



A University of Sussex PhD thesis

Available online via Sussex Research Online:

<http://sro.sussex.ac.uk/>

This thesis is protected by copyright which belongs to the author.

This thesis cannot be reproduced or quoted extensively from without first obtaining permission in writing from the Author

The content must not be changed in any way or sold commercially in any format or medium without the formal permission of the Author

When referring to this work, full bibliographic details including the author, title, awarding institution and date of the thesis must be given

Please visit Sussex Research Online for more information and further details

Modelling and analysing neuronal and
epidemiological dynamics on structured static and
dynamic networks

Rosanna Claire Barnard

Submitted for the degree of Doctor of Philosophy

Department of Mathematics

University of Sussex

September 2018

Declaration

I hereby declare that this thesis has not been, and will not be, submitted in whole or in part to another University for the award of any other degree. I also declare that this thesis was composed by myself, under the supervision of Professor István Z. Kiss and Dr Luc Berthouze, and the work contained therein is my own, except where indicated by citations and in the list of publications and author contributions.

Signature:

(Rosanna Claire Barnard)

UNIVERSITY OF SUSSEX

ROSANNA CLAIRE BARNARD

THESIS SUBMITTED FOR THE DEGREE OF DOCTOR OF PHILOSOPHY
IN MATHEMATICSMODELLING AND ANALYSING NEURONAL AND EPIDEMIOLOGICAL
DYNAMICS ON STRUCTURED STATIC AND DYNAMIC NETWORKSSUMMARY

Many of the technological, social and biological systems we observe and partake in in our everyday lives can be described as networks of interacting elements. Network-based research can then be performed to improve our understanding about the structural features of such complex networks, the behaviour of processes occurring within such complex networks, and the interaction between the two. During my PhD I have considered neuronal and epidemiological dynamics occurring on complex networks, with the main aim of improving model realism by incorporating spatial or local structure whilst maintaining model tractability. In total I have considered three network-based research projects which are included in this thesis in chronological order.

This thesis begins with an introduction to the study of complex networks and processes occurring on complex networks. Comparisons are drawn between the approaches of neuroscience and epidemiology-based network studies, including consideration of the difficulties regarding modelling local spatial structure. Chapter 2 considers an existing model describing the activity-dependent growth and development of a network of excitatory and inhibitory neurons embedded in space. A systematic investigation of the effects of various spatial arrangements of neurons on the resultant electrical dynamics finds that increased spatial proximity between inhibitory neurons leads to oscillatory dynamics. Chapter 3 utilises the edge-based compartmental modelling approach. Existing research is extended to derive and validate equations describing the evolution of a susceptible-infected-recovered (SIR) epidemic process occurring on a dual-layer multiplex network incorporating heterogeneity in the structure, type and duration of connections between individuals. Chapter 4 considers pairwise models describing the SIR epidemic process and derives and validates analytic expressions for the epidemic threshold, an improvement on existing results. This thesis concludes with a discussion of the research contained in Chapters 2-4, including suggestions for improvements and future research ideas.

Acknowledgements

Firstly, I would like to thank my academic supervisors Professor István Z. Kiss and Dr Luc Berthouze for their guidance throughout my time as a PhD researcher. I would like to thank the UK's Engineering and Physical Sciences Research Council for funding my PhD studentship and I would also like to give thanks to the researchers I collaborated with on the work contained within this thesis.

There are numerous people I have had the pleasure of knowing or meeting during my time as a PhD researcher in the School of Mathematical and Physical Sciences and I wish to acknowledge their contributions in supporting me to do this work. From friends, colleagues and university facilities staff to professional services staff and students, this piece of work would not be the same without all of these people and I am immensely grateful to all those unnamed individuals for their presence and inspiration. Finally, and most importantly, I would like to thank my family, who have continuously supported and encouraged me throughout this process.

List of publications and author contributions

- **Clustered arrangement of inhibitory neurons can lead to oscillatory dynamics in a model of activity-dependent structural plasticity**

Rosanna C. Barnard, István Z. Kiss, Simon F. Farmer & Luc Berthouze.

Published as a chapter in *The Rewiring Brain: A Computational Approach to Structural Plasticity in the Adult Brain* (pp. 123-154), edited by Arjen van Ooyen and Markus Butz-Ostendorf, published by San Diego: Academic Press, 2017.

- Rosanna C. Barnard conceived the overall goals and design of the study, developed and implemented the original and additional Matlab code for our analyses, derived novel measures for inhibitory clustering, performed simulations and analyses and produced the majority of the Figures, wrote the first draft, reviewed the first draft and agreed upon final additions and changes, and contributed towards writing the final draft.
- István Z. Kiss conceived the overall goals and design of the study, supervised the work of Rosanna C. Barnard, derived novel measures for inhibitory clustering, produced images depicting network motifs, reviewed the first draft and agreed upon final additions and changes, and contributed towards writing the final draft.
- Simon F. Farmer reviewed the first draft and agreed upon final additions and changes, provided additional content discussing future modelling and experimental studies, and contributed towards writing the final draft.
- Luc Berthouze conceived the overall goals and design of the study, provided Matlab code to implement the basic model, supervised the work of Rosanna C. Barnard, derived novel measures for inhibitory clustering, wrote a script to generate exhaustive lists of spatial arrangements, performed some analyses

and produced an additional Figure, reviewed the first draft and agreed upon final additions and changes, contributed towards writing the final draft and submitted the research for publication.

- **Edge-based compartmental modelling of an SIR epidemic on a dual-layer static-dynamic multiplex network with tunable clustering**

Rosanna C. Barnard, István Z. Kiss, Luc Berthouze & Joel C. Miller.

Published in *Bulletin of Mathematical Biology*, August 2018.

Available at <https://rdcu.be/41ZB>

- Rosanna C. Barnard conceived the overall goals and design of the study, contributed towards the derivation of model equations and the epidemic threshold, wrote and implemented Matlab code to solve model equations and to validate their predictions by generating equivalent networks alongside simulated epidemic processes, performed analyses and produced all Figures, wrote the first draft and subsequent revisions of the paper and submitted the work for publication.
- István Z. Kiss conceived the overall goals and design of the study, contributed towards the derivation of model equations and the epidemic threshold, supervised the work of Rosanna C. Barnard and contributed towards reviewing the first draft and producing the final draft.
- Luc Berthouze conceived the overall goals and design of the study, supervised the work of Rosanna C. Barnard and contributed towards reviewing the first draft and producing the final draft.
- Joel C. Miller conceived the overall goals and design of the study, contributed towards the derivation of model equations and the epidemic threshold and contributed towards reviewing the first draft and producing the final draft.

- **Epidemic threshold in pairwise models for clustered networks: closures and fast correlations**

Rosanna C. Barnard, Luc Berthouze, Péter L. Simon & István Z. Kiss.

Submitted to journal for peer-review, June 2018.

Available at <https://arxiv.org/abs/1806.06135>

- Rosanna C. Barnard conceived the overall goals and design of the study, contributed towards mathematical calculations and analyses, contributed towards

writing the first draft, reviewed the first draft and contributed towards writing the final draft.

- Luc Berthouze conceived the overall goals and design of the study, supervised the work of Rosanna C. Barnard and reviewed the first draft.
- Péter L. Simon conceived the overall goals and design of the study, contributed towards mathematical calculations and analyses and reviewed the first draft.
- István Z. Kiss conceived the overall goals and design of the study, supervised the work of Rosanna C. Barnard, contributed towards mathematical calculations and analyses, performed analyses and produced Figures in Matlab, contributed towards writing the first draft, reviewed the first draft, contributed towards writing the final draft and submitted the work for publication.

Contents

List of Tables	x
List of Figures	xxi
1 Introduction	1
1.1 Background and motivation	1
1.2 Thesis contribution	4
1.3 Thesis structure	8
2 Clustered arrangement of inhibitory neurons can lead to oscillatory dynamics in a model of activity-dependent structural plasticity	11
2.1 Introduction	11
2.2 Model	14
2.3 Model implementation	16
2.4 Methods	16
2.4.1 Parameter choice	16
2.4.2 Spatial arrangement of excitatory and inhibitory neurons	17
2.4.3 Measuring spatial clustering of inhibition in $1D$ and $2D$ neuron arrangements	18
2.5 Results	19
2.5.1 $1D$ results	19
2.5.2 $2D$ results	34
2.6 Discussion	36
2.6.1 Comparison to previous modelling results	39
2.6.2 $1D$ network behaviours	41
2.6.3 $2D$ network behaviours	42
2.6.4 Future modelling studies	43
2.6.5 Future experimental studies	44

2.6.6	Concluding remarks	45
2.7	Acknowledgements	46
3	Edge-based compartmental modelling of an SIR epidemic on a dual-layer static-dynamic multiplex network with tunable clustering	47
3.1	Introduction	47
3.2	Methods	50
3.2.1	Edge-based compartmental model derivation	53
3.2.2	Deriving the basic reproduction number R_0	61
3.2.3	Model implementation	65
3.2.4	Simulation implementation	66
3.3	Results	67
3.3.1	Model convergence to existing uniplex model equations	68
3.3.2	Model validation by comparison with simulation	71
3.3.3	A brief exploration of parameter spaces	71
3.3.4	Contribution of network layers via $(p_s + p_t + p_d) \equiv 1$	75
3.3.5	Validation of basic reproduction number R_0	77
3.4	Discussion	80
3.5	Acknowledgements	85
4	Epidemic threshold in pairwise models for clustered networks: closures and fast correlations	86
4.1	Introduction	86
4.2	Model formulation	89
4.2.1	The network	89
4.2.2	SIR dynamics	89
4.2.3	The unclosed pairwise model	90
4.3	Closures	90
4.3.1	Closure for unclustered networks	90
4.3.2	Closure for clustered networks	92
4.4	Results for the pairwise model with the simple closure	97
4.4.1	Background	97
4.4.2	Epidemic threshold	98
4.4.3	Fast variables with the simple closure	99
4.4.4	Asymptotic expansion of the epidemic threshold	101

4.4.5	Numerical examples	103
4.5	Results for the pairwise model with the compact improved closure	103
4.5.1	Fast variables with the compact improved closure	105
4.5.2	Asymptotic expansion of the epidemic threshold	105
4.5.3	Numerical examples	107
4.6	Discussion	107
4.7	Acknowledgements	112
Appendices		113
4.A	Derivation of evolution equations for the fast variables with simple closure .	113
4.B	Derivation of evolution equations for the fast variables with the compact improved closure	115
4.C	Standard linear stability analysis for the case of the simple closure	117
4.D	Standard linear stability analysis for the case of the compact improved closure	118
5	Discussion	120
5.1	Summarising the work presented in Chapter 2	121
5.2	Summarising the work presented in Chapter 3	123
5.3	Summarising the work presented in Chapter 4	125
5.4	Implications of the work & future research	127
5.5	Final remarks	129
Bibliography		130




List of Tables

2.1	Default values for all model parameters used in simulations	15
2.2	Global system behaviour and clustering measure for mixed $1D$ simulations with various spatial arrangements. Default values were used on initially disconnected networks. S denotes stabilisation of the network and activity, SO denotes stable oscillatory behaviour, UO denotes unstable oscillatory behaviour, and TO denotes transient oscillatory behaviour. All $1D$ clustering measures are given as exact values or to four significant figures.	22
2.3	Network motif counts at various points of the simulations in Figures 2.5 - 2.7. Network motifs are displayed here in two dimensions for ease of visualisation, but all structures considered are $1D$ lattice structures with periodic boundaries.	33
2.4	Global system behaviour and clustering measure for mixed $2D$ simulations with various spatial arrangements. Default values were used on initially disconnected networks.	35
3.1	Definitions for model variables and parameters. Many definitions refer to the test node u , which is selected at random from the population and modified so that it cannot transmit infection, but can itself become infected. . .	51

List of Figures

1.1	Partial map of the Internet based on the January 15, 2005 data found on The Opte Project [67]. Each line is drawn between two nodes, representing two IP addresses. The length of the lines are indicative of the delay between those two nodes. This graph represents less than 30% of the Class C networks reachable by the data collection program in early 2005. Lines are colour coded according to their corresponding RFC 1918 allocation as follows: ■: net, ca, us, ■: com, org, ■: mil, gov, edu, ■: jp, cn, tw, au, de, ■: uk, it, pl, fr, ■: br, kr, nl, ■: unknown. Image reproduced without changes from Wikipedia [126], licensed under a CC BY 2.5	2
1.2	The feedback loop that occurs between the dynamics <i>on</i> and <i>of</i> an adaptive or coevolutionary network. Inspired by Figure 1 of [36].	3
1.3	Flow diagram representing the compartments and transitions possible within the basic SIR compartmental model	4
1.4	Flow diagram representing the compartments and transitions possible within the basic SIRS (upper) and QARQ (lower) compartmental models	7
2.1	Global system behaviour of mixed 1D lattice networks with various spatial arrangements of neurons. In all cases $L = 13$, $N = 9$, $M = 4$ and default parameters listed in Table 2.1 are used. The networks are initially wholly disconnected and neurons are at rest. Figures on the <i>left-hand side</i> depict the dynamics of the individual neuritic radii values; figures on the <i>right-hand side</i> depict the dynamics of the individual electrical activity values. Neuron arrangements are as follows: ●●●●●●●●●●●●●●●● (A,B), ●●●●●●●●●●●●●●●● (C,D), ●●●●●●●●●●●●●●●● (E,F).	21

- 2.2 Global system behaviour of mixed 1D lattice networks with various levels of inhibitory clustering.** In all cases, $L = 10$, $N = 7$, $M = 3$ and default parameters listed in Table 2.1 are used. The networks are initially wholly disconnected and neurons are at rest. Figures on the *left-hand side* depict the dynamics of the individual neuritic radii values; figures on the *right-hand side* depict the dynamics of the individual electrical activity values. Neuron arrangements are as follows: ●●●●●●● (A,B), ●●●●●●● (C,D), ●●●●●●● (E,F), ●●●●●●● (G,H). 25
- 2.3 1D system behaviours for growth simulation setups with various proportions of inhibitory neurons and levels of inhibitory clustering.** *Green boxes* denote stabilisation of network structure and electrical activity. *Purple boxes* denote large unstable oscillations in network structure and unstable burst-like oscillations in electrical activity. *Blue boxes* denote stable oscillatory behaviour of neuritic radii and electrical activities. *Pink boxes* denote unbounded growth examples, where the system was unable to reach the desired level of electrical activity for all neurons, with all neuritic fields growing indefinitely. *White areas* did not have any suitable configurations to run. In panel **A**, the networks were initially disconnected. In panel **B**, the networks started as regular ring networks. 26
- 2.4 1D system behaviours as a function of the percentage of inhibitory cells (*horizontal axis*) and number of tile repeats (*vertical axis*).** All tile arrangements are contiguous. Tiles are repeated in an adjacent manner to maintain a 1D system. *Green circles* denote networks experiencing complete stabilisation. *Blue circles* denote periodic (stable) oscillatory behaviour. *Purple circles* denote unstable oscillatory behaviour. *Pink circles* denote simulations where all neuritic fields grow unbounded because the desired level of electrical activity cannot be reached. In panel **A**, the networks were initially disconnected. In panel **B**, the networks started with sparse connectivity, with neuritic radii values randomly generated in the interval (0,0.6) (identical seed of value 10 for all networks). All other parameters were as listed in Table 2.1. 27

2.5	Global system behaviour and analysis of the associated network structure at equilibrium. This is the same simulation as shown in Figure 2.1 E and F , with the spatial arrangement  . Panel A depicts the dynamics of the neuritic radii, B depicts the dynamics of the electrical activity values, C is a visualisation of the network's structure at the end of the simulation, where circles with shades of blue denote the field of an excitatory neuron and circles with shades of red denote the field of an inhibitory neuron. Panel D shows the degree distribution of all neurons at equilibrium.	30
2.6	Network structure and degree distribution of the simulation shown in Figure 2.1 A and B, at three time points during the periodic oscillations. See coloured markers in panel C , where a <i>red circle</i> denotes a low point in an oscillation, a <i>green circle</i> denotes a midpoint in an oscillation, and a <i>pink circle</i> denotes a high point in an oscillation. The spatial arrangement of neurons is  with the network being initially disconnected. Panels B and D show the network structure and associated degree distribution at a low point in an oscillation, panels E and G show the network structure and associated degree distribution at a midpoint in an oscillation, and panels F and H show the network structure and associated degree distribution at a high point of an oscillation shown in panel C	31
2.7	Network structure and degree distribution of the simulation shown in Figure 2.1 C and D, at three time points during the unstable oscillations. See coloured markers in panel C , where a <i>green triangle</i> denotes a time during burst-like behaviour of electrical activity, a <i>red triangle</i> denotes a time immediately after the burst-like behaviour, and a <i>pink triangle</i> denotes a time where the network is experiencing a peak of connectivity (corresponding triangles are also shown in panel A). The spatial arrangement of neurons is  with the network initially disconnected. Panels B and D show the network structure and associated degree distribution during the burst-like behaviour. Panels E and G depict the network structure and associated degree distribution after the burst-like behaviour and panels F and H show the network structure and associated degree distribution at the peak of connectivity.	32

- 2.8 Global system behaviour of mixed 2D lattice networks with various levels of inhibitory clustering.** In all cases $L = 36$, $N = 30$, $M = 6$ and default parameters listed in Table 2.1 are used. The networks are initially wholly disconnected and neurons are at rest. Figures on the *left-hand side* depict the dynamics of the individual neuritic radii values; figures on the *right-hand side* depict the dynamics of the individual electrical activity values. Panels **A** and **B** depict the dynamics of arrangement 47 in Table 2.4, panels **C** and **D** depict the dynamics of arrangement 51 in Table 2.4, panels **E** and **F** depict the dynamics of arrangement 49 in Table 2.4 and panels **G** and **H** depict the dynamics of arrangement 50 in Table 2.4. 37
- 2.9 The proportion of 2D neural network growth simulations depicting oscillatory behaviour of electrical activity and network connectivity for a range of WH/M values, where the terms W, H and M are defined in Equation (2.9).** Growth simulations consisted of networks of $L = 36$ neurons with $M = 6, 7, 8, 9, 10, 11$ inhibitory neurons, and default parameters listed in Table 2.1 were used. Networks were initially wholly disconnected and neurons were at rest. For each M , 2 million neuron arrangements were generated at random, from which the unique set of WH values was extracted. For each (M, WH) pair, 200 neuron arrangements were selected at random. Growth simulations of all 200 arrangements were implemented and the result tested for behaviour through thresholding of the norm of the variance of the last 10 data points, where the norm was taken over all L neurons. Thresholds were empirically determined and confirmed visually. The procedure of picking 200 arrangements for each (M, WH) pair was repeated 50 times to obtain the mean and standard deviation, displayed in the plot using error bars. Empty circles denote (M, WH) pairs for which less than 200 arrangements were available for testing. 38
- 3.1 Flow diagram for the flux of a static line partner through different states.** The flux between the probabilities that the test node u is connected by a line (2-clique) on the static network layer to a node v that has not transmitted infection to u and is susceptible (ϕ_S), infectious (ϕ_I) or recovered (ϕ_R), and the probability that v has transmitted infection to u , equal to $(1 - \theta_2)$ 54

- 3.2 Flow diagram for the flux of two triangle neighbours through different states.** The flux between the probabilities that the test node u is connected in a triangle to two nodes in all possible disease status configurations, where neither triangle neighbour has transmitted infection to u , as well as the probability $(1 - \theta_3)$ that a node $v \neq u$ in the triangle has transmitted infection to the test node u 55
- 3.3 Flow diagram for the flux of a dynamic edge partner through different states.** The flux between the probabilities $\theta_4 = \psi_S + \psi_I + \psi_R$ that a random stub currently connected to u on the dynamic network layer has never been involved in transmitting infection to u . Note that the compartment denoted $\eta\theta_4$ is not a compartment in the typical sense. When edges break (at rate η) in the model, moving into ‘compartment’ $\eta\theta_4$, new edges are formed *immediately* without delay, moving straight back into compartments ψ_S , ψ_I or ψ_R . π_S , π_I and π_R denote the probabilities that a randomly chosen dynamic stub belongs to a susceptible, infected, or recovered node, respectively 58
- 3.4 Flow diagram for the flux of a dynamic line stub through different states.** The flux between π_S , π_I and π_R , the probabilities that a randomly chosen dynamic stub belongs to a susceptible, infected or recovered node, respectively 58

3.5 Multiplex model convergence — no dynamic layer, with simulation.

The time evolution of infection prevalence for the original EBCM of an SIR epidemic on a static uniplex network (solid black line), for the proposed EBCM of an SIR epidemic on a dual-layer multiplex with the dynamic network layer being close to zero (thick dashed red line), and for 10 Gillespie simulations of the SIR epidemic on a single network of size $N = 5000$ (solid blue lines). In all panels $\gamma = 1$, $\rho = 0.05$, and $p = 0.5$ and $r = 10$ generate a negative binomial distribution for pairs of edge stubs. For the original static derivation (solid black line) $p_s = 0.5 = p_t$, describing the proportion of edge-pairs that are split into two single lines or remain as a triangle corner, respectively. For the multiplex derivation (thick dashed red line) $\beta_s = \beta_d$, $\eta = 0.01$, and $p_s = 0.4999999$, $p_t = 0.5$ and hence $p_d = 10^{-7}$ describe the proportion of edge-pairs that become two static lines, a static triangle corner, or two dynamic edges respectively. (a) $\beta's = 1$, $C = 0.02677$, (b) $\beta's = 0.5$, $C = 0.02670$, (c) $\beta's = 0.25$, $C = 0.02658$, (d) $\beta's = 0.125$, $C = 0.02685$, where C denotes the global clustering coefficient of each static network layer generated for simulation . 69

3.6 Multiplex model convergence — no static layer, with simulation.

The time evolution of infection prevalence for the original EBCM of an SIR epidemic on a dynamic uniplex network with conserved degrees and edge re-wiring (solid black line), for the proposed multiplex EBCM of an SIR epidemic with the static network layer being close to zero (thick dashed red line), and for 10 Gillespie simulations of the process on a single network of size $N = 5000$ (solid blue lines). In all panels $\gamma = 1$, $\rho = 0.05$, and $p = 0.5$ and $r = 10$ generate a negative binomial distribution for pairs of edge stubs. For the original conserved-degree derivation (solid black line) $p_d = 1$, indicating that all edge-pairs become two disjoint dynamic edges. For the multiplex derivation (thick dashed red line), $\eta = 0.01$ and $p_s = p_t = 10^{-7}$ and $p_d = 0.9999998$ describe the proportion of edge-pairs that become two static lines, single triangle corners, or two dynamic edges respectively. (a) $\beta's = 1$, $C = 0.004944$, (b) $\beta's = 0.5$, $C = 0.005285$, (c) $\beta's = 0.25$, $C = 0.005344$, (d) $\beta's = 0.125$, $C = 0.005127$, where C denotes the global clustering coefficient of each dynamic network layer generated for simulation, at time zero 70

3.7 Multiplex model prediction vs. simulation — varying clustering

and average degree. Plotting the dynamics of the proportion of infected individuals over time. Each panel contains 25 Gillespie simulations on a single multiplex network comprised of $N = 1000$ individuals (blue lines) and the associated EBCM prediction (black line). All networks are generated using a negative binomial distribution for pairs of edge stubs with parameters $p = 0.5$ and various values for r . Networks in column 1 (counting from left to right) have average degree 10 (achieved via $r = 5$), networks in column 2 have average degree 20 (achieved via $r = 10$) and networks in column 3 have average degree 30 (achieved via $r = 15$). Networks in row 1 (counting from top to bottom) have minimised clustering via values $p_s = 0.99999998$ and $p_t = 10^{-8}$. Networks in row 2 have the values $p_s = 0.49999999 = p_t$. Networks in row 3 have maximised clustering via the values $p_s = 10^{-8}$ and $p_t = 0.99999998$. Counting panels from left to right and top to bottom, starting with the upper-left panel, static networks have the following clustering coefficients: $C = 0.0161$, $C = 0.0267$, $C = 0.0370$, $C = 0.0535$, $C = 0.0473$, $C = 0.0493$, $C = 0.0898$, $C = 0.0662$, $C = 0.0629$. In all panels, $tmax = 10$, $\rho = 0.05$, $\beta_s = \beta_d = 0.25$, $\gamma = 1$, $\eta = 0.01$ 72

3.8 Multiplex model prediction vs. simulation — varying infection

parameters β_s and β_d . Plotting the dynamics of the proportion of infected individuals over time. Each panel contains 100 Gillespie simulations (10 simulations on 10 multiplex networks comprised of $N = 5000$ individuals) (blue lines) and the associated EBCM prediction (black line). All multiplex networks follow a negative binomial distribution for pairs of edge stubs with parameters $p = 0.5$ and $r = 10$, which were split into three edge types via $p_s = 0.3 = p_t$ and thus $p_d = 0.4$. In all panels $tmax = 10$, $\rho = 0.05$, $\gamma = 1$, $\eta = 0.01$. Across the panels, different values for β_s and β_d have been used in the range $[0.125, 0.25, 0.5]$, indicated by individual column and row headings 73

3.9 Multiplex model predictions. Plotting the dynamics of the proportion of infected individuals over time, for a number of different parameter sets. In all panels, a baseline parameter set ($p = 0.5$, $r = 10$, $p_s = 0.3 = p_t$, $p_d = 0.4$, $\beta_s = 0.05$, $\beta_d = 0.2$, $\gamma = 1$, $\eta = 0.01 = \rho$, $tmax = 10 \Rightarrow R_0 = 1.076$) is used to plot dynamics predicted by multiplex model equations (3.1)-(3.23) (thick black line). In each panel, a single parameter is varied and the resultant predictions are plotted in various colours, indicated by individual panel legends. In the bottom row of panels, parameters p_s , p_t and p_d are being varied. Since the model has the constraint $(p_s + p_t + p_d) \equiv 1$, we alter the triplet values in each panel in the following way. Assume we are varying the parameter p_s . If the new p_s is larger than the baseline p_s , we subtract $\frac{1}{2}$ the difference from the remaining baseline parameters p_t and p_d . Conversely, if the new p_s is smaller than the baseline p_s , $\frac{1}{2}$ the difference is added to each of the values p_t and p_d 74

3.10 Multiplex model layer contributions. Heat map plots depicting the final epidemic size (equal to the fraction of the population who are either infectious or recovered at the end of the epidemic process) predicted by equations (3.1)-(3.23) for a multiplex network of various proportions p_s , p_t (y -axes) and p_d (x -axes), with the model constraint $(p_s + p_t + p_d) \equiv 1$. For all setups $\gamma = 1$, $\rho = 0.01$, $tmax = 25$ and pairs of edge stubs followed a discrete homogeneous distribution where all individuals had 2 edge pairs (and hence total degree 4). The values of remaining model parameters η , β_s and β_d are indicated above each panel, with $\eta \in [0.01, 1, 100]$, $\beta_s \in [0.55, 0.6, 0.65]$ and $\beta_d \in [\beta_s/2, \beta_s, 2\beta_s]$. All 27 possible combinations of the parameters η , β_s and β_d are considered. Prior to implementation, a number of setups across the (p_s, p_t, p_d) parameter spaces in each panel were tested by hand to ensure that the epidemic process had concluded by time $tmax = 25$. . . 76

3.11 Validation of the basic reproduction number R_0 . Plotting values of the basic reproduction number R_0 (x -axis), found via the leading eigenvalue of the matrix (3.24), against the associated final epidemic sizes (y -axis) predicted by multiplex equations (3.1)-(3.23) (red line) and recorded by single statistically-correct Gillespie simulations (blue circles). Static and dynamic line stubs follow binomial distributions with parameters $n = 20$ and $p = 0.5$. The distribution of triangle corners follows a binomial distribution with parameters $n = 1$ and $p = 0.001$ to minimise clustering. Fixed parameters were $\gamma = 1$, $\rho = 0.001$, $\eta = 0.01$, $tmax = 10$, $N = 1000$. In each setup $\beta_s = \beta_d$. 100 transmission rates were tested, from $\beta_s = \beta_d = 0.01$ up to $\beta_s = \beta_d = 0.3$, in equal-sized increments. In Gillespie simulations where $R_0 > 1$, if the number of infected individuals did not reach 10 times the initial number of infectives, all data was discarded and the Gillespie script restarted from initial conditions at time zero 78

3.12 Effects of rewiring, average degrees and clustering. Plotting the value of R_0 and the associated final epidemic size found using EBCM equations (3.1)-(3.23), for a number of different setups. Upper-left panels: Testing 100 evenly-spaced values for η in the range $[0.01, 50]$. Remaining model parameters were $p_s = 0.3 = p_t$, $\beta_s = 0.1 = \beta_d$, $\gamma = 1$, $\rho = 0.01$ and $tmax = 25$. Pairs of edge stubs followed a negative binomial distribution with parameters $p = 0.5$ and $r = 5$. Upper-right panels: Testing 15 evenly-spaced values for $\langle k \rangle \in [2, 30]$, generated using a negative binomial distribution for pairs of edge stubs with fixed $p = 0.5$ and $r \in [1, 15]$. Remaining model parameters were $p_s = 0.3 = p_t$, $\beta_s = 0.0625 = \beta_d$, $\gamma = 1$, $\eta = 0.1$, $\rho = 0.01$, $tmax = 25$. Lower-left panels: Testing 100 evenly-spaced values for p_t in the range $[0.01, 0.99]$. The proportion $(1 - p_t)$ was split equally between parameters p_s and p_d . Remaining model parameters were $\beta_s = 0.5 = \beta_d$, $\gamma = 1$, $\rho = 0.01$, $\eta = 0.1$ and $tmax = 25$. Pairs of edge stubs followed a discrete homogeneous distribution where all individuals had 2 edge pairs. Lower-right panels: Testing 15 evenly-spaced values for $\langle k \rangle \in [2, 30]$, generated using a discrete homogeneous distribution for pairs of edge stubs where all individuals have identical degree. Remaining model parameters were $p_s = 0.3 = p_t$, $\beta_s = 0.0625 = \beta_d$, $\gamma = 1$, $\rho = 0.01$, $\eta = 0.1$, $tmax = 25$ 79

- 4.1 Flow diagrams showing the flux between compartments of singles (left) and compartments of pairs (right) in the SIR pairwise model. In the compartments of pairs, straight arrows denote infections coming from within the pair (with a rate depending on a pair) or from outside the pair (with a rate depending on a triple), and curved arrows denote a recovery. The colour indicates the status of the “first” node in the pair. Symmetry allows us to conclude that some of the variables (see lighter shaded variables on the right hand side of the pairs diagram) must equal their symmetric version (e.g. $[RS] = [SR]$), so we do not need to directly calculate both quantities. 91
- 4.2 General setup for a central susceptible node with a given infected neighbour for (a) unclustered and (b) clustered regular networks with degree n . Dashed arrows indicate that the infected node may be connected to the other neighbours of the central susceptible node. Random variables X_1, X_2, \dots, X_{n-1} take values from the set $\{S, I, R\}$ 91
- 4.3 Illustration of the dynamics of prevalence, $[I]/N$, over time ((a)-(b)), compared to that of $\alpha = \frac{[SI]}{[I]}$ ((c)-(d)) and $\delta = \frac{[II]}{[I]}$ ((e)-(f)) for the pairwise model with the simple (left column) and the improved (right column) closures. Parameter values are $N = 10000$, $n = 5$, $\phi = 0.5$ and $\tau = \gamma = 1$ 100
- 4.4 Assessing the validity of the epidemic threshold based on the asymptotic approximation (4.45) (dashed line and markers - \circ) by comparing it to the epidemic threshold based on the numerical solution of the cubic equation (4.39) (continuous lines). In the right hand column we compare both threshold curves in the $(\tau, n, 0)$ plane. In the left hand column both curves are compared to the final epidemic size based on numerical integration of the pairwise model equations with the simple closure. Parameter values are $N = 10000$, $\gamma = 1$ and from top to bottom the clustering coefficients are $\phi = 0, 0.15, 0.3, 0.45, 0.6$ 104

4.5	Assessing the validity of the epidemic threshold based on the asymptotic expansion (4.62) (dashed line and markers - \circ) by comparing it to the epidemic threshold based on the numerical solution of the cubic equation (4.52) (continuous lines). In the right hand column we compare both threshold curves in the $(\tau, n, 0)$ plane. In the left hand column both curves are compared to the final epidemic size based on numerical integration of the pairwise model equations with the compact improved closure. Parameter values are $N = 10000$, $\gamma = 1$ and from top to bottom the clustering coefficients are $\phi = 0, 0.15, 0.3, 0.45, 0.6$.	108
-----	--	-----

Chapter 1

Introduction

1.1 Background and motivation

Networks, comprised of nodes connected by links or edges, can be utilised to describe many of the complex systems we observe in the real-world, such as the structure of interconnected neurons and synapses in the brain, as well as other technological, biological and social networks [82]. Networks can be static, meaning that the population of nodes and their connection structure remain fixed over time. Conversely, dynamic networks allow for changes in the composition of the population and its structure over time. Individuals, described by nodes, can join or leave the population, whilst connections between existing population members can be continuously created and removed. A visualisation of part of the structure of the internet, taken as a snapshot on the 15th of January 2005, is provided in Figure 1.1 and demonstrates the level of complexity even partial and static real-world networks can exhibit.

Studying the structural characteristics of naturally occurring and man-made real-world networks can provide insight into which structural features are most common and how such features influence the network's characteristics as a whole. Recent examples of research considering network architecture include the consideration of scientific collaboration networks [83], ecological food webs [79], mobile phone communication networks [86], air transportation networks [39], political blog networks [1], financial transaction networks [7], metabolic networks [49] and semantic networks [108]. In dynamic networks, such research can consider fluctuations in the prevalence of specific topological/structural features over time [59].

As well as studying the topological features of empirical networks, research can consider dynamical processes occurring within and between each node of a network over time [122].

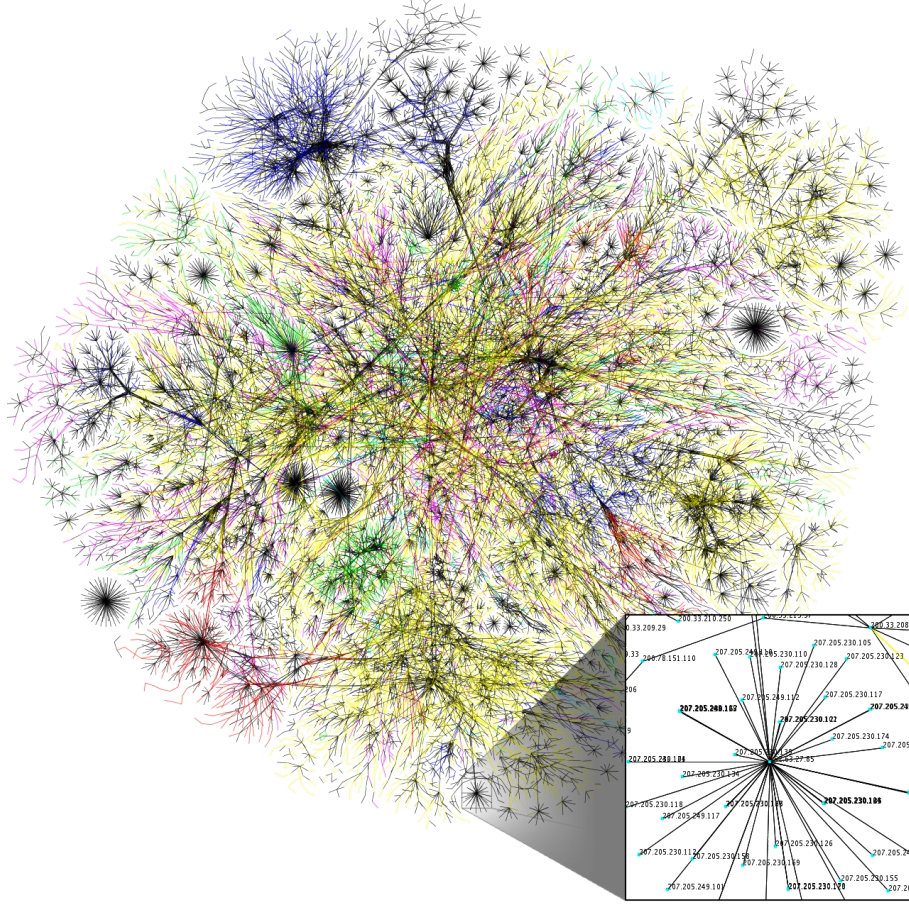


Figure 1.1: Partial map of the Internet based on the January 15, 2005 data found on [The Opte Project](#) [67]. Each line is drawn between two nodes, representing two IP addresses. The length of the lines are indicative of the delay between those two nodes. This graph represents less than 30% of the [Class C](#) networks reachable by the data collection program in early 2005. Lines are colour coded according to their corresponding [RFC 1918](#) allocation as follows: ■: net, ca, us, ■: com, org, ■: mil, gov, edu, ■: jp, cn, tw, au, de, ■: uk, it, pl, fr, ■: br, kr, nl, ■: unknown. Image reproduced without changes from [Wikipedia](#) [126], licensed under a [CC BY 2.5](#).

For example, the process of diseases spreading amongst populations of individuals [88], the process of man-made viruses spreading across networked computers [5], or the processes of rumour spreading and opinion formation within social networks [81, 34]. In many cases, a major aim is to understand how specific structural features of the network affect the dynamical process being modelled. For example, in the context of an epidemic spreading within a human population, increased levels of clustering, describing the propensity for two friends¹ of an individual to also be friends themselves, has been shown to inhibit epidemic spreading [125]. However, the relationship between clustering and the outcome of the epidemic is complex. The same authors find that simultaneously increasing clustering and

¹The terminology ‘friend’ is used to describe a population member that is connected to, or makes connections with, the individual in question

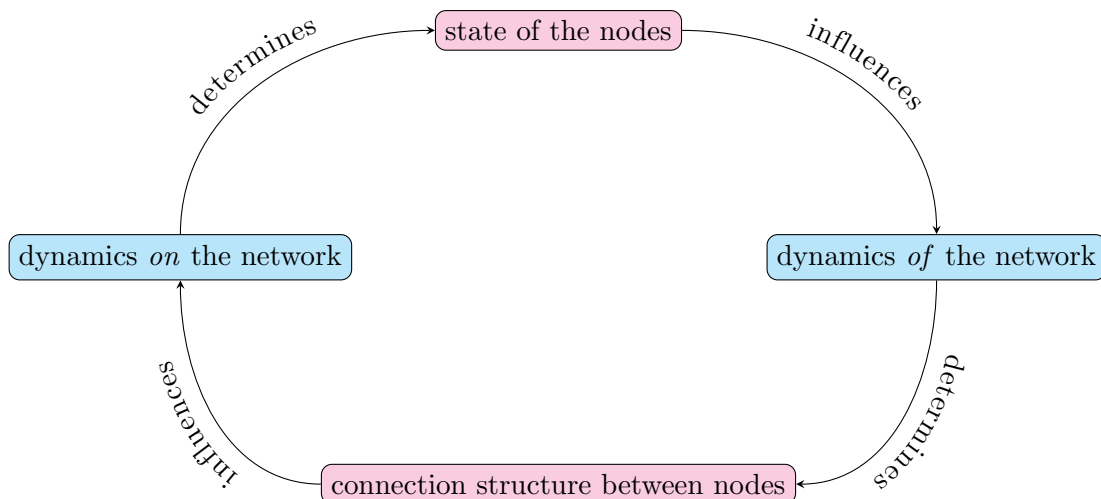


Figure 1.2: The feedback loop that occurs between the dynamics *on* and *of* an adaptive or coevolutionary network. Inspired by Figure 1 of [36].

the variance of the degree distribution, describing the probability distribution governing the number of edges an individual partakes in, leads to an increase in the final size of the epidemic [125].

When considering dynamic processes on dynamic networks, not only can research investigate how the topological features of the network influence the dynamical process on the network, it can also consider how the dynamical process influences the topological features of the network. These interacting processes form a feedback loop between the state of the nodes and the network’s topology [36], and such networks are referred to as coevolutionary or adaptive networks. A visualisation of this feedback loop is given in Figure 1.2.

The feedback loop between the dynamics *on* and *of* the network can be easily understood in the context of an epidemic spreading through a population of individuals. As mentioned previously, the connection structure between individuals influences the spread of the epidemic, or the dynamics occurring *on* the network. The spread of the epidemic determines the state of the various nodes in the network (e.g. some nodes become infected). If population members become aware of the epidemic prior to becoming infected, for example if their neighbour becomes infected, they may reduce their susceptibility by altering the connections they make with other individuals. This process causes changes to the connection structure of the network which are otherwise referred to as the dynamics *of* the network. Thus, a reaction to the epidemic leads to a change in behaviour which influences the network’s topology and eventually the course of the epidemic itself.

Awareness of an epidemic can itself be considered as a dynamical process, and the

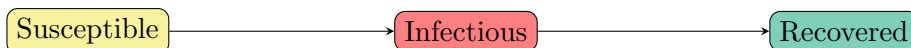


Figure 1.3: Flow diagram representing the compartments and transitions possible within the basic SIR compartmental model

interaction between this process and the epidemic process has been considered on complex networks in [29] and [35]. Reviews of research considering the influence of human behaviour on infectious disease spread and of research on adaptive networks can be found in [30] and [36], respectively.

1.2 Thesis contribution

This thesis is composed of three pieces of research I undertook during my PhD studentship. All three pieces of research consider dynamic processes occurring on complex networks and use the same mathematical formalism, whereby complex networks are described by a set of nodes and their respective connections. The first piece of research considers a network-based model from neuroscience which describes the growth and development of a network of excitatory and inhibitory neurons embedded in space. The second and third pieces of research consider network-based models from epidemiology, with both models tracking the dynamics in time of a *susceptible-infected-recovered* (SIR) epidemic process. The compartments and transitions possible within the SIR compartmental model are visualised in Figure 1.3.

Early precursors of network-based models made strong unifying assumptions that disregarded local spatial structure, be that spatial embedding or clustering. For example, the original compartmental SIR model, derived following work by Kermack & McKendrick in 1927 [55], assumes homogeneous mixing, whereby all pairs of individuals within the population are assumed to come into contact at the same rate. The ordinary differential equations governing the dynamics in time of each disease compartment are

$$\frac{dS}{dt} = -\beta \frac{SI}{N} \quad (1.1)$$

$$\frac{dI}{dt} = \beta \frac{SI}{N} - \gamma I \quad (1.2)$$

$$\frac{dR}{dt} = \gamma I, \quad (1.3)$$

where $S + I + R \equiv N$, N being the population size, infectious individuals that come into contact with susceptible individuals transmit infection at rate β and infectious individuals recover at rate γ .

However, with increasing evidence supporting the existence of non-random structure in empirical networks [107], and with knowledge that many real-world networks occur in space, network-based studies must consider any structural features of the network that influence the outcome on a global scale. Incorporating such structure into network-based models prevents researchers from making strong unifying assumptions, which in turn complicates the modelling and analyses processes. Thus, improved models, modelling techniques and analytical approaches are required.

In the first piece of research, contained in Chapter 2, a complex network comprised of two types (excitatory and inhibitory) of nodes describing neurons that are assigned fixed locations in space is considered. The dynamical processes modelled are i) the development of the network's structure over time, where each neuron has a variable neuritic radius determining the connections it forms with other neurons in the network, and ii) the electrical activity of neurons over time, where each individual neuron strives to maintain a set level of electrical activity by increasing or decreasing its neuritic radius, altering the strength of connections it makes with other excitatory and inhibitory neurons in the network and thus the level of electrical input it receives. Various spatial arrangements of the two types of neurons are considered and tested to determine how specific distributions of the neuron types influence the connection structure and electrical activity of the network on a global scale.

In the second piece of research, contained in Chapter 3, model equations are derived which describe the dynamics in time of an SIR epidemic occurring on a complex network, where individuals exhibit heterogeneity in the structure, duration and type of connections made with other individuals. Namely, the model has an entirely static network layer with its permanent connection structure being determined by two degree distributions, allowing for varying levels of clustering to be considered. The network has a secondary network layer, meaning the network can be considered as *multiplex*, where all such connections rewire at a constant rate, generating an entirely dynamic network layer with finite durations for each connection made. The model equations incorporate various parameters as inputs such that distinct local spatial structures can be considered and the resultant epidemic dynamics studied.

In the third piece of research, contained in Chapter 4, pairwise model equations reflecting the dynamics of an SIR epidemic occurring on a clustered complex network are considered. The model equations incorporate the global clustering coefficient, meaning that a range of clustering coefficients $\in [0, 1]$ can be tested and the resultant dynamics

analysed. A novel analytical approach is taken to derive expressions for the epidemic threshold in two variants of the pairwise model, which are approximated and then validated by comparison to epidemic threshold expressions derived via alternative methods.

Although all of the research contained in Chapters 2-4 utilises the same underlying mathematical formalism and considers the effects of local spatial structure on global dynamics, there are some clear differences between the analytical approaches typical of neuroscience and epidemiology. When considering activity in the brain, research tends to focus on ‘healthy’ and ‘pathological’ activity states [101]. In a healthy state, the brain’s activity is characterised by unstable oscillatory behaviour generated by individual firing neurons that operates within a stable regime on a global scale. Pathological network activity, for example in patients with epilepsy, can be characterised as abnormally excessive or synchronous neuronal activity [27]. In a neuroscience-based network study, one might study the effects on electrical activity of specific structural motifs in the network of neurons or investigate the mechanisms that enable the network of neurons to remain within healthy operational regimes. Further, researchers can consider what kind of techniques could be used to treat patients who experience pathological brain activity.

On the other hand, researchers who study the dynamics of infectious diseases are most interested in the extreme cases of an epidemic process. They ask questions such as: *under what conditions will the epidemic persist and spread, and under what conditions will it stop spreading?* These kind of questions lead epidemiologists to consider mathematical expressions for epidemic thresholds, above which the epidemic is expected to spread and below which it is expected to die out. Epidemic thresholds can incorporate disease transmission rates and information regarding the network’s contact structure. Considering the original compartmental SIR model governed by equations (1.1)-(1.3), the epidemic threshold can be expressed as $R_0 = \beta/\gamma$, which is commonly referred to as the basic reproduction number and describes the expected number of new infections caused by a single infectious individual in an otherwise susceptible population.

In the neuroscience-based model considered in Chapter 2, each neuron is modelled as having a variable level of electrical activity within a bounded, continuous and closed range. In contrast, both of the epidemiological-based models (Chapters 3 and 4 respectively) consider nodes to be in one of three discrete states, indicated by the disease compartments in Figure 1.3. Although the neuroscience-based research in Chapter 2 is restricted to considering a neuron’s activity levels to exist within a continuous range, it is also possible to describe a neuron’s activity by transitions between discrete states. For example, a

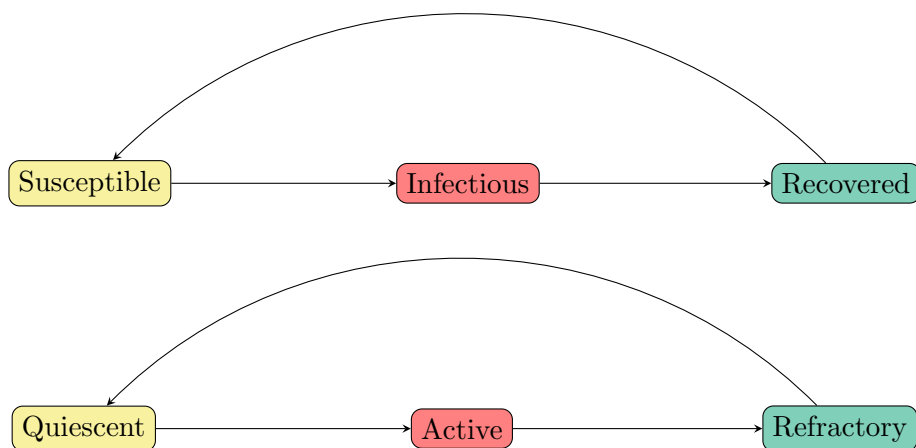


Figure 1.4: Flow diagram representing the compartments and transitions possible within the basic SIRS (upper) and QARQ (lower) compartmental models

neuron can be considered as being initially quiescent (Q), followed by becoming activated (A) during firing and subsequently entering a period of refraction (R), before returning to the initial quiescent state. This QARQ model can be considered similarly to the SIRS epidemic model which describes a disease transmission model that is very similar to the SIR model, but where individuals can return to the susceptible (S) disease state following a period of recovery (R) from infection (Figure 1.4).

Although the statuses of neurons within a developing neural network and individuals in a social network during an epidemic can be characterised in a similar way, these scenarios diverge when transmission dynamics are considered (e.g. how do neurons or individuals cause neighbouring neurons or individuals to change states?). In epidemiology the typical approach is to assume that a disease-spreading contact between a susceptible and an infectious individual occurs at a given rate. It is also typical to assume that infectious individuals recover from infection at a given rate. However, in neuroscience, a common approach is to consider ‘integrate-and-fire’ neuronal models [11, 12] whereby a neuron receives excitatory and inhibitory inputs from other neurons, and a neuron only transitions from quiescent to activated (or from not-firing to firing) when its electrical activity (or membrane potential) exceeds a threshold value, upon which an action potential or spike in the neuron’s activity is generated. A neuron is then considered to transition from the activated state to the refractory state at a given rate, once it completes its firing activity.

A common theme across all three pieces of research in Chapters 2-4 is the consideration of local spatial structure and its influence on the dynamic process being modelled at a global scale. Specifically, the challenge here in considering both neuronal and epidemiological dynamics is to utilise and analyse models where the network structure exhibits

spatial embedding (for the neuronal network model, see Chapter 2) or the network exhibits complex local structure such as clustering (for the epidemic network models, see Chapters 3 and 4).

1.3 Thesis structure

The remaining chapters of this thesis are structured as follows. In Chapter 2, a published model [119] is considered which describes the activity-dependent growth and development of a network of excitatory and inhibitory neurons embedded in Euclidean space. A systematic investigation into the effect of various spatial arrangements of excitatory and inhibitory neurons on the global dynamics of the network is performed. In this setting, the physical locations of the neurons influence the network's topology which in turn influences the electrical activity of each neuron. The electrical activity of each neuron also influences the neuron's local network topology: each neuron increases or decreases the size of its neuritic field, which determines a neuron's connection structure and strengths, to increase or decrease electrical input until a homeostatic set point for electrical activity can be reached by all neurons in the system simultaneously. As well as considering the dynamic balance between the amount of excitation and inhibition in the network (called the E/I balance), it is demonstrated that the spatial arrangement of the neurons is also an important factor in determining global outcome. Further, measures for inhibitory clustering within one- and two-dimensional lattice structures with periodic boundary conditions are defined, supporting the discovery that increased inhibitory clustering leads to unstable, oscillatory behaviour on a global scale in the model. Previous research had shown that different spatial arrangements of neurons led to distinct outcomes, but no systematic investigation into such spatial arrangements was published prior to this work.

In the second piece of research, contained in Chapter 3, novel model equations are derived, following the existing edge-based compartmental modelling approach [124, 73, 74, 77]. The model equations describe an SIR epidemic spreading on a multiplex network comprised of two layers that represent i) an individual's permanent connections to their local community and ii) transient connections made with other members of the population. This work combines two existing edge-based compartmental models into a single set of equations, allowing for a network-based model with a combination of static and dynamic network architecture. The basic reproduction number, describing the average number of infectious cases generated by a single infectious individual in an otherwise susceptible population, is derived, and this is validated and tested alongside the model equations

describing the prevalence of each disease compartment over time. The original abstract for this piece of research is as follows:

The duration, type and structure of connections between individuals in real-world populations play a crucial role in how diseases invade and spread. Here, we incorporate the aforementioned heterogeneities into a model by considering a dual-layer static-dynamic multiplex network. The static network layer affords tunable clustering and describes an individual's permanent community structure. The dynamic network layer describes the transient connections an individual makes with members of the wider population by imposing constant edge rewiring. We follow the edge-based compartmental modelling approach to derive equations describing the evolution of a susceptible-infected-recovered epidemic spreading through this multiplex network of individuals. We derive the basic reproduction number, measuring the expected number of new infectious cases caused by a single infectious individual in an otherwise susceptible population. We validate model equations by showing convergence to pre-existing edge-based compartmental model equations in limiting cases and by comparison with stochastically simulated epidemics. We explore the effects of altering model parameters and multiplex network attributes on resultant epidemic dynamics. We validate the basic reproduction number by plotting its value against associated final epidemic sizes measured from simulation and predicted by model equations for a number of setups. Further, we explore the effect of varying individual model parameters on the basic reproduction number. We conclude with a discussion of the significance and interpretation of the model and its relation to existing research literature. We highlight intrinsic limitations and potential extensions of the present model and outline future research considerations, both experimental and theoretical.

In the third piece of research, contained in Chapter 4, the epidemic threshold is considered in pairwise/correlation models [94, 54] describing an SIR epidemic process on clustered and regular networks. Analytic expressions for the epidemic threshold are obtained by utilising a novel analytical approach which exploits the presence of two fast variables related to the correlation structure that develops in the network as the epidemic spreads. Two analytic threshold expressions are derived and approximated, for two distinct pairwise model closures, and both expressions are validated numerically. Detailed calculations are provided in Appendices 4.A-4.D. The abstract for this piece of research is

given as follows:

The epidemic threshold is probably the most studied quantity in the modelling of epidemics on networks. For a large class of networks and dynamics the epidemic threshold is well studied and understood. However, it is less so for clustered networks where theoretical results are mostly limited to idealised networks. In this paper we focus on a class of models known as pairwise models where, to our knowledge, no analytical result for the epidemic threshold exists. We show that by exploiting the presence of fast variables and using some standard techniques from perturbation theory we are able to obtain the epidemic threshold analytically. We validate this new threshold by comparing it to the numerical solution of the full system. The agreement is found to be excellent over a wide range of values of the clustering coefficient, transmission rate and average degree of the network. Interestingly, we find that the analytical form of the threshold depends on the choice of closure, highlighting the importance of model choice when dealing with real-world epidemics. Nevertheless, we expect that our method will extend to other systems in which fast variables are present.

This thesis concludes with a discussion, contained in Chapter 5, which summarises the research and results within Chapters 2-4 and discusses the implications of the work presented, alongside considerations of potential improvements to the work, future research ideas and interesting open questions related to the research of complex systems.

Chapter 2

Clustered arrangement of inhibitory neurons can lead to oscillatory dynamics in a model of activity-dependent structural plasticity

2.1 Introduction

Neuronal networks continuously undergo changes in their connectivity. This structural plasticity starts with development and continues throughout adulthood. It is typically supported by experience-dependent mechanisms. In computational neuroscience, a number of mathematical models of activity-dependent structural plasticity have been developed to further our understanding of the formation, function, and underlying structure of neuronal networks [90]. These models operate on the assumption that network structure results from a number of activity-dependent processes such as neurite outgrowth and growth cone behaviour [16, 26, 100], and naturally occurring cell death [87, 25]. It has been shown that combining the Shunting model [38], describing the neuronal activity of a group of neurons, with terms describing activity-dependent outgrowth, in which initially disconnected neurons organise themselves into a network under the influence of endogenous activity, results in a model that can display complex periodic behaviour of electrical activity and connectivity, including small-amplitude stable oscillations and intermittent

unstable burst-like oscillations [118, 120]. A unifying assumption of this so-called Extended Shunting model (ES model hereafter) is the homeostatic regulation of neuronal excitability toward a target level, a phenomenon which is considered ubiquitous in both development and adulthood [114, 41]. Such a mechanism allows neurons to maintain stability of function whilst undergoing significant anatomical and functional changes and it plays a key role in network growth and stability.

Early neural network formation depends on a number of factors: (1) neurotrophic substances exerting chemoattraction and chemorepulsion, (2) neurotransmitters, most notably glutamate (an excitatory transmitter), GABA (classically inhibitory transmitter but may be temporarily excitatory during early development), glycine, and taurine, and (3) neural network activity. It is important to note that neurotransmitters can act directly on the network growth through modulation of intracellular calcium [42] and also indirectly through synaptic mechanisms causing depolarisation (excitation) and hyperpolarisation (inhibition) of the target neuron and thus modulation of neuronal activity [21, 128, 65]. It is the third mechanism of network activity-dependent growth that the ES model considers and in particular the balance between excitation and inhibition in a neuronal network, which plays a crucial role in determining the stability and computational effectiveness of the network [40]. Animal and human studies have shown that the disruption of excitatory and inhibitory neurotransmitter levels results in neural migration disorders and epilepsy [65]; furthermore it is noted that some human genetic disorders are associated with excessive inhibition in the brain [31]. Previous work involving the ES model emphasised the importance of the balance between excitation and inhibition, suggesting that a network developing under conditions of relatively high inhibition is more likely to end up in a pathological state with oscillatory behaviour, whereas a network developing under a low level of inhibition during its development enables the system to move to the normal state, where the network structure reaches a stable end state with stable levels of activity [120]. The oscillatory behaviour induced by moderate proportions of inhibition was thought to be a result of interactions between excitatory and inhibitory activities, occurring on the timescale of the electrical activity [119].

Central to this chapter is another factor that has been identified as affecting system behaviour beyond the proportion of inhibitory neurons: namely, the spatial arrangement of inhibitory neurons [119]. The developmental migration of inhibitory neurons within the central nervous system was thought to be spatially random [2, 110]. Recent studies, however, demonstrate that during neural development clusters of inhibitory neurons form.

The result of this inhibitory clustering is the production of higher amplitude inhibitory postsynaptic potentials (IPSPs) within excitatory neurons [8, 15].

Under neural activity homeostasis, neural inhibition will induce outgrowth and allow disconnected subnetworks to become connected. We therefore hypothesise that the spatial distribution of inhibitory neurons will play an important role in the interaction between structure and function. When highly clustered inhibitory cells (with self-inhibition) become electrically inhibited, outgrowth of inhibitory neurons is stimulated (as their activity is below the homeostatic target value), inducing long-range inhibition within the whole network. This in turn means that these networks develop stronger excitatory-excitatory, excitatory-inhibitory (and inhibitory-excitatory) connectivity, and as a result, possibly increased network instability.

A comprehensive account of the extent to which the spatial organisation of excitatory and inhibitory neurons influences global system behaviour and the structural characteristics of the resulting neuronal networks is lacking. Such an account is made necessary by a growing body of evidence suggesting the presence of nonrandom network attributes within neuronal network structures, including modular community structure, short characteristic path length (associated with high global efficiency of information transfer), high levels of clustering (i.e., the propensity for neighbours of a random neuron to share a connection, associated with robustness to random error), and degree distributions compatible with the existence of highly connected hub neurons [10, 107, 117]. In this chapter, we investigate how much influence the spatial arrangement of excitatory and inhibitory neurons, and more specifically, the spatial clustering of inhibitory neurons, has on the global system dynamics, network structure, and electrical activity in the ES model.

In what follows, we begin by outlining the differential equations governing the activity-dependent neuronal network growth model, giving a detailed description of each model element, and explaining how these elements combine to create a system in which each and every neuron strives to maintain a desired level of electrical activity (homeostasis). We explain the choice of model parameters, describe the implementation of the numerical scheme used to solve the resulting system of ordinary differential equations (ODEs), and outline the terminologies and notation used throughout this chapter. We define novel methods for measuring the extent of inhibitory clustering within one- and two-dimensional (1D and 2D) lattice networks composed of various neuron arrangements. The lattice networks have periodic boundary conditions, i.e., they are mapped onto a torus, thus approximating large systems. In Section 2.5, we show that the proportion of inhibitory neurons alone is

a necessary but not sufficient condition for inducing network instability characterised by oscillatory behaviour of the connectivity and electrical activity. By considering $1D$ and $2D$ networks we are able to demonstrate that in general, higher levels of spatial clustering of inhibition induce oscillatory behaviours, whilst lower levels of inhibitory clustering lead to a final, stable end state. We look at the qualitatively distinct global system behaviours produced by the ES model and attempt to understand whether different system behaviours translate into different underlying network structures. This is done by using network theoretical measures and by comparing these across networks corresponding to different system behaviours. We conclude with a discussion of our findings including neurodevelopmental parallels and suggestions for future experimental and computational work in the field.

2.2 Model

This work is based on the model of structural plasticity proposed by Van Ooyen et al. [119]. It extends the Shunting model proposed by Grossberg [38] by incorporating activity-dependent outgrowth terms. This allows a network containing excitatory and inhibitory neurons to be grown from initial conditions. Each neuron is assigned a unique spatial location (see Subsection 2.4.2) and modelled with a variable radius, denoting the area of its neuritic (axonal and dendritic) extensions. When the circular fields of two neurons overlap, those neurons become connected with a strength proportional to the area of overlap, multiplied by the appropriate synaptic efficacy term, determined by the type (excitatory or inhibitory) of the two neurons.

Precisely, the system is governed by the following dimensionless coupled differential equations describing the rate of change of electrical activity (denoted $(X_i)_{i=1,\dots,N}$ and $(Y_j)_{j=N+1,\dots,N+M}$) and neuritic radii (denoted $(R_i)_{i=1,\dots,N}$ and $(R_j)_{j=N+1,\dots,N+M}$) of N excitatory and M inhibitory neurons respectively:

$$\frac{dX_i}{dT} = -X_i + (1 - X_i) \sum_{k=1}^N W_{ik} F(X_k) - (H + X_i) \sum_{l=N+1}^{N+M} W_{il} F(Y_l) \quad (2.1)$$

$$\frac{dY_j}{dT} = -Y_j + (1 - Y_j) \sum_{k=1}^N W_{jk} F(X_k) - (H + Y_j) \sum_{l=N+1}^{N+M} W_{jl} F(Y_l) \quad (2.2)$$

$$\frac{dR_i}{dT} = \rho G(F(X_i)) \quad (2.3)$$

$$\frac{dR_j}{dT} = \rho G(F(Y_j)). \quad (2.4)$$

Equations (2.1) and (2.2) correspond to the original Shunting model, where X_i and Y_j

Parameter name	Parameter description	Default parameter value
ρ	Rate of growth of neuritic field	0.0001
θ	Firing threshold for firing rate function F	0.5
α	Slope of firing rate function F	0.1
β	Slope of growth function G	0.1
ϵ	Threshold for growth function G	0.6
H	Ratio between minimum and maximum electrical activity values	0.1
S_{ee}	Excitatory to excitatory synaptic efficacy	1
S_{ei}	Inhibitory to excitatory synaptic efficacy	1
S_{ie}	Excitatory to inhibitory synaptic efficacy	1
S_{ii}	Inhibitory to inhibitory synaptic efficacy	1

Table 2.1: Default values for all model parameters used in simulations

refer to the electrical activity of excitatory neuron i and inhibitory neuron j , respectively, expressed in units of a saturation value (finite maximum). Electrical activities have a finite minimum, i.e., $-H$ times the saturation value. A change in electrical activity of a neuron is influenced by its own electrical activity and that of any other neuron it shares a connection with. The strength of the connection between neurons i and j at any point in time is given by element W_{ij} of the (symmetric) weight matrix \mathbf{W} . In this weight matrix, self-overlap terms are set to zero ($W_{ii} = 0, \forall i \in \{1, \dots, N+M\}$) and non-diagonal elements are calculated as

$$W_{ij} = A_{ij}S_{[i][j]}, \quad (2.5)$$

where A_{ij} describes the area of overlap between the circular neuritic fields of neurons i and j , and $S_{[i][j]}$ describes a synaptic strength parameter from a neuron of type (excitatory or inhibitory) $[j]$ to a neuron of type $[i]$.

Equations (2.3) and (2.4) result from extending the Shunting model to incorporate activity dependency of neurite outgrowth. R_i and R_j denote the radii of the neuritic field of excitatory neuron $i \in \{1, \dots, N\}$ and inhibitory neuron $j \in \{N+1, \dots, L = N+M\}$, respectively. Parameter ρ describes the rate of outgrowth of the neuritic radii (ρ is constant in our analyses) and the functions F and G are continuous saturating functions:

$$F(u) = \frac{1}{1 + e^{(\theta-u)/\alpha}} \quad (2.6)$$

$$G(u) = 1 - \frac{2}{1 + e^{(\epsilon-u)/\beta}}. \quad (2.7)$$

The function F can be thought of as governing the mean firing rate of each neuron, with values in the bounded range $(0, 1)$. The function G describes the growth rate of a

neuron as a function of the neuron's firing rate and has values in the range $(-1, 1)$. The role and default values of parameters θ , α , ϵ , and β are given in Table 2.1. The value of ϵ has great influence on system behaviour, since each neuron attempts to maintain electrical activity equal to ϵ . When a neuron's electrical activity stabilises at ϵ , the growth function G tends to zero and the neuritic radius will cease to change. If all neurons in the system are able to maintain an electrical activity equal to ϵ simultaneously, a system steady state is reached.

2.3 Model implementation

All simulations were implemented in the MATLAB environment, using a variable-order stiff ODE solver (*ode15s*). Initial conditions were specified, consisting of the spatial location of all neurons within the system and the value of each neuron's radius and electrical activity at time zero. In the 1D model, neurons were placed onto lattice positions on a line with periodic boundary conditions, leaving a nominal distance of 1 between each neuron pair. In the 2D model, a square number $L = N + M$ of neurons were assigned positions on a square lattice with periodic boundary conditions, with every adjacent pair of neurons being separated by nominal distance 1. In both 1D and 2D models, initial electrical activity values were set to zero for all neurons. Different scenarios of initial radii values were used as specified in each of the relevant sections. These included:

- Randomly (uniformly) generated values in the range $(0, 0.6)$ creating an initially largely disconnected network
- Identical values (radii=0.4) creating a totally disconnected network
- Identical values (radii=0.6) for a 1D ring network in which each neuron is only connected to its two immediate neighbours.

We imposed that all neuritic radii be greater than or equal to zero at all times. The ODE system was solved until system behaviour could be clearly identified (typically up to a time $> 10^5$).

2.4 Methods

2.4.1 Parameter choice

Our analyses used similar parameters to those used by Van Ooyen et al. [119] and are summarised in Table 2.1. They differed in two respects. First, whereas Van Ooyen et al.

set the proportion of inhibitory neurons in the range of 10% – 20%, in accordance with in vivo observations in various brain regions [119], we systematically varied this proportion in order to provide a fuller picture of system behaviour in relation to the balance between excitation and inhibition (see also the next subsection). Second, for simplicity, we kept the synaptic efficacy parameters (S_{ee} , S_{ei} , S_{ie} and S_{ii}) identical throughout.

2.4.2 Spatial arrangement of excitatory and inhibitory neurons

Since connectivity is determined by the amount of overlap between neuritic fields centred over fixed neuron locations, it follows that the joint degree¹ distributions for X (excitatory) and Y (inhibitory) neurons will strongly depend on the spatial arrangement of these neurons, and particularly, whether they are well mixed or clustered – an operational definition of this clustering will be given in the following subsection. We used a systematic approach to building 1D arrangements of excitatory and inhibitory neurons assigned to lattice positions. We define a tile as a single row of $l \in \mathbb{Z}^+$ neurons, with nominal distance 1 between consecutive neurons. Then, complex 1D networks with periodic boundary conditions could be formed by duplicating tiles a specified number of times. For example, a network of size $L = 12$ with a 1/3 proportion of inhibitory neurons could consist of a single tile of length $l = 12$ with 4 inhibitory neurons or 4 identical tiles of length $l = 3$ with 1 inhibitory neuron each (see example neuron arrangement in subsequent paragraph). The use of periodic boundary conditions means that any pair of neurons in the network will be at most $L/2 = (1/2 \times \text{number of neurons in the network})$ distance away from one another. 2D arrangements of N excitatory and M inhibitory neurons were generated in MATLAB using random permutations of a vector containing N zeros and M ones, and reshaping the resulting column vector of size $L \times 1$ into a matrix of size $\sqrt{L} \times \sqrt{L}$.

When representing spatial arrangements throughout the text in this chapter, we use filled circles to denote inhibitory neurons and empty circles to denote excitatory neurons, e.g., $\bullet \circ \circ \bullet \circ \circ \bullet \circ \circ \bullet \circ \circ$. In Figure legends, neuron arrangements are represented using red circles in various hues to denote inhibitory neurons and blue circles in various hues to denote excitatory neurons. The use of unique colours enables the reader to make a direct comparison between each neuron’s spatial location and the associated dynamics of their neuritic radius and electrical activity.

¹The degree of a node in a network is the number of connections it has to other nodes in the network. The joint degree distribution describes the probability distribution of connections between nodes of degree k_1 and nodes of degree k_2 over the whole network.

2.4.3 Measuring spatial clustering of inhibition in 1D and 2D neuron arrangements

Measuring the clustering of inhibitory neurons in spatial arrangements of both excitatory and inhibitory neurons is not straightforward, and we are not aware of any established method for quantifying it. In what follows, we define measures for clustering in 1D and 2D lattice networks as defined previously.

1D inhibitory clustering measure

We define a measure of inhibitory clustering in a 1D network of neurons assigned to lattice positions with periodic boundary conditions as

$$C_{1D} = \frac{1}{D} \left(\sum_{i=1}^D \frac{1}{i^2} N_{i-1} \right), \quad (2.8)$$

where D is the shortest distance between the first and last inhibitory neurons in the network, taking periodic boundary conditions into account, and N_i denotes the number of pairs of inhibitory neurons with i excitatory neurons separating them. N_i is consistently counted without multiplicity, meaning that the total N_i count will always be equal to $(M - 1)$ with M inhibitory neurons, and any N_i pairs of inhibitory neurons should not have another inhibitory neuron in between them. For example, network $\bullet \bullet \circ \circ \bullet \circ \circ \circ \circ$ has $D = 4$, $N_0 = 1$ (the only adjacent pair of inhibitory neurons), $N_2 = 1$ (the single pair of inhibitory neurons separated by 2 excitatory neurons), and $N_1 = N_3 = N_4 = 0$ leading to a clustering value of $C_{1D} = \frac{1}{4} \left(\frac{1}{1} 1 + \frac{1}{3^2} 1 \right) = \frac{10}{36}$. The inhibitory clustering measure takes value 1 when the greatest possible level of inhibitory clustering is achieved in a network, i.e., when all inhibitory neurons are adjacent to one another and hence $N_0 = D$, and its value tends toward zero as the extent of inhibitory clustering decreases. The contribution of inhibitory neuron pairs decays with the number of excitatory neurons separating them. The weighting factor was selected as a trade-off between an insufficient penalty for the spreading out of inhibitory neurons (e.g., $1/i$) and insensitivity to subtle variations in the structure of the network (e.g., $1/i^3$), hence our choice of $1/i^2$.

2D inhibitory clustering measure

We define a measure of inhibitory clustering for a 2D lattice network containing L neurons with M inhibitory neurons and periodic boundary conditions as follows:

$$C_{2D} = 1 - \frac{WH}{L} \left[\sum_{R=r_1}^{r_n} N_{R_W R_H} \left(\frac{R_W R_H}{(WH - M)} \right)^2 \right] \quad (2.9)$$

where one firstly computes the smallest possible “covering rectangle” of width W and height H which covers all M lattice positions of inhibitory neurons, taking continuous boundary conditions into account, followed by decomposing all WH neurons contained *within* the covering rectangle into $n \in \mathbb{Z}^+$ inhibitory-empty rectangles of various dimensions, from the largest possible rectangle of size $(W-1) \times H$ or $W \times (H-1)$, to the smallest possible rectangle of size 1×1 , containing a single neuron. In each case, the width and height of a rectangle are equal to the *number* of neurons along the width and height of the rectangle, respectively. Each inhibitory-empty rectangle is counted without replacement. R_W and R_H denote the width and height of rectangle R and the term $N_{R_W R_H}$ denotes the *number* of inhibitory-empty rectangles of size $R_W \times R_H$ contained within the covering rectangle. If a covering rectangle contains no excitatory neurons, the summation term will be equal to zero and hence $C_{2D} = 1$.

2.5 Results

2.5.1 1D results

The proportion of inhibitory neurons – a necessary condition for global system behaviour

In our analyses, it was found that the proportion of inhibition alone cannot accurately predict the system’s global behaviour. Simulations with tile size 13 were implemented where the proportion of inhibition in the system was set to $4/13 \approx 30.77\%$ with all other parameters held constant, bar the placement of neurons. For the initial conditions, all electrical activity values were set to zero, and all neuritic radii values were set to 0.4, creating a wholly disconnected network. A number of spatial arrangements were considered, randomly picked from a set of unique tile arrangements generated by a MATLAB script that selected at random M out of L positions for inhibitory neurons, and placed N excitatory neurons onto the remaining lattice positions (note that a more systematic approach is used in the following subsection).

Three qualitatively distinct global behaviours are found (Figure 2.1), namely (1) stable periodic oscillations of small amplitude of both network structure and electrical activity (Figure 2.1 A and B), (2) large amplitude unstable oscillations in the network structure and unstable burst-like oscillations in electrical activity (Figure 2.1 C and D), and (3) complete stabilisation of both network structure and electrical activity (Figure 2.1 E and F), all occurring after an initial period of overshoot and pruning of connections.

Since all networks were initialised with identical neuritic field sizes and electrical activities, we conclude that varying the spatial arrangement of neurons within the network can induce distinct global behaviours. The proportion of inhibition alone may be a necessary but not sufficient condition to induce oscillatory system behaviour. The relationship between E/I ratio, spatial arrangement, and the occurrence of oscillations in the ES model is nontrivial and cannot be attributed to any single characteristic. As pointed out by Van Ooyen and Van Pelt [118], oscillations can arise as a result of the hysteresis loop formed by the coupling between network structure and electrical activity in the ES model, or due to fluctuations in the *effective* E/I ratio, i.e., the dynamically emerging ratio of total excitatory to inhibitory connectivity, irrespective of the fixed number of excitatory and inhibitory neurons in the arrangement.

The effect of inhibitory clustering on global system behaviour in 1D

The occurrence of different global behaviours when the proportion of inhibitory neurons in a tile is fixed and simulations of various spatial arrangements are run (Figure 2.1) suggests that some feature of spatial organisation of neurons (and specifically inhibitory neurons) could impact the presence of oscillatory behaviour. As most models typically assume a well-mixed population, here, we focus on the possibility that inter-inhibitory connectivity induced by spatial clustering of inhibitory neurons could be an important determinant.

Simulations with fixed tile size and number of inhibitory neurons, but various levels of inhibitory clustering, revealed distinct global behaviours and a trend suggesting that networks with a higher clustering measure are more likely to experience oscillatory behaviours (Table 2.2). In networks containing three inhibitory neurons and seven excitatory neurons (Figure 2.2), the most extreme oscillatory behaviour is observed when inhibitory clustering is at its greatest (Figure 2.2 A and B). In this case, the network structure and electrical activities experienced a bout of periodic oscillations, before developing unstable burst-like oscillations of much greater amplitude. As the extent of inhibitory clustering decreases slightly, the system experiences stable oscillations with a smaller amplitude, in

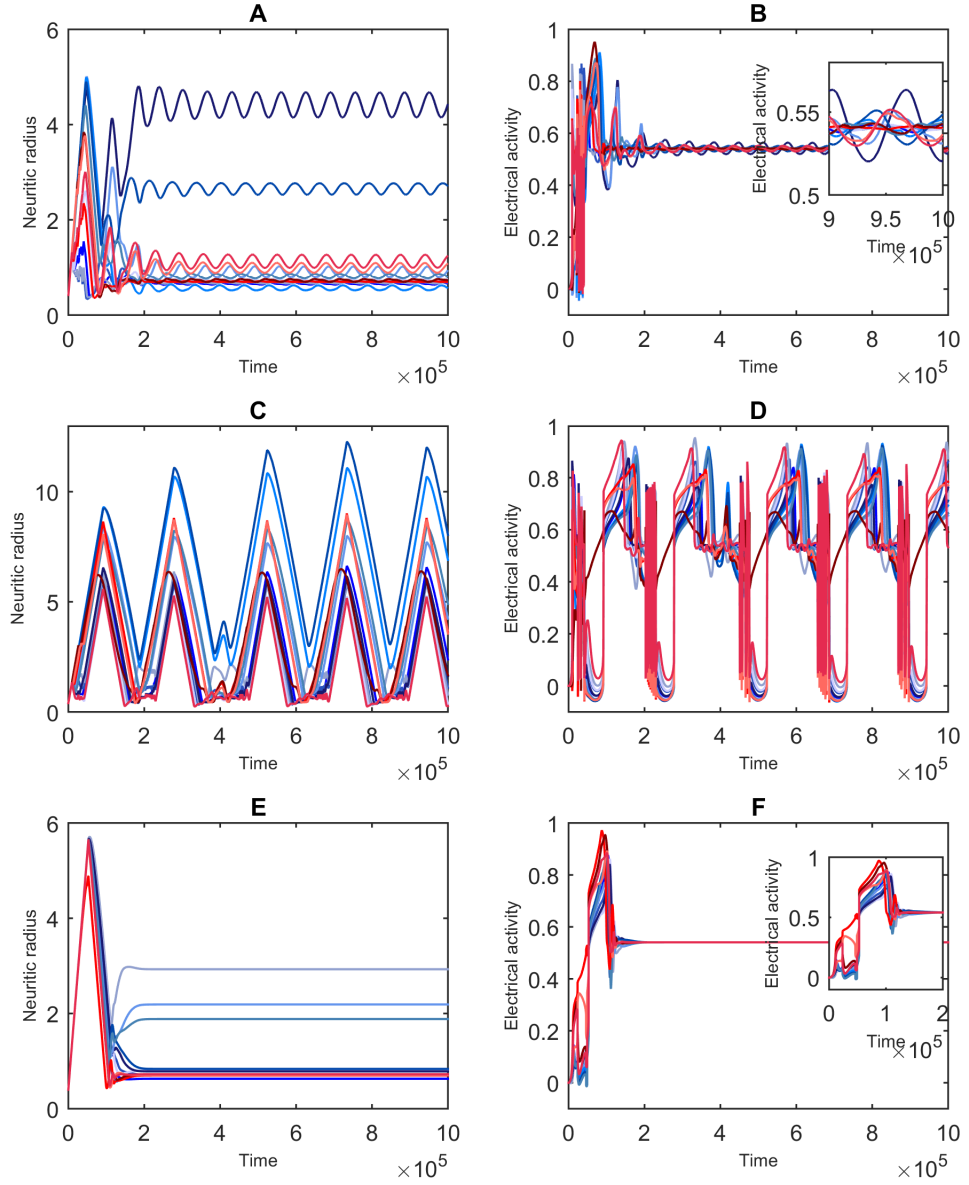


Figure 2.1: **Global system behaviour of mixed 1D lattice networks with various spatial arrangements of neurons.** In all cases $L = 13$, $N = 9$, $M = 4$ and default parameters listed in Table 2.1 are used. The networks are initially wholly disconnected and neurons are at rest. Figures on the *left-hand side* depict the dynamics of the individual neuritic radii values; figures on the *right-hand side* depict the dynamics of the individual electrical activity values. Neuron arrangements are as follows: ●●●●●●●●● (A,B), ●●●●●●●●● (C,D), ●●●●●●●●● (E,F).

both network structure and electrical activity (Figure 2.2 C and D). Here, an idiosyncratic behaviour of the ES model is observed whereby the largest neuritic field in the network continues to grow whilst experiencing stable oscillations (Figure 2.2 C). This behaviour results from the fact that once the neuron's field completely overlaps those of every other

neuron in the network, further growth has no effect on the connection strengths to itself and others and outgrowth continues unbounded. Eventually, the inhibitory neurons become more evenly distributed across the lattice positions and the neuritic radii and their associated electrical activity experience complete stabilisation (Figure 2.2 E-H). An exhaustive list (taking symmetries and reflections into account) of all possible spatial configurations for tile sizes 8, 10, and 14, containing 2, 3, and 4 inhibitory neurons, respectively, also suggests that higher inhibitory clustering increases the likelihood of oscillatory behaviour being observed (Table 2.2).

A systematic mapping of the relationship between inhibitory clustering and the proportion of inhibitory neurons reveal the emergence of distinct regimes (Figure 2.3). There are no significant differences for the regimes observed between simulations with initially disconnected networks (radii=0.4, Figure 2.3 A) and those starting with a regular ring network (radii=0.6, Figure 2.3 B). Networks with lower proportions of inhibitory neurons and lower clustering values are more likely to experience complete stabilisation of electrical activity and network structure. However, a handful of configurations with high inhibitory clustering and low proportions of inhibitory neurons also experienced complete stabilisation. In general, as inhibitory clustering increases, systems developed oscillatory behaviours. We observe that the oscillatory regime also extends into slightly higher proportions of inhibitory neurons than the stabilisation regime. Past the oscillatory regime, with the highest proportions of inhibitory neurons, and a range of inhibitory clustering values, we see systems experience unbounded growth.

Table 2.2: Global system behaviour and clustering measure for mixed 1D simulations with various spatial arrangements. Default values were used on initially disconnected networks. S denotes stabilisation of the network and activity, SO denotes stable oscillatory behaviour, UO denotes unstable oscillatory behaviour, and TO denotes transient oscillatory behaviour. All 1D clustering measures are given as exact values or to four significant figures.

ID	Spatial arrangement	Tile size	%I	Behaviour	1D clustering measure
1	● ● ○ ○ ○ ○ ○ ○	8	25	SO	1
2	● ○ ● ○ ○ ○ ○ ○	8	25	S	0.125
3	● ○ ○ ● ○ ○ ○ ○	8	25	S	0.03704
4	● ○ ○ ○ ● ○ ○ ○	8	25	S	0.015625
5	● ● ● ○ ○ ○ ○ ○ ○ ○	10	30	UO	1
6	● ● ○ ● ○ ○ ○ ○ ○ ○	10	30	SO	0.4167
Continued on next page					

Table 2.2 – continued from previous page

ID	Spatial arrangement	Tile size	%I	Behaviour	1D clustering measure
7	● ● ○ ○ ● ○ ○ ○ ○ ○	10	30	SO	0.2778
8	● ○ ● ○ ● ○ ○ ○ ○ ○	10	30	S	0.125
9	● ● ○ ○ ○ ● ○ ○ ○ ○	10	30	SO	0.2125
10	● ○ ● ○ ○ ● ○ ○ ○ ○	10	30	S	0.07222
11	● ○ ● ○ ○ ○ ● ○ ○ ○	10	30	S	0.05208
12	● ○ ○ ● ○ ○ ● ○ ○ ○	10	30	S	0.03704
13	● ● ● ● ○ ○ ○ ○ ○ ○ ○ ○	14	28.57	SO	1
14	● ● ● ○ ● ○ ○ ○ ○ ○ ○ ○	14	28.57	UO	0.5625
15	● ● ○ ● ● ○ ○ ○ ○ ○ ○ ○	14	28.57	UO	0.5625
16	● ● ● ○ ○ ● ○ ○ ○ ○ ○ ○	14	28.57	UO	0.4222
17	● ● ○ ● ○ ● ○ ○ ○ ○ ○ ○	14	28.57	S	0.3
18	● ● ○ ○ ● ● ○ ○ ○ ○ ○ ○	14	28.57	SO	0.4222
19	● ○ ● ● ○ ● ○ ○ ○ ○ ○ ○	14	28.57	S,TO	0.3
20	● ● ● ○ ○ ○ ● ○ ○ ○ ○ ○	14	28.57	UO	0.3438
21	● ● ○ ● ○ ○ ● ○ ○ ○ ○ ○	14	28.57	S	0.2269
22	● ● ○ ○ ● ○ ● ○ ○ ○ ○ ○	14	28.57	SO	0.2269
23	● ● ○ ○ ○ ● ● ○ ○ ○ ○ ○	14	28.57	S	0.3438
24	● ○ ● ● ○ ○ ● ○ ○ ○ ○ ○	14	28.57	S	0.2269
25	● ○ ● ○ ● ○ ● ○ ○ ○ ○ ○	14	28.57	S	0.125
26	● ● ● ○ ○ ○ ○ ● ○ ○ ○ ○	14	28.57	UO	0.2914
27	● ● ○ ● ○ ○ ○ ● ○ ○ ○ ○	14	28.57	S	0.1875
28	● ● ○ ○ ● ○ ○ ● ○ ○ ○ ○	14	28.57	S,TO	0.1746
29	● ● ○ ○ ○ ● ○ ● ○ ○ ○ ○	14	28.57	S	0.1875
30	● ● ○ ○ ○ ○ ● ● ○ ○ ○ ○	14	28.57	S	0.2914
31	● ○ ● ● ○ ○ ○ ● ○ ○ ○ ○	14	28.57	S	0.1875
32	● ○ ● ○ ● ○ ○ ● ○ ○ ○ ○	14	28.57	S	0.08730
33	● ○ ● ○ ○ ● ○ ● ○ ○ ○ ○	14	28.57	S	0.08730
34	● ○ ○ ● ● ○ ○ ● ○ ○ ○ ○	14	28.57	S	0.1746
35	● ● ● ○ ○ ○ ○ ○ ● ○ ○ ○	14	28.57	SO (burst-like)	0.2535
36	● ● ○ ● ○ ○ ○ ○ ● ○ ○ ○	14	28.57	S	0.1613
37	● ● ○ ○ ● ○ ○ ○ ● ○ ○ ○	14	28.57	S	0.1467

Continued on next page

Table 2.2 – continued from previous page

ID	Spatial arrangement	Tile size	%I	Behaviour	1D clustering measure
38	● ● ○ ○ ○ ● ○ ○ ● ○ ○ ○ ○ ○	14	28.57	S	0.1467
39	● ● ○ ○ ○ ○ ● ○ ● ○ ○ ○ ○ ○	14	28.57	S	0.1613
40	● ● ○ ○ ○ ○ ○ ● ● ○ ○ ○ ○ ○	14	28.57	UO	0.2535
41	● ○ ● ● ○ ○ ○ ○ ● ○ ○ ○ ○ ○	14	28.57	S	0.1613
42	● ○ ● ○ ● ○ ○ ○ ● ○ ○ ○ ○ ○	14	28.57	S	0.07031
43	● ○ ● ○ ○ ● ○ ○ ● ○ ○ ○ ○ ○	14	28.57	S	0.05903
44	● ○ ● ○ ○ ○ ● ○ ● ○ ○ ○ ○ ○	14	28.57	S	0.07031
45	● ○ ○ ● ● ○ ○ ○ ● ○ ○ ○ ○ ○	14	28.57	S	0.1467
46	● ○ ○ ● ○ ● ○ ○ ● ○ ○ ○ ○ ○	14	28.57	S	0.05903

Is there an optimal proportion of inhibition for inducing oscillatory behaviour in 1D networks containing inhibitory clusters?

When high levels of inhibitory clustering are considered and networks are made up of repeated tile arrangements, thus creating network structures with one or more inhibitory clusters, a proportion of inhibitory neurons in the range [20%, 50%] induced oscillatory behaviour in both network structure and electrical activity (Figure 2.4). Within this range, some configurations experienced stable oscillations of network structure and electrical activity with small amplitudes, whilst the majority of other simulations experienced sustained unstable burst-like oscillatory behaviour of electrical activity and sustained unstable oscillations of neuritic radii values with larger amplitudes. For proportions of inhibition below 20%, all simulations experienced complete stabilisation of network structure and electrical activity. With a proportion of inhibition above 50%, the systems were unable to achieve the desired level of electrical activity for every neuron ($\epsilon = 0.6$). Neurons which are unable to achieve an electrical activity of ϵ experience unbounded growth of their neuritic field, with their electrical activity stabilising at a level below the homeostatic set-point. In such a situation, a stable network end state is unachievable. We see very similar regimes emerge when the starting network is either totally disconnected (Figure 2.4 A) or sparsely connected (Figure 2.4 B). In both cases, we observe a transition between stabilisation and oscillatory behaviours as the proportion of inhibition exceeds 20%, and between oscillatory behaviours and unbounded growth as the proportion of inhibitory neurons exceeds that

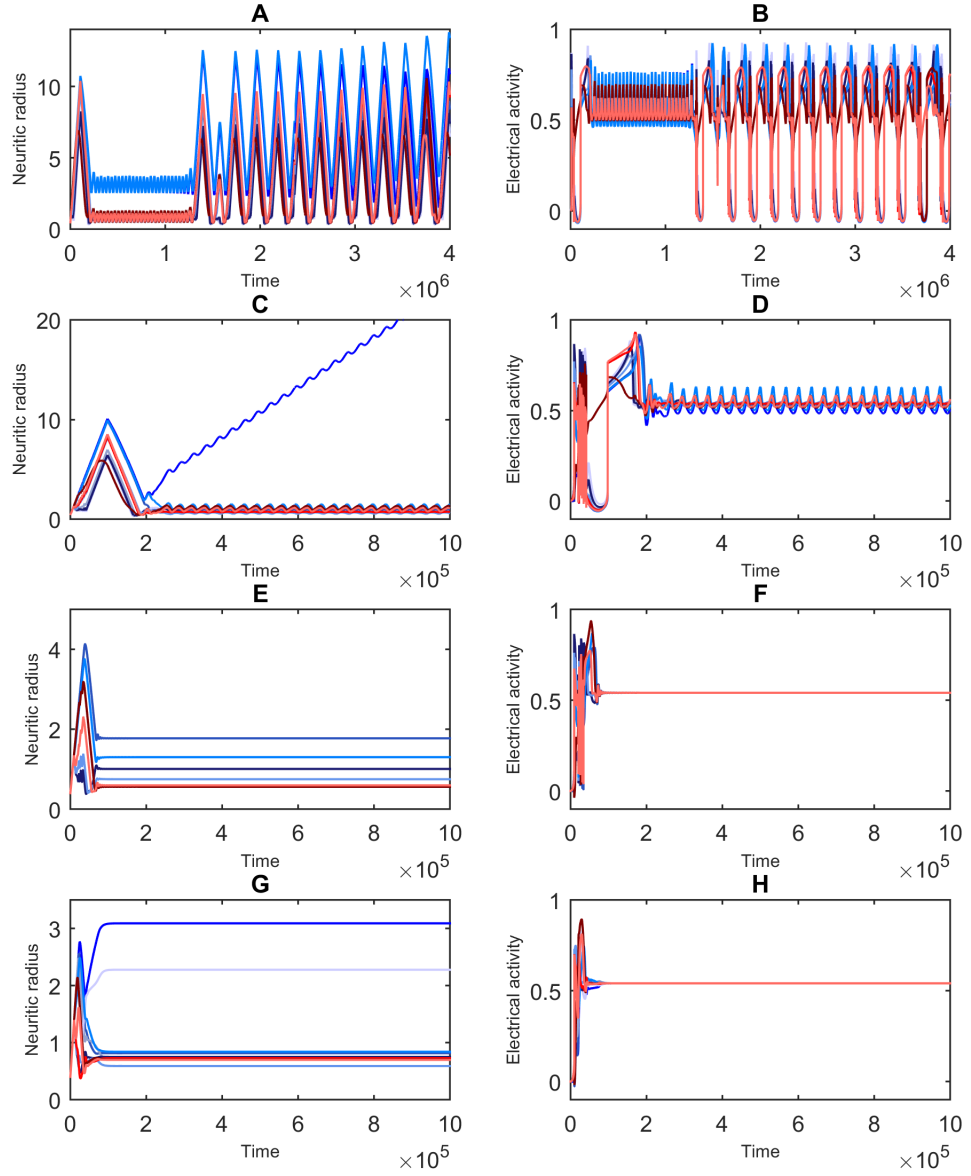


Figure 2.2: **Global system behaviour of mixed 1D lattice networks with various levels of inhibitory clustering.** In all cases, $L = 10$, $N = 7$, $M = 3$ and default parameters listed in Table 2.1 are used. The networks are initially wholly disconnected and neurons are at rest. Figures on the *left-hand side* depict the dynamics of the individual neuritic radii values; figures on the *right-hand side* depict the dynamics of the individual electrical activity values. Neuron arrangements are as follows: ● ● ● ● ● (A,B), ● ● ● ● ● (C,D), ● ● ● ● ● (E,F), ● ● ● ● ● (G,H).

of excitatory neurons.

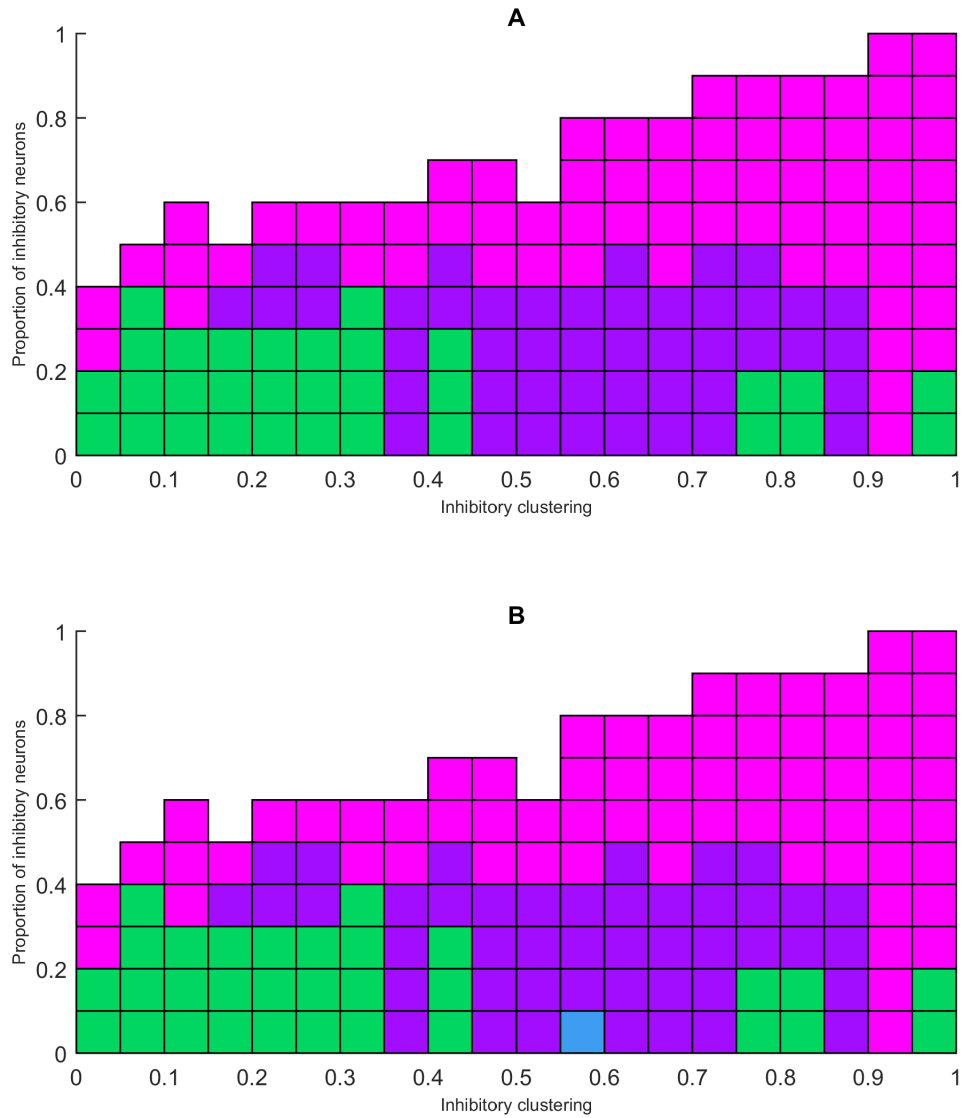


Figure 2.3: **1D system behaviours for growth simulation setups with various proportions of inhibitory neurons and levels of inhibitory clustering.** *Green boxes* denote stabilisation of network structure and electrical activity. *Purple boxes* denote large unstable oscillations in network structure and unstable burst-like oscillations in electrical activity. *Blue boxes* denote stable oscillatory behaviour of neuritic radii and electrical activities. *Pink boxes* denote unbounded growth examples, where the system was unable to reach the desired level of electrical activity for all neurons, with all neuritic fields growing indefinitely. *White areas* did not have any suitable configurations to run. In panel **A**, the networks were initially disconnected. In panel **B**, the networks started as regular ring networks.

Network analysis of 1D global behaviour types

To gain a deeper understanding of how distinct global network behaviours are characterised in terms of network theoretical measures, we plotted neuritic radii and electrical

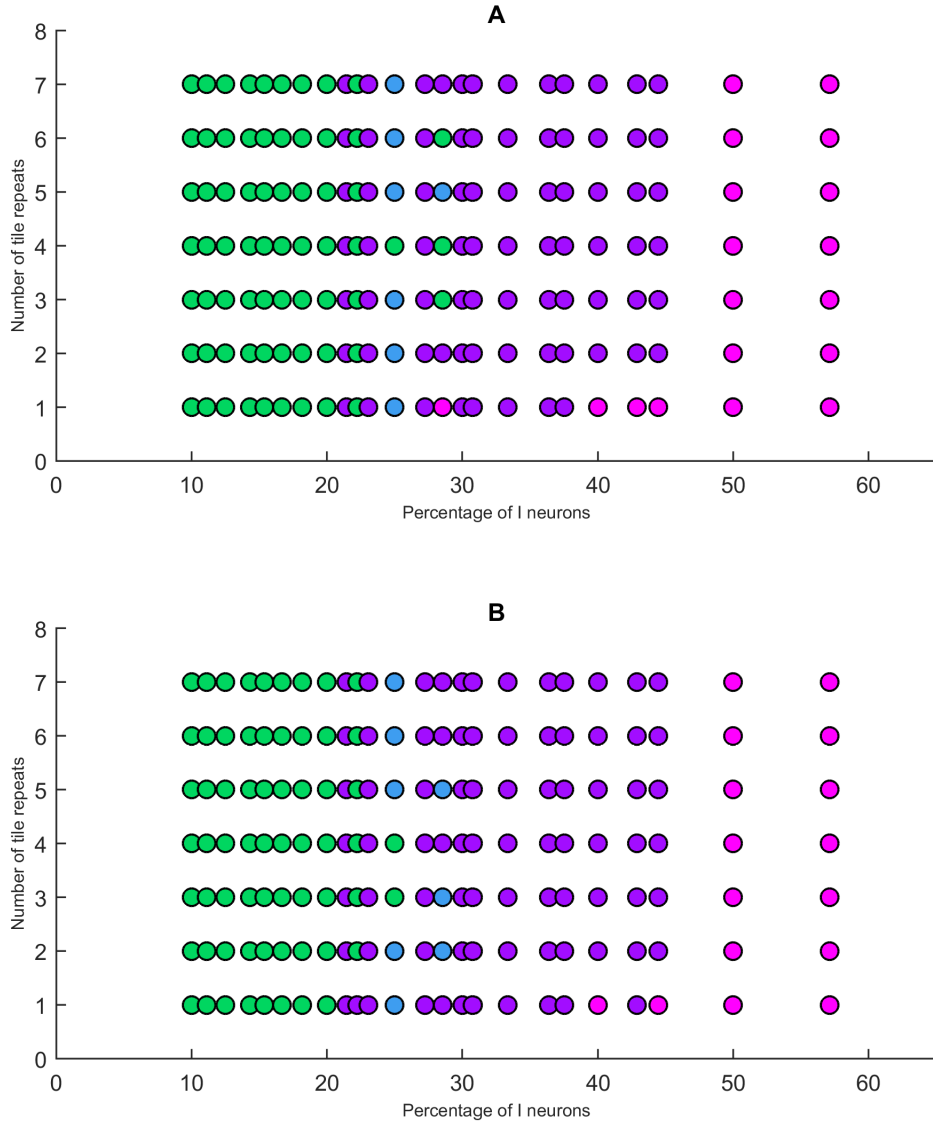


Figure 2.4: **1D system behaviours as a function of the percentage of inhibitory cells (*horizontal axis*) and number of tile repeats (*vertical axis*).** All tile arrangements are contiguous. Tiles are repeated in an adjacent manner to maintain a 1D system. *Green circles* denote networks experiencing complete stabilisation. *Blue circles* denote periodic (stable) oscillatory behaviour. *Purple circles* denote unstable oscillatory behaviour. *Pink circles* denote simulations where all neuritic fields grow unbounded because the desired level of electrical activity cannot be reached. In panel **A**, the networks were initially disconnected. In panel **B**, the networks started with sparse connectivity, with neuritic radii values randomly generated in the interval (0,0.6) (identical seed of value 10 for all networks). All other parameters were as listed in Table 2.1.

activity dynamics, alongside corresponding network structure visualisations and degree distributions, for three simulation configurations with distinct global behaviours (Figures 2.5 - 2.7). Using the subgraph counting algorithm described by Ritchie et al. [97], we

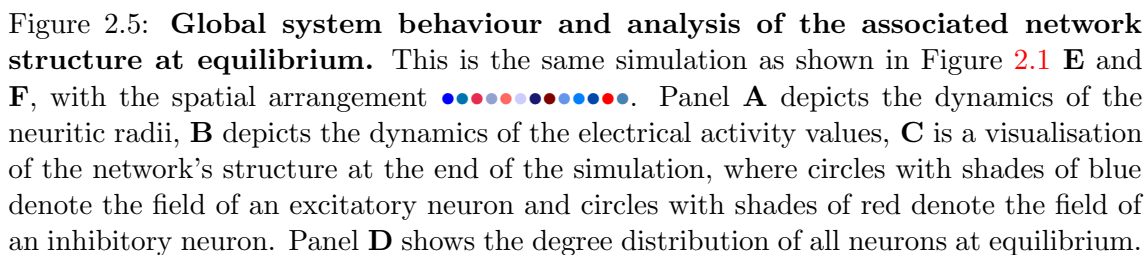
performed motif analysis on networks at specific time points from each simulation to determine if global behaviour types are also characterised by specific network motifs (Table 2.3). Here, we list the behaviour types observed and describe each in terms of structural and electrical dynamics, and we discuss other noteworthy characteristics.

Total stabilisation Networks which experience total stabilisation of their structure and electrical activity (Figure 2.5) undergo a period of rapid overshoot in the number of connections, until a critical level of network connectivity is reached (Figure 2.5 A). At this stage, a rapid pruning of connections occurs, with all neuritic radii shrinking at a similar rate. Simultaneously, we observe an overshoot followed by a steep reduction in the electrical activity for all neurons (Figure 2.5 B). Following periods of overshoot and pruning, the neuritic radius and electrical activity for all neurons tend quickly toward their equilibrium values. Once all values have stabilised, we look to a visual representation of the final network structure (Figure 2.5 C) and the corresponding degree distribution (Figure 2.5 D) to understand the structural elements in more detail. In areas containing inhibitory neurons, neighbouring excitatory neurons have large field sizes, and areas of high inhibitory clustering seem to coincide with even larger excitatory neighbours. The corresponding degree distribution suggests that the introduction of inhibitory neurons has resulted in a long-tailed degree distribution, with the presence of excitatory hub nodes with high degree that are able to contact the majority of the remaining neurons in the system. We note that the inhibitory clustering measure for the network structure ($\circ\circ\bullet\circ\bullet\circ\bullet\circ\circ\bullet\circ$), which experienced complete stabilisation of both network structure and electrical activity, is 0.04707. Looking at the resulting network in terms of network motifs present within the structure (Table 2.3), we observe that the majority of motifs at stabilisation contain open loops as opposed to closed loops.

Stable oscillations Networks developing stable oscillatory behaviour appear to experience relatively minor changes in their structure over time (Figure 2.6). The associated electrical activity dynamics for this scenario (Figure 2.1 B) show very similar behaviour to that of the neuritic radii values. After the initial period of overshoot and pruning of network connections, the stable oscillatory regime is reached, and both network structure and electrical activity experience stable oscillations of similar, small amplitudes. Once the system has reached the oscillatory regime, the network structure has a long-tailed degree distribution, indicating the existence of hub nodes. Looking at the dynamics of the two largest neuritic radii (both excitatory neurons neighbouring one or more inhibitory

neurons), we observe that their oscillations are almost out of phase with one another; it appears that it is the interaction between these two large neuritic fields which holds the system in a stable oscillatory regime. The inhibitory clustering measure for the network structure ($\circ \circ \circ \circ \circ \bullet \bullet \circ \circ \bullet \circ \bullet \circ$) is 0.2269. Furthermore, we note that the network structure during the low point in the oscillation of one neuritic radius (Figure 2.6) contains very similar motifs to the final network structure of the simulation which experienced complete stabilisation (Figure 2.5), but by the mid- and high points in the oscillations, the majority of motifs increase in number consistent with increased network connectivity (Table 2.3).

Unstable oscillations Networks experiencing sustained unstable oscillatory behaviour undergo far more extreme changes in their structure, level of connectivity, and electrical activity over time (Figure 2.7). From the start of the simulation, all neuritic radii endure unstable oscillations with large amplitudes, mostly in synchronisation with one another (i.e., all neuritic fields in the system are expanding or retracting simultaneously). During each increase in field sizes, we see bursting behaviour of the electrical activity values, followed immediately afterwards by a return to the resting electrical activity (equal to zero in the ES model). Coinciding with the peak of each oscillation in field size, we see a rapid increase in electrical activity for the majority of neurons. Following this, we observe unstable movements of the electrical activity values and the neuritic fields reduce in size, before the bursting behaviour commences once again. In terms of network attributes, during unstable burst-like oscillations it is clear that the network structure alternates between full and partial connectivity at various points during the oscillations. During the bursting behaviour of the electrical activity, the network structure is not fully connected, with a long-tailed degree distribution that implies the existence of excitatory hub nodes. Sometime after the bursting behaviour, the network structure becomes fully connected once again and the cycle of behaviour continues. The inhibitory clustering measure for the network structure ($\circ \circ \bullet \circ \circ \circ \circ \circ \bullet \bullet \bullet \circ \circ$) is 0.2914. Looking at motif analysis of the network structure at various time points (Table 2.3), it is immediately obvious that the changes in number and distribution of network motifs during the time course of this simulation are much more extreme when compared with other behaviour types we analysed in this section. At time 659,940, when the electrical activity values are exhibiting burst-like behaviour (Figure 2.7), the network contains a wide array of motifs, from triangles and squares to pentagons and even hexagons. However, once the network becomes fully connected (after the bursting behaviour and at the peak of network connectivity), we see that the network is entirely made up of fully connected squares (i.e., high clustering).



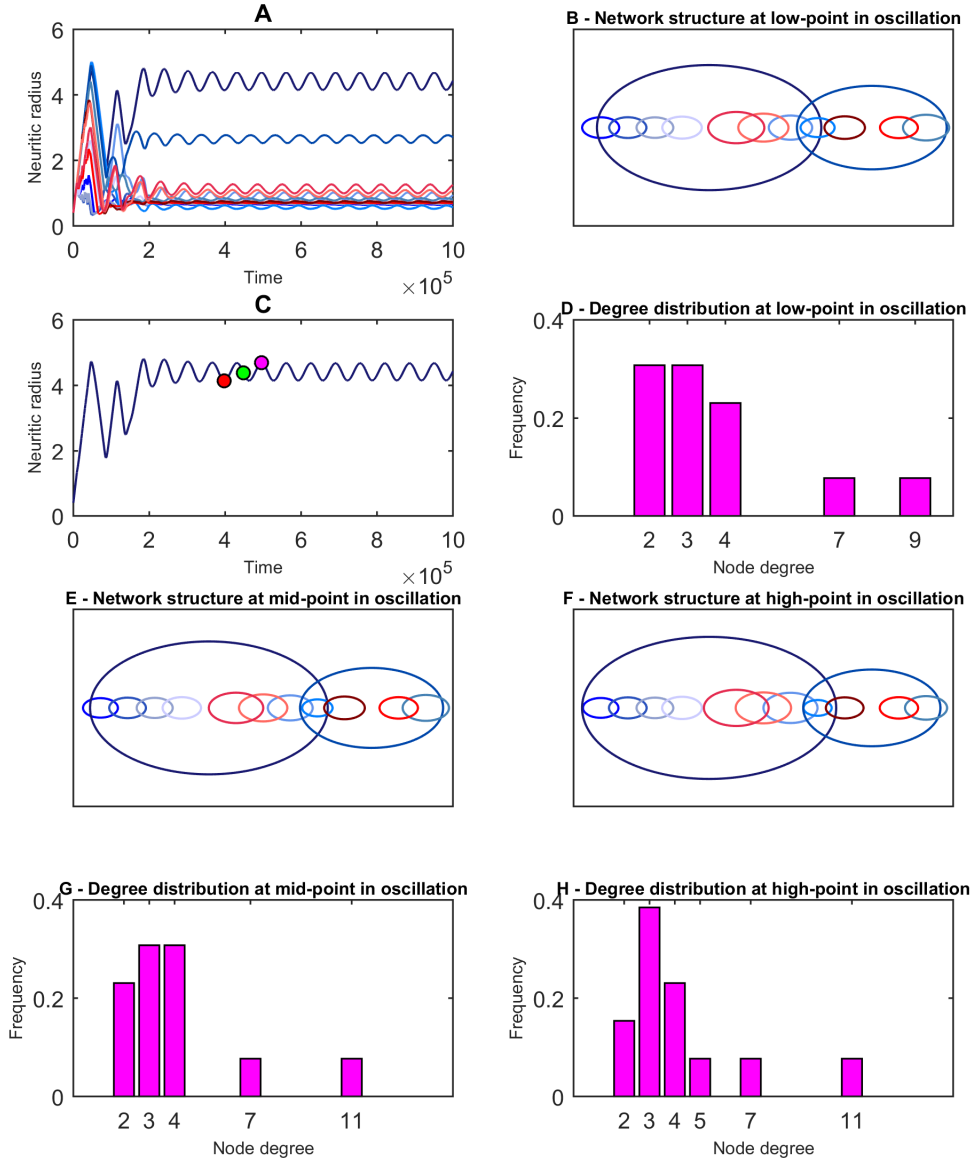


Figure 2.6: **Network structure and degree distribution of the simulation shown in Figure 2.1 A and B, at three time points during the periodic oscillations.** See coloured markers in panel C, where a *red circle* denotes a low point in an oscillation, a *green circle* denotes a midpoint in an oscillation, and a *pink circle* denotes a high point in an oscillation. The spatial arrangement of neurons is $\bullet \bullet$ with the network being initially disconnected. Panels B and D show the network structure and associated degree distribution at a low point in an oscillation, panels E and G show the network structure and associated degree distribution at a midpoint in an oscillation, and panels F and H show the network structure and associated degree distribution at a high point of an oscillation shown in panel C.

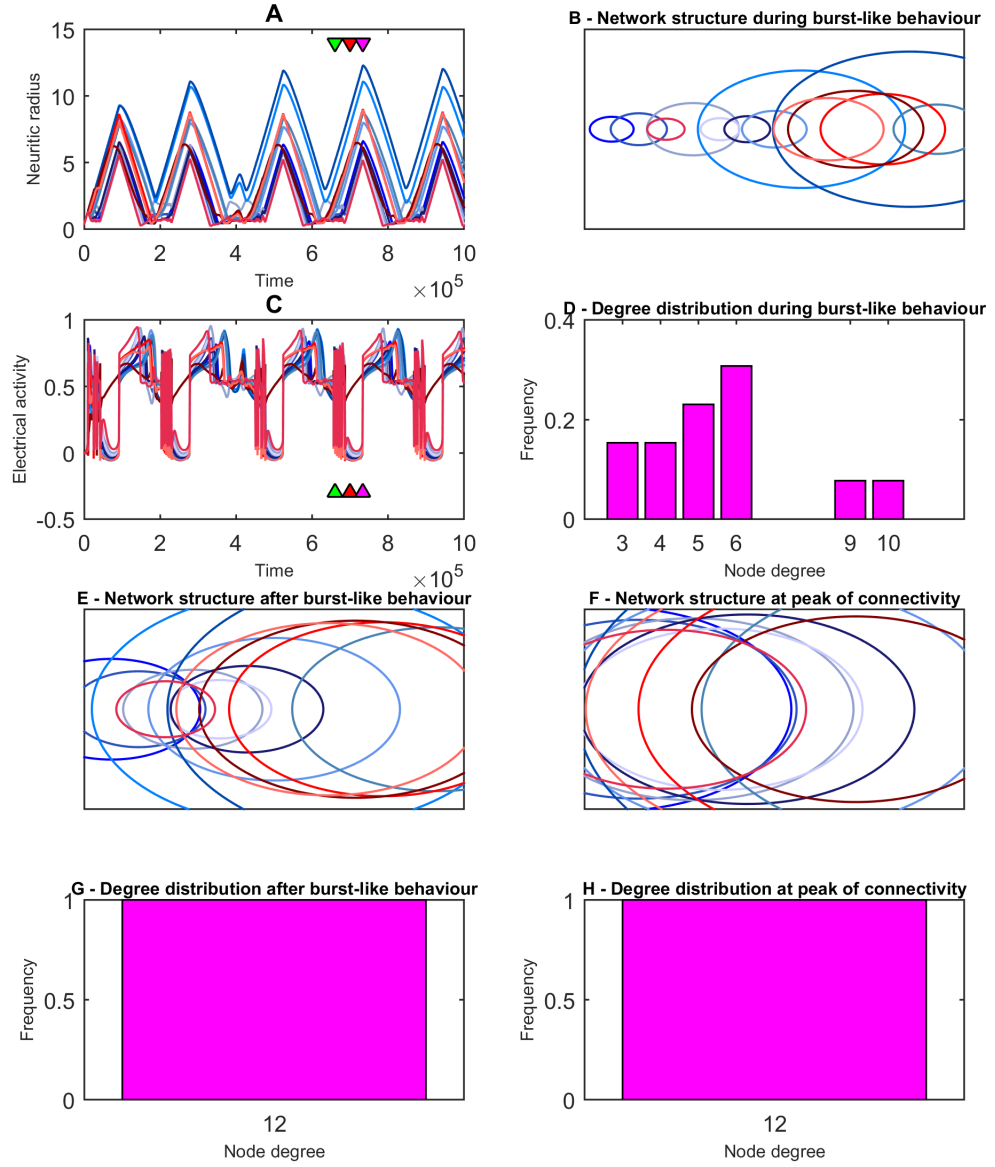
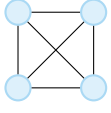
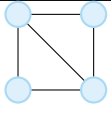
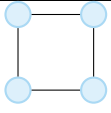
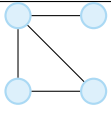
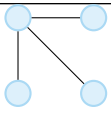
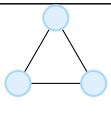
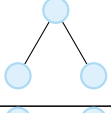
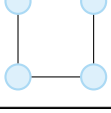


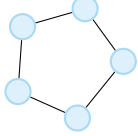
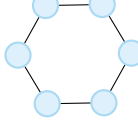
Figure 2.7: **Network structure and degree distribution of the simulation shown in Figure 2.1 C and D, at three time points during the unstable oscillations.** See coloured markers in panel C, where a *green triangle* denotes a time during burst-like behaviour of electrical activity, a *red triangle* denotes a time immediately after the burst-like behaviour, and a *pink triangle* denotes a time where the network is experiencing a peak of connectivity (corresponding triangles are also shown in panel A). The spatial arrangement of neurons is $\bullet \bullet \bullet \bullet \bullet \bullet \bullet \bullet \bullet \bullet \bullet \bullet$ with the network initially disconnected. Panels B and D show the network structure and associated degree distribution during the burst-like behaviour. Panels E and G depict the network structure and associated degree distribution after the burst-like behaviour and panels F and H show the network structure and associated degree distribution at the peak of connectivity.

Table 2.3: Network motif counts at various points of the simulations in Figures 2.5 - 2.7. Network motifs are displayed here in two dimensions for ease of visualisation, but all structures considered are 1D lattice structures with periodic boundaries.

Reference	Fig 2.5	Fig 2.6	Fig 2.6	Fig 2.6	Fig 2.7	Fig 2.7	Fig 2.7
Time	1,000,000	397,061	448,310	496,220	659,940	700,040	733,720
Motif	Motif count						
	1	1	3	4	17	715	715
	11	12	18	19	45	0	0
	0	0	0	0	2	0	0
	0	0	0	0	0	0	0
	23	39	75	69	21	0	0
	13	13	17	19	38	286	286
Triangles involved in complete squares	4	4	11	15	36	286	286
Triangles involved in diagonal squares	12	13	17	17	36	0	0
Triangles not involved in complete/diagonal squares	0	0	0	0	0	0	0
	48	52	64	64	75	0	0
	51	43	28	31	77	0	0

Continued on next page

Table 2.3 – continued from previous page

Reference	Fig 2.5	Fig 2.6	Fig 2.6	Fig 2.6	Fig 2.7	Fig 2.7	Fig 2.7
Time	1,000,000	397,061	448,310	496,220	659,940	700,040	733,720
Motif	Motif count						
	0	0	0	0	1	0	0
	0	0	0	0	1	0	0

2.5.2 2D results

The effect of inhibitory clustering on global system behaviour in 2D

Growth simulations of various neuron arrangements on 2D lattice structures were implemented, and in all cases we observed either complete stabilisation of network structure and electrical activity, or stable oscillations in network structure and electrical activity. Complete stabilisation and stable, periodic oscillations both occurred after the typical initial overshoot and pruning periods (Figure 2.8). No 2D growth simulations were observed to exhibit burst-like behaviour of electrical activity and large unstable oscillations in network structure, as seen previously in 1D growth simulations, e.g., Figure 2.2 A and B. Although oscillatory 2D arrangements tended to have larger 2D clustering values, it was still possible to detect deviations from this general rule, e.g., see arrangements 51 and 52 in Table 2.4. Examples such as this suggest that the 2D inhibitory clustering measure (2.9) is overly sensitive to how inhibitory neurons are organised *within* the covering rectangle. Instead, when considering only the component of the 2D inhibitory clustering measure which characterises the smallest area within which all inhibitory neurons are found, i.e., WH/M , and testing various arrangements of $L = 36$ neurons, with $M = 6, 7, 8, 9, 10, 11$ inhibitory neurons (and therefore varying levels of inhibition between 16.67% and 30.56%), we find a robust relationship whereby neuron arrangements with smaller WH/M values are more likely to experience oscillatory behaviour (Figure 2.9). Our results also show that, for a given WH/M value, networks with larger M , and hence a higher proportion of inhibitory neurons, are more likely to experience oscillatory behaviour. Intuitively the observed relationship between WH/M and the presence of oscillatory behaviour is logi-

cal, since the smallest possible value $WH/M = 1$ signifies that the covering rectangle is of equal size to the total number of M inhibitory neurons and contains no excitatory neurons, meaning that the inhibitory neurons are maximally clustered, e.g., arrangement 47 in Table 2.4. However, even with a fixed number of inhibitory neurons, maximal clustering can be achieved in multiple ways and can exhibit distinct outcomes. For example, for $M = 6$, maximal clustering can be achieved using a single row of six neurons or two rows of three neurons. When these arrangements were compared in growth simulations of a $2D$ network of 36 neurons with all else held constant, the single line of six inhibitory neurons induced complete stabilisation, whereas the network containing a single inhibitory cluster of two lines of three neurons experienced stable oscillations in both network structure and electrical activity.

Table 2.4: Global system behaviour and clustering measure for mixed $2D$ simulations with various spatial arrangements. Default values were used on initially disconnected networks.

ID	Spatial arrangement	L	M	Behaviour	$2D$ clustering
47		36	6	Stable oscillatory	1
48		36	6	Stabilisation	0.8965
49		36	6	Stabilisation, transient oscillations	0.7222

Continued on next page

Table 2.4 – continued from previous page

ID	Spatial arrangement	L	M	Behaviour	2D clustering
50		36	6	Stabilisation	0.6667
51		36	6	Stable oscillatory	0.8056
52		36	6	Stabilisation	0.9794

2.6 Discussion

The main findings of our simulations relate to system stability and the effect of spatial clustering of inhibitory neurons. We demonstrate that subtle alterations in 1D and 2D arrangements of excitatory and inhibitory neurons can have marked effects on global behaviour of electrical activity and network connectivity in the spatially embedded ES model. In particular, we find that lattice networks containing highly clustered inhibitory neurons are more likely to display oscillatory dynamics of both electrical activity and network structure than those where excitatory and inhibitory neurons are more evenly distributed across all lattice positions.

Instability is mostly evident in 1D networks, where burst-like behaviour of electrical activity and large unstable oscillations in network structure can be observed. Results of

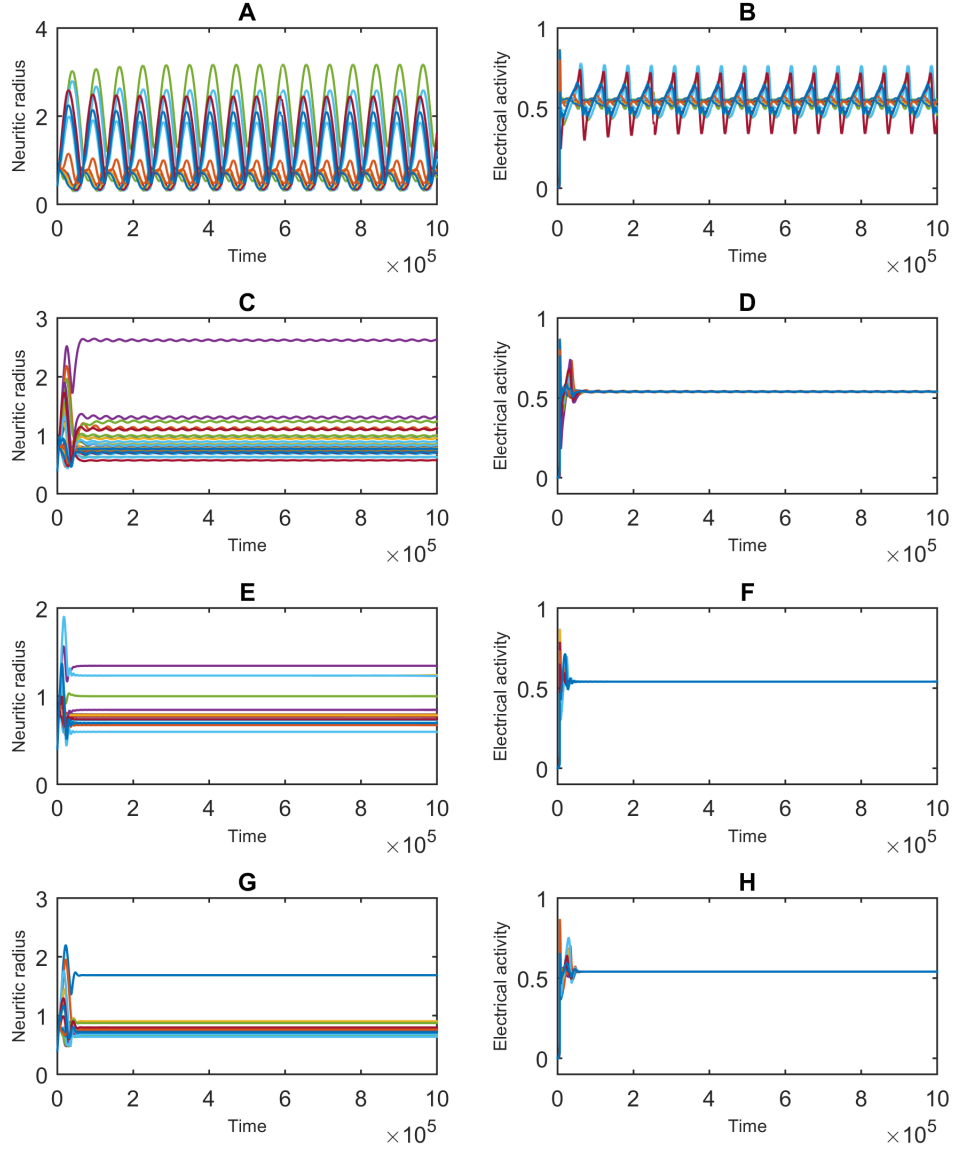


Figure 2.8: **Global system behaviour of mixed 2D lattice networks with various levels of inhibitory clustering.** In all cases $L = 36$, $N = 30$, $M = 6$ and default parameters listed in Table 2.1 are used. The networks are initially wholly disconnected and neurons are at rest. Figures on the *left-hand side* depict the dynamics of the individual neuritic radii values; figures on the *right-hand side* depict the dynamics of the individual electrical activity values. Panels **A** and **B** depict the dynamics of arrangement 47 in Table 2.4, panels **C** and **D** depict the dynamics of arrangement 51 in Table 2.4, panels **E** and **F** depict the dynamics of arrangement 49 in Table 2.4 and panels **G** and **H** depict the dynamics of arrangement 50 in Table 2.4.

2D network simulations tend to be more stable; no burst-like behaviours are observed in 2D, suggesting that networks in higher spatial dimensions either mask or protect against the emergence of the most pathological network behaviours. It is important to note that

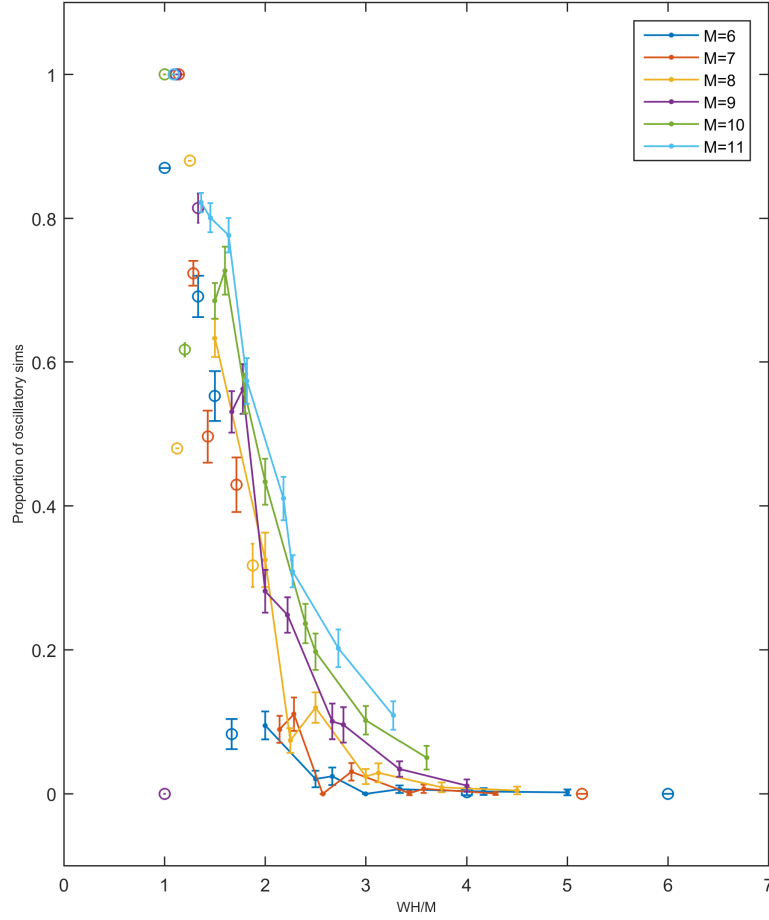


Figure 2.9: **The proportion of 2D neural network growth simulations depicting oscillatory behaviour of electrical activity and network connectivity for a range of WH/M values, where the terms W , H and M are defined in Equation (2.9).** Growth simulations consisted of networks of $L = 36$ neurons with $M = 6, 7, 8, 9, 10, 11$ inhibitory neurons, and default parameters listed in Table 2.1 were used. Networks were initially wholly disconnected and neurons were at rest. For each M , 2 million neuron arrangements were generated at random, from which the unique set of WH values was extracted. For each (M, WH) pair, 200 neuron arrangements were selected at random. Growth simulations of all 200 arrangements were implemented and the result tested for behaviour through thresholding of the norm of the variance of the last 10 data points, where the norm was taken over all L neurons. Thresholds were empirically determined and confirmed visually. The procedure of picking 200 arrangements for each (M, WH) pair was repeated 50 times to obtain the mean and standard deviation, displayed in the plot using error bars. Empty circles denote (M, WH) pairs for which less than 200 arrangements were available for testing.

although we describe periodic oscillations as being stable, this type of behaviour does not necessarily imply a healthy network outcome.

No attempt has been made here to simulate the extraordinarily complex 3D structure

of the developing and mature mammalian cerebral cortex using the spatially embedded ES model. Such results may lead to further dilution of the spatial effects given that higher dimensions lead to greater overall connectivity. This may in turn move the system closer to a well-mixed population where mean field models with fewer equations can provide accurate approximations. Nevertheless, there are interesting parallels between the ES model and the neurodevelopmental literature which will be discussed later. If it is a general rule that increased spatial dimension leads to greater tolerance of inhibitory clustering effects on network stability, then it is possible that $3D$ network activity-dependent network growth will be even more robust than $2D$ network growth.

Oscillatory behaviour in network structure, especially an unstable one, has been considered, for the most part, to be an undesired outcome as it renders the network fragile and therefore more vulnerable to the development of a pathological dynamical outcome. Modelling work by Ehrens et al., e.g., suggested that seizures can manifest through small perturbations in the synaptic connections that render the entire cortical network unstable [24]. An alternative view is that instability of network structure that increases networks' sensitivity to random perturbations might allow a network to depart from an undesirable state, thus providing a means for resilience and adaptation. It is difficult to explore such a possibility with the present model due to the lack of separation between network structure and electrical activity. Whilst the authors of the original model were able to observe distinct oscillations in electrical activity and network structure, the simulations reported in this chapter, in order to pursue a particular research question, used a narrower set of parameters in which there was no separation of timescales.

2.6.1 Comparison to previous modelling results

Previous studies of the ES model have postulated that outgrowth and interactions between excitation and inhibition can lead to complex patterns of development in individual cells [119]. Excitation increases activity but inhibits outgrowth, whereas inhibition does the opposite [119]. When dealing with a purely excitatory model, with individual neurons assigned various outgrowth rates (the parameter ρ in the ES model), complex periodic behaviour of connectivity and electrical activity can be observed, with Van Ooyen and Van Pelt concluding that the precise network behaviour depends on the spatial distribution of the cells and the distribution of the outgrowth properties over the cells [118]. A later study with a simple two-neuron $E - I$ model showed that the introduction of inhibition could account for network bistability [120]. It concluded that purely excitatory networks result

in the same final attractor regardless of initial conditions, whereas mixed (excitatory and inhibitory) networks do not necessarily do so, i.e., they can be bistable. Further this study shed light on the excitation-inhibition balance, demonstrating that networks developing under conditions of relatively high inhibition result in a “pathological” state with oscillatory activity whereas a low level of inhibition during the initial stage of development enables the system to develop toward the “normal” stable end state [120].

Our work reinforces the idea that networks with higher levels of inhibition are more likely to experience oscillatory dynamics of and on the network. However, through revealing distinct global behaviours for different spatial arrangements with a fixed number of excitatory and inhibitory neurons, we have established that the global behavioural dynamics and structural characteristics of the network rely not only on the balance between excitation and inhibition but also on the spatial arrangement of neurons within the network (and, to a limited extent, the initial conditions). In particular, we have offered that spatial clustering of inhibitory neurons, which we have characterised through measures of inhibitory clustering in $1D$ and $2D$, is an important determinant of the network dynamics. Networks with higher levels of inhibitory clustering are more likely to undergo oscillatory dynamics in electrical activity and network structure than networks with low levels of inhibitory clustering.

There is little published literature available on the effects of increased inhibitory clustering on neuronal network structure and dynamics. In studies of the ES model, inhibitory neurons are found to (1) impose a structure on neighbouring excitatory neurons, helping them to connect to different parts of a structure by inducing outgrowth and (2) increase the overall degree of connectivity in a network [119]. Van Ooyen et al. proposed that the number and distribution of inhibitory neurons is important: when inhibitory neurons are able to contact one another (i.e., our clustering measures (2.8) and (2.9) become larger), the neurons are electrically inhibited (self-inhibition), but their outgrowth will become stimulated [119]. This causes the ultimate level of inhibition in such a system to be higher than in a network without self-inhibition. It has also been noted that long-range inhibition is obtained when inhibitory cells occur in a clustered fashion and are able to stimulate one another’s outgrowth [119]. More recently, Litwin-Kumar and Doiron investigated the implications of excitatory clustering on cortical activity, finding that even modest clustering substantially changed the behaviour of the network activity, introducing slow dynamics during which clusters of neurons experience temporary changes in their firing rate [63]. In a network structure consisting of solely excitatory and inhibitory neurons, excitatory

clustering and inhibitory clustering will be somewhat congruous concepts, and, in this respect, our results support and complement those of Litwin-Kumar and Doiron [63].

To test the hypothesis that network structures with high levels of inhibitory clustering are more likely to undergo oscillatory behaviour, we proposed measures of inhibitory clustering within $1D$ tile networks and $2D$ lattice networks in which neurons are assigned to lattice positions and networks are taken to have continuous boundary conditions. The fundamental idea that spatial arrangements affect dynamical behaviour was highlighted in the original work but not systematically investigated [119].

2.6.2 $1D$ network behaviours

Performing growth simulations of $1D$ network arrangements, and in particular using the notion of tiles, means that an exhaustive investigation of $1D$ network arrangements was possible. As it stands, our $1D$ measure (2.8) captures the extent of inhibitory clustering within a tile network and provides ease of comparison across tile network structures of different sizes. Even within $1D$ networks, there is scope for improvement, however. Whilst the measure takes into account the closeness of $(M - 1)$ inhibitory pairs with M inhibitory neurons, it does not measure the *order* of these pairs. Using the current measure, it is therefore possible to find distinct spatial arrangements which produce an identical clustering measure but experience different global behaviours. For example, arrangements 21 and 22 in Table 2.2 have the same clustering measure, but one network experiences complete stabilisation whilst the other undergoes stable oscillations.

The $1D$ inhibitory clustering measure (2.8) allowed us to map out the relationship between inhibitory clustering and proportion of inhibition in a $1D$ system, along with the associated dynamics of and on the circular tile networks. Irrespective of whether the networks were initially connected or disconnected, we observed a clear structure (see Figure 2.3 A and B, respectively). However, it is important to note that the different regimes are extremely coarse grained: for each segment plotted, we ran one individual simulation, where the proportion of neurons was contained within an interval of width 10% and the clustering measure was contained within an interval of length 0.05. In order to obtain sufficient coverage of all segments, we considered various network sizes, a range of values for M and N , and various spatial arrangements. We therefore expected to observe increased variability on the boundaries of areas delimiting different regimes, and we treated the regimes produced with caution, focusing more on the qualitative results than on specific behaviours.

A similar structure is observed again when plotting the proportion of inhibitory neurons in a contiguous tile versus the number of adjacent tile repeats combined to form the entire $1D$ network (Figure 2.4). The idea of having adjacent tile repeats is a similar concept to that explored in a modelling study by Malagarriga et al. in which mixed cortical macrocolumns, operating in a partially synchronised irregular regime, are seen to affect the dynamics of the network itself [69]. The authors found that in this type of mesoscopic network, excitation and inhibition spontaneously segregate, with some columns acting mainly in an excitatory manner while some others had predominantly an inhibitory effect on their neighbours. They also reported that hub nodes (i.e., nodes with high degree) are preferentially inhibitory, contrasting with our finding that increased inhibitory clustering induces excitatory neurons of high degree. Whilst we do not suggest that excitatory hubs are physiologically likely, it is worth mentioning that in our networks, hubs are an emergent property; whereas, in the above study, hubs are the result of imposing a scale-free network structure on the model. Furthermore, in agreement with Malagarriga et al. [69], when we analysed the characteristics of neuronal networks exhibiting distinct global behaviours, we observed some emerging segregation of excitation and inhibition, suggesting that clustered inhibitory neurons induce a secondary network “layer” of high degree excitatory neurons which could be responsible for the transport of information across the whole network. We acknowledge that the $1D$ networks studied here are biologically unrealistic due to their size and therefore there are limited conclusions to be drawn regarding the presence of network motifs and degree distributions. Nevertheless, our results speak to recent results from mathematical work by Ritchie et al. showing that in networks with identical degree distribution and clustering coefficient, differences in higher order structure (as assessed by varied subgraph counts) can have marked effects on the dynamics running on the networks [97]. Network analysis on simulations with larger networks consisting of $2D$ and $3D$ lattices with periodic boundary conditions would provide more insight into the emergence of specific network motifs and their function.

2.6.3 $2D$ network behaviours

Increasing dimensionality leads to increasing complexity, such that an exhaustive list of $2D$ neural network growth simulations has not been attempted here. Further, designing the $2D$ inhibitory clustering measure (2.9) using a similar approach to the $1D$ measure (2.8) led to a loss of sensitivity and a not-always-monotonic relationship between the measure (2.9) and the probability of oscillatory dynamics being observed; see, e.g., arrangements 48

and 51 in Table 2.4. In fact, using simpler components of the $2D$ clustering measure (2.9) to compute WH/M revealed a far clearer relationship between the arrangement of neurons and the global behaviour of the network and its electrical activity (Figure 2.9), where in general, configurations with smaller values WH/M were more likely to be oscillatory. In contrast to this relationship, we found some $2D$ arrangements contained such large clusters of inhibitory neurons, that the effects of this clustered inhibition appeared to be eliminated, and the system experienced complete stabilisation (see, e.g., Figure 2.9, $M = 9$, $WH/M = 1$, where 9 inhibitory neurons were arranged into a 3×3 grid of neurons and hence were maximally clustered, but the system experienced complete stabilisation of network structure and electrical activity – note that the inhibitory neuron in the centre of such an arrangement is completely surrounded by inhibitory neurons). This finding suggests that self-inhibition can have nontrivial effects and more work is needed to refine methods for measuring spatial clustering of neurons and to understand how local structure of neurons within the covering rectangle will determine global outcome.

Various approaches can be considered either to improve the sensitivity of the $2D$ clustering measure (2.9) or to propose novel methods for quantifying clustering of neuron locations in mixed neuronal arrangements. If one considers inhibitory neurons as clusters in a “sea of excitatory neurons, the average cluster size of the cluster size distribution coupled with intercluster distances may provide an improved picture of how the spatial arrangement of neurons influences the outcome at system and network level. Furthermore, topological or geometric measures such as the perimeter of inhibitory clusters may add insights.

2.6.4 Future modelling studies

The ES model uses circular neuritic fields to model the area of influence of a single neuron. One consequence of this is that all neurons connect to their direct neighbours before connecting to neurons located further away topologically. As a result, the networks cannot develop the small-world properties observed in neuronal networks. Furthermore, restricting the state space of neuron locations to equally spaced lattice positions within a given area is not biologically realistic and greatly reduces the possible arrangements of neurons.

Analytical work on the spatially embedded ES model (especially in more than $1D$) is not possible without engaging in coarse-grain modelling that would inevitably involve removing the very characteristic that we seek to study, namely, spatial embedding. Indeed, this has been the case for all analytical works carried out on this type of model to date, e.g.,

Van Ooyen and Van Pelt [118]. However, as pointed out by Wolf et al. [127], “whenever the essential ingredients of a phenomenon need to be identified or when a qualitatively novel type of behaviour demands conceptual advancement, idealisation – even counterfactual idealisation, that is the neglect of known features – is required.

Future modelling studies should investigate the effects of inhibitory clustering using an activity-dependent growth model where neurons are assigned to random locations within some state space, have a variable and discrete number of synaptic elements, and various synapse formation rules can be implemented (e.g., random, distance-dependent, or otherwise), in order to create specific network attributes. Such a modelling approach was shown to conserve small-world network properties in a study investigating cortical reorganisation after focal retinal lesions [13].

2.6.5 Future experimental studies

Until recently it was not appreciated that within the developing mesencephalon, there exist inhibitory interneurons whose lineage results in their being spatially clustered rather than randomly distributed [8, 15]. It is not known how such an arrangement could impact on in vivo activity-dependent network development, but models such as the one explored in this chapter point to clustering as having a crucial role in network structure and function. Our results especially in $2D$ suggest that some degree of inhibitory clustering can be tolerated by the network. Thus in vivo it may be that network stability is maintained whilst allowing for the benefits of inhibitory clustering.

Networks in which there is inhibition of inhibition exist in vivo. The physiological effect of such connectivity is to increase network excitation. The fact that such networks can be detected in the mature nervous system again indicates that during development a certain level of inhibitory to inhibitory connectivity is tolerated. In vivo such arrangements are being actively studied but their functional implications remain poorly understood [93]. Interestingly, inhibitory to inhibitory interactions are seen only in certain inhibitory neuron subtypes of the extremely diverse inhibitory interneuron network [68, 92]. Functionally such arrangements within the sensory system have been shown to increase salience of signal detection [93, 50]. How such networks emerge during in vivo development and how inhibition of inhibition affects network activity-dependent growth remains to be explored.

Inhibitory neurons in the mature nervous system show greatest synaptic plasticity [123]. In relation to the ES model, it is interesting to note that in vivo the on-going shaping of network structure is crucially dependent on neural inhibition. In the mature nervous

system, inhibitory synapses are more dynamic in response to the sensory environment than excitatory synapses [123]. Furthermore, suppression of inhibition leads to more exuberant yet less focused connectivity, and therefore in sensory systems a less functional connectivity [21, 123, 28]. Future models may explore how through inhibitory mechanisms, dynamic network stability is achieved, i.e., a network that can rapidly remodel to reflect changes in environmental experience yet one in which the essential structure and dynamics are preserved.

Excessive inhibition and disruption of inhibition leads to network pathology. As discussed, the results of our modelling study indicate that a certain level of inhibitory clustering can be tolerated and result in a stable network. However, even small changes in the arrangement or proximity between inhibitory neurons can lead to instability. In vivo we suggest that early clustering of inhibitory neurons that inhibit one another during the activity-dependent stage of neural development will lead to excessive connectivity and network instability. Whilst it is unknown how inhibitory clustering might play out in vivo studies of neural migration disorders, there are strong hints that such a mechanism or a similar mechanism may be of importance [66]. We suggest that there should be particular emphasis placed on the detection in vivo of inhibitory neuron clusters and an exploration of their potential role in network pathology. Finally, in an era where clinical neuroscience is exploring neural plasticity therapy as a way of overcoming the effects of brain injury, a focus on neural inhibition as a potential target for inducing favourable network remodelling [31] will be informed by dynamic neural network growth models in which both the quantity and the spatial arrangement of inhibition are important variables.

2.6.6 Concluding remarks

Simulations involving the ES model suggest that the complex dynamical behaviour neuronal networks experience is influenced by a combination of factors, including the balance between excitation and inhibition, the spatial topology of those excitatory and inhibitory neurons, and the connections between them. There are too many intrinsic limitations to the ES model to be allowed to make strong statements about cortical development. Nevertheless, this work suggests that modelling studies should be careful to attribute particular dynamic properties to the E/I ratio as such properties may be meaningful in well-mixed populations but insufficiently descriptive in the kind of structured networks found in physiological systems. This certainly highlights the need for further work in developing tractable mathematical models on structured networks, where balancing the

need for analytical tractability versus model realism is key in order to identify clear dependencies between model ingredients and outcomes.

2.7 Acknowledgements

Rosanna Barnard acknowledges funding for her PhD studies from EPSRC (Engineering and Physical Sciences Research Council) EP/M506667/1. Simon Farmer acknowledges funding support from the UCLH Biomedical Research Centre.

Chapter 3

Edge-based compartmental modelling of an SIR epidemic on a dual-layer static-dynamic multiplex network with tunable clustering

3.1 Introduction

The continual design and development of mathematical models describing epidemic processes on large, complex populations improves our understanding of how diseases and individuals behave during an epidemic, and how preventative measures can be implemented for the greater good. With ever-increasing computational power, models can incorporate increasingly complex features, and model predictions may become more valuable. Nonetheless, any model must tread a careful balance between capturing observed real-world complexity and enabling calculations and conclusions to be drawn with ease. The ultimate epidemiological model must therefore incorporate the behavioural and structural features which significantly influence disease dynamics, whilst being analytically tractable.

Social heterogeneity describes the propensity for a social group to be diverse in character or content, and is an important determinant when studying the dynamics and control of infectious diseases [3]. In a social group, heterogeneity encompasses many descriptive elements, such as variations in individuals' behaviour or in susceptibility across group

members. In network theory, social heterogeneity can also describe variations in the *types* of connections an individual makes. For example, an individual can be connected to other individuals in distinct groups, such as workplace or community groups.

Structured populations with multiple connection types are well described by multiplex networks, where a population of individuals partakes in multiple network *layers*. Each network layer describes a specific type of interaction between members of the population, and network structure in one layer is allowed overlap with network structure in another layer. A pair of individuals in a multiplex network can share more than one connection. In a multiplex network, an individual is present in every network layer, but may or may not partake in connections in individual network layers.

Existing multiplex modelling studies have shown that single-layer approximations or aggregations of multiplex networks are not accurate enough to describe the epidemic process [19, 131, 33, 17], and further that an epidemic can spread on a multiplex network even if the individual layers are well below their respective epidemic thresholds [130]. A global cascades model generalised for multiplex networks was used to show that multiplexes are more vulnerable to global cascades than single layer networks [9]. These studies highlight the importance of accounting for heterogeneity in connection type by considering multiplex network models.

Another determinant of infectious disease dynamics is heterogeneity in the structural connections between individuals, within a single type of connection. Real-world networks often exhibit community structure, with a high density of connections within communities and a low density of connections between communities. They are also considered to exhibit other structural characteristics such as network transitivity or clustering, described in social network theory as the propensity for an individual to be connected to a friend of a friend [84].

Community structure has been shown to affect disease dynamics on single-layered (uniplex) networks, where on average, epidemics occurring on networks with community structure exhibit greater variance in final epidemic size, a greater number of small, local outbreaks that do not develop into epidemics, and higher variance in the duration of the epidemic [99]. Network quality functions able to detect community structure in multiplex networks have been developed [80]. Further, results such as the large graph limit of an SIR epidemic process on a dynamic multilayer network, where one network layer represents community links and another represents connections in healthcare settings, have been derived [47].

In network models, increased clustering is generally considered to slow an epidemic by increasing the epidemic threshold [71]. However, this relationship is not always monotonic. Higher clustering in a multiplex study of information propagation led to an increase in the epidemic threshold and a decrease in final epidemic size [132]. Increased clustering in a study of Watt’s threshold model generalised for a multiplex network comprised of clustered network layers led to a decrease in the probability of a global cascade and its size [131]. However, the authors also discovered a critical threshold for the average degree, above which clustering was shown to *facilitate* global cascades [131]. A uniplex network study found that simultaneously increasing clustering and the variance of the degree distribution led to an increase in final epidemic size [125]. Moreover, clustering can lead to correlations where high-degree individuals are more likely to connect with other high-degree individuals. It is clear that the effect of clustering is complex and should be considered in the design of network models.

In epidemiology it is also important to consider heterogeneity across contact *duration*. In human populations, links between individuals may be long-lasting (persistent), e.g. between an infant child and their caregiver; temporary (transient), e.g. between workplace colleagues; or more short-lived (fleeting), e.g. between strangers coming into close proximity on public transport. In a study using a year’s mobile phone data as a proxy for the structure and dynamics of a large social network, researchers found that persistent links tend to be reciprocal and are more common for individuals with low degree and high clustering [43]. Many network-based studies in the past have considered fully static network structures, and hence solely investigate the effects of persistent connections between individuals, see [53] for a review of differing approaches.

Later studies of epidemic processes on networks have incorporated persistent *and* transient connections into their models by imposing rewiring rules on static networks. Rewiring rules considered include spatially-constrained rewiring [95], random link activation and deletion [111, 102, 56], and temporary link deactivation [113, 105]. On the other hand, epidemic processes with fleeting contact duration can be well-described via the mass action model, which assumes all pairs of individuals contact one another at the same rate, the mean-field social heterogeneity model (also known as the degree-based mean-field model), which generalises the mass action model by allowing for variations in contact rate across the population, and the dynamic fixed- and dynamic variable-degree models, where edges are swapped at a given rate, or edges are broken and created at given rates, respectively [78, 77].

Here, we suppose that static and dynamic connections *coexist* in any complex population. We aim to derive a network model describing an SIR epidemic process spreading through a population where each individual has two types of connections: persistent links to individuals in their household, constituting a static network layer with community structure, and transient connections to strangers in the wider population, where all such edges rewire at a constant rate, constituting a dynamic network layer with conserved degrees.

In what follows, we utilise the edge-based compartmental modelling (EBCM) approach [124, 73, 74, 77], deriving equations which describe the time evolution of classical quantities of interest, where the underlying dual-layered static-dynamic network has heterogeneity in contact-type, contact-duration, and contact-structure. We derive the associated basic reproduction number R_0 , following the next generation matrix approach [20]. We describe the implementation of the EBCM model and of statistically-correct Gillespie simulations of the epidemic process [32]. The new model is validated, firstly by showing that collapsing either the static or dynamic network layers leads model equations to converge to existing equivalent model equations, and secondly by comparing the dynamics predicted by model equations to those from exact simulations. We explore how various combinations of model parameters and network layers influence global dynamics, uncover behavioural regimes that the model can achieve for specific combinations of infection and rewiring rates, and show that our derived R_0 behaves as expected. The chapter concludes with a discussion of potential implications of the work as well as possible extensions.

3.2 Methods

Our solutions are based on the class of undirected random graphs (networks). Each node is a member of a random number of static lines (2-vertex cliques), static triangles (3-vertex cliques) and dynamic lines (2-vertex cliques). The probability that a node has s static line stubs, t static triangle *corners* and d dynamic line stubs is described by the probability mass function $p_{s,t,d}$. The model captures network structure using the probability generating function (PGF)

$$g(x, y, z) = \sum_{s,t,d} p_{s,t,d} x^s y^t z^d. \quad (3.1)$$

When differentiating the PGF (3.1), we use superscripts such that $g^{(x)}$ denotes the first (partial) derivative of g with respect to x and $g^{(y,y)}$ denotes the second (partial) derivative of g with respect to y . Equation (3.1) can be used to calculate useful properties of the

multiplex network. For example, M_s , the expected number of static line stubs that belong to a randomly selected individual, M_t , the expected number of static triangle corners that belong to a randomly selected individual, and M_d , the expected number of dynamic line stubs that belong to a randomly selected individual, are calculated as follows:

$$\begin{aligned} M_s &= \sum_{s,t,d} s p_{s,t,d} = g^{(x)}(1, 1, 1), \\ M_t &= \sum_{s,t,d} t p_{s,t,d} = g^{(y)}(1, 1, 1), \\ M_d &= \sum_{s,t,d} d p_{s,t,d} = g^{(z)}(1, 1, 1). \end{aligned}$$

We consider a basic SIR compartmental model. Infections occur across edges on the static network layer at a constant rate β_s whilst infections occur across edges on the dynamic network layer at a constant rate β_d . Infected individuals recover at a constant rate γ . Once recovered, a node cannot be reinfected, and can no longer transmit infection to its neighbours. A comprehensive list of model variables and parameters is given in Table 3.1.

Table 3.1: Definitions for model variables and parameters. Many definitions refer to the test node u , which is selected at random from the population and modified so that it cannot transmit infection, but can itself become infected.

Variable/Parameter	Definition
β_s	Per-edge disease transmission rate on static network layer
β_d	Per-edge disease transmission rate on dynamic network layer
γ	Per-individual disease recovery rate
ρ	The proportion of initially infectious individuals
η	Edge rewiring rate on dynamic network layer
$S(t), I(t), R(t)$	The susceptible, infectious and recovered proportion of the population at time $t \geq 0$
$p_{s,t,d}$	The proportion of individuals in the network that are a member of s static line stubs, t triangle corners and d dynamic line stubs
$g(x, y, z)$	Probability generating function for the numbers of static lines, triangles and dynamic lines of which an individual is a member
Continued on next page	

Table 3.1 – continued from previous page

Variable/parameter	Definition
$\theta_2(t)$	A survivor function for remaining susceptible for some time $t \geq 0$, given that the individual in question is a member of a single static line
$\theta_3(t)$	A survivor function for remaining susceptible for some time $t \geq 0$, given that the individual in question is a member of a single triangle corner
$\theta_4(t)$	A survivor function for remaining susceptible for some time $t \geq 0$, given that the individual in question is a member of a single dynamic line
$\phi_S(t), \phi_I(t), \phi_R(t)$	The probabilities that a neighbour of u along a static line is susceptible, infectious or recovered, and has not transmitted infection to u by time $t \geq 0$
$\phi_{XY}(t)$	The probability that two neighbours of u in a triangle are in states X and $Y \in \{S, I, R\}$ and have not transmitted infection to u by time $t \geq 0$
$A(t)$	The rate (at time $t \geq 0$) at which a random triangle neighbour v of u is infected from outside the triangle, given that v was susceptible
$B(t)$	The rate (at time $t \geq 0$) at which a random dynamic line stub neighbour v of u becomes infected from outside the dynamic line joining u and v , given that v was susceptible
$\psi_S(t), \psi_I(t), \psi_R(t)$	The probabilities (at time $t \geq 0$) that a random dynamic stub belonging to u has never been involved in transmitting infection to u and is currently connected to a susceptible, infected, or recovered individual, respectively
$\pi_S(t), \pi_I(t), \pi_R(t)$	The probabilities (at time $t \geq 0$) that a randomly chosen dynamic stub belongs to a susceptible, infected, or recovered individual, respectively

3.2.1 Edge-based compartmental model derivation

We follow the edge-based compartmental modelling approach by considering the fate of a randomly selected test node u , which is prevented from transmitting infection. This assumption is a useful tool that eliminates conditional probability arguments that would need to be considered otherwise [77]. It does not introduce any approximation. At time zero, infection is introduced to a fraction ρ of the population chosen uniformly at random, comprising the initial condition of the system. We assume that the test node u is a member of s static line stubs, t static triangle corners and d dynamic line stubs. Then the probability that u is susceptible is $(1 - \rho)\theta_2^s\theta_3^t\theta_4^d$, where θ_2 is the probability that a random line (2-clique) on the static network layer has not transmitted infection to the test node, θ_3 is the probability that neither of the other nodes in a random triangle on the static network layer have transmitted infection to the test node, and θ_4 is the probability that a random *stub* connected to u on the dynamic network layer has never been involved in transmitting infection to the test node. Assuming we are able to calculate θ_2 , θ_3 and θ_4 as functions of time, we are able to calculate the proportion of susceptible individuals S as a function of time. Given $S(t)$, we use $I(t) = 1 - S(t) - R(t)$ and $\dot{R}(t) = \gamma I(t)$ to calculate $I(t)$ and $R(t)$, completing the system.

Considering θ_2

We divide θ_2 into ϕ_S , ϕ_I and ϕ_R , the probabilities that a random neighbour along a line on the static network layer has not transmitted infection to u , and is susceptible, infected, or recovered, respectively. The probability the neighbour has not transmitted infection to u is $\theta_2 = \phi_S + \phi_I + \phi_R$, and $(1 - \theta_2)$ is the probability that it has transmitted infection to u . The fluxes between these quantities is shown in Figure 3.1. The fluxes from ϕ_I to ϕ_R and from ϕ_I to $(1 - \theta_2)$ are proportional to one another. Both ϕ_R and $(1 - \theta_2)$ are equal to zero at time zero since we assume that no infection or recovery events can occur prior to time zero. By integrating the relation $\frac{d\phi_R}{dt} = \frac{\gamma}{\beta_s} \frac{d(1-\theta_2)}{dt}$, and using the initial condition $\phi_R(0) = (1 - \theta_2(0)) = 0$, we find the relation

$$\phi_R = \frac{\gamma}{\beta_s}(1 - \theta_2). \quad (3.2)$$

Next, we must calculate an expression for ϕ_S . Consider the number of static line stubs attached to an individual that we reach by following a randomly chosen static line. Similarly, consider the number of static triangle corners attached to an individual reached

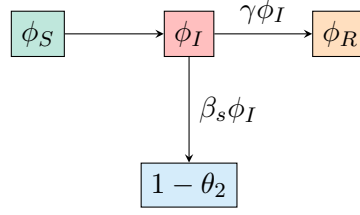


Figure 3.1: **Flow diagram for the flux of a static line partner through different states.** The flux between the probabilities that the test node u is connected by a line (2-clique) on the static network layer to a node v that has not transmitted infection to u and is susceptible (ϕ_S), infectious (ϕ_I) or recovered (ϕ_R), and the probability that v has transmitted infection to u , equal to $(1 - \theta_2)$

by following a randomly chosen static triangle edge, and the number of dynamic line stubs attached to an individual we reach by following a randomly chosen dynamic line. Following edges in this way means we are more likely to arrive at an individual with a higher degree, in direct proportion to that individual's degree [70]. The random number of such lines and triangle corners is described by the *excess degree distribution*, and we calculate the associated probability density functions for each edge type as follows. Denote $q_{s-1,t,d} \propto sp_{s,t,d}$ as the probability of there being $(s-1)$ static line stubs, t triangle corners and d dynamic line stubs connected to a node that we reach by following a static line, not counting the line by which we arrived. Similarly, denote $r_{s,t-1,d} \propto tp_{s,t,d}$ as the probability that if we follow a triangle edge to a node, there are s static line stubs, $(t-1)$ triangle corners and d dynamic line stubs connected to that node, not counting the triangle edge by which we arrived, and $w_{s,t,d-1} \propto dp_{s,t,d}$ as the probability that if we follow a dynamic edge to a node, there are s static line stubs, t triangle corners and $(d-1)$ dynamic line stubs connected to that node, not counting the dynamic edge by which we arrived.

From above, we note that the probability that there are s static line stubs, t triangle corners and d dynamic line stubs attached to a random neighbour of u across a static line (not counting the line it was reached across) is $q_{s-1,t,d} \propto sp_{s,t,d}$. A neighbour reached by following a static line connected to u is susceptible with probability $(1 - \rho)\theta_2^{s-1}\theta_3^t\theta_4^d$ (recall that u cannot transmit infection), where s , t and d are realisations of the excess degree distribution. We calculate ϕ_S by multiplying the probability that a random neighbour across a static line has (s, t, d) neighbours, with the probability the random neighbour is susceptible, summing over all possible values of (s, t, d) , and dividing by $M_s = g^{(x)}(1, 1, 1)$, the expected number of static lines a randomly selected node belongs to. We find

$$\phi_S = \frac{(1 - \rho) \sum_{s,t,d} sp_{s,t,d} \theta_2^{s-1} \theta_3^t \theta_4^d}{M_s} = \frac{(1 - \rho) g^{(x)}(\theta_2, \theta_3, \theta_4)}{g^{(x)}(1, 1, 1)}. \quad (3.3)$$

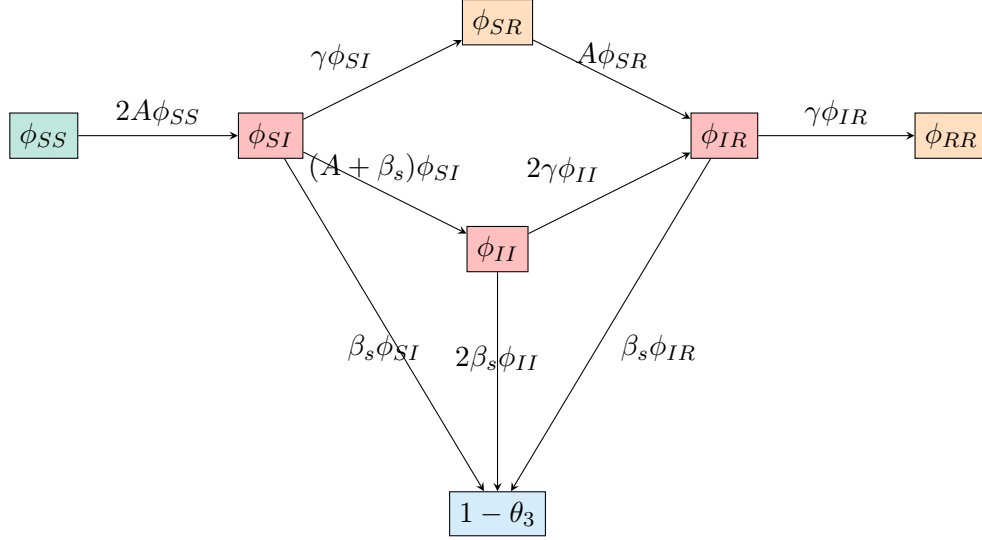


Figure 3.2: **Flow diagram for the flux of two triangle neighbours through different states.** The flux between the probabilities that the test node u is connected in a triangle to two nodes in all possible disease status configurations, where neither triangle neighbour has transmitted infection to u , as well as the probability $(1 - \theta_3)$ that a node $v \neq u$ in the triangle has transmitted infection to the test node u

From the original definition of θ_2 we have

$$\phi_I = \theta_2 - \phi_S - \phi_R. \quad (3.4)$$

We are now able to calculate an expression for θ_2 using equations (3.2)-(3.4), and noting from Figure 3.1 that $\dot{\theta}_2 = -\beta_s \phi_I$:

$$\dot{\theta}_2 = -\beta_s \theta_2 + \beta_s \frac{(1 - \rho)g^{(x)}(\theta_2, \theta_3, \theta_4)}{g^{(x)}(1, 1, 1)} + \gamma(1 - \theta_2). \quad (3.5)$$

Considering θ_3

Since θ_3 denotes the probability that neither of the other nodes in a triangle have transmitted infection to the test node, we must divide θ_3 into six quantities ϕ_{SS} , ϕ_{SI} , ϕ_{SR} , ϕ_{II} , ϕ_{IR} and ϕ_{RR} in order to consider all possible disease status combinations for two individuals. For example, ϕ_{SI} denotes the probability that one triangle neighbour of u is susceptible, whilst the other is infectious, and neither have transmitted infection to u . The flux between the various compartments can be seen in Figure 3.2. There is no simple relation between ϕ_{RR} and θ_3 , so we take a different approach than before. We start with $\dot{\theta}_3$, which satisfies

$$\dot{\theta}_3 = -\beta_s \phi_{SI} - 2\beta_s \phi_{II} - \beta_s \phi_{IR}. \quad (3.6)$$

To calculate elements in the right hand side of (3.6), we must first obtain an expression

for ϕ_{SS} , the probability that both neighbours in a triangle are still susceptible. Under the assumption that no transmission events have occurred in the triangle, the probability that a *single* triangle neighbour of u is susceptible is

$$(1 - \rho) \sum_{s,t,d} t p_{s,t,d} \theta_2^s \theta_3^{t-1} \theta_4^d / M_t = (1 - \rho) g^{(y)}(\theta_2, \theta_3, \theta_4) / g^{(y)}(1, 1, 1),$$

where M_t is the expected number of static triangle corners belonging to a randomly chosen individual. Since we require both triangle neighbours of u to be susceptible, we have

$$\phi_{SS} = \left(\frac{(1 - \rho) g^{(y)}(\theta_2, \theta_3, \theta_4)}{g^{(y)}(1, 1, 1)} \right)^2. \quad (3.7)$$

We choose A to denote the rate at which a single triangle neighbour of u becomes infected from *outside* the triangle. From Figure 3.2 we know that $\frac{d\phi_{SS}}{dt} = -2A\phi_{SS}$, which implies $A = -\frac{d\phi_{SS}}{dt} / 2\phi_{SS}$. To arrive at an explicit formula for A , we begin by calculating $\frac{d\phi_{SS}}{dt}$ via the chain rule:

$$\begin{aligned} \frac{d\phi_{SS}}{dt} &= 2 \left(\frac{(1 - \rho) g^{(y)}(\theta_2, \theta_3, \theta_4)}{g^{(y)}(1, 1, 1)} \right) \frac{d}{dt} \left(\frac{(1 - \rho) g^{(y)}(\theta_2, \theta_3, \theta_4)}{g^{(y)}(1, 1, 1)} \right) \\ &= \frac{2(1 - \rho)^2 g^{(y)}(\theta_2, \theta_3, \theta_4)}{g^{(y)}(1, 1, 1)} \left(\frac{g^{(y)}(1, 1, 1) (g^{(y)}(\theta_2, \theta_3, \theta_4))' - g^{(y)}(\theta_2, \theta_3, \theta_4) (g^{(y)}(1, 1, 1))'}{(g^{(y)}(1, 1, 1))^2} \right), \end{aligned}$$

where the prime ($'$) notation is used to denote the derivative with respect to time t . We know that $(g^{(y)}(1, 1, 1))' = 0$, since $g^{(y)}(1, 1, 1) = \sum_{s,t,d} t p_{s,t,d} \in \mathbb{R}$. Hence

$$\begin{aligned} \frac{d\phi_{SS}}{dt} &= \frac{2(1 - \rho)^2 g^{(y)}(\theta_2, \theta_3, \theta_4)}{g^{(y)}(1, 1, 1)} \left(\frac{g^{(y)}(1, 1, 1) (g^{(y)}(\theta_2, \theta_3, \theta_4))'}{(g^{(y)}(1, 1, 1))^2} \right) \\ &= \frac{2(1 - \rho)^2 g^{(y)}(\theta_2, \theta_3, \theta_4)}{g^{(y)}(1, 1, 1)} \left(\frac{(g^{(y)}(\theta_2, \theta_3, \theta_4))'}{g^{(y)}(1, 1, 1)} \right). \end{aligned}$$

Next, we calculate $(g^{(y)}(\theta_2, \theta_3, \theta_4))'$ using $\frac{dg(x,y,z)}{dt} = \frac{\partial g}{\partial x} \frac{dx}{dt} + \frac{\partial g}{\partial y} \frac{dy}{dt} + \frac{\partial g}{\partial z} \frac{dz}{dt}$ to obtain

$$(g^{(y)}(\theta_2, \theta_3, \theta_4))' = g^{(y,x)}(\theta_2, \theta_3, \theta_4) \dot{\theta}_2 + g^{(y,y)}(\theta_2, \theta_3, \theta_4) \dot{\theta}_3 + g^{(y,z)}(\theta_2, \theta_3, \theta_4) \dot{\theta}_4,$$

where the dot ($\dot{\cdot}$) notation is also used to denote the derivative with respect to time t .

Thus we have

$$\frac{d\phi_{SS}}{dt} = \frac{2(1 - \rho)^2 g^{(y)}(\theta_2, \theta_3, \theta_4)}{g^{(y)}(1, 1, 1)} \left(\frac{(g^{(y)}(\theta_2, \theta_3, \theta_4))'}{g^{(y)}(1, 1, 1)} \right).$$

Using $A = -\frac{d\phi_{SS}}{dt}/2\phi_{SS}$ and some simplification, we find an explicit formula for A :

$$A = - \left(\frac{g^{(y,x)}(\theta_2, \theta_3, \theta_4)\dot{\theta}_2 + g^{(y,y)}(\theta_2, \theta_3, \theta_4)\dot{\theta}_3 + g^{(y,z)}(\theta_2, \theta_3, \theta_4)\dot{\theta}_4}{g^{(y)}(\theta_2, \theta_3, \theta_4)} \right). \quad (3.8)$$

Now we are ready to calculate equations for ϕ_{SI} , ϕ_{II} and ϕ_{IR} . We also require ϕ_{SR} , but do not require a formula for ϕ_{RR} . Using the flow diagram in Figure 3.2, we have

$$\dot{\phi}_{SI} = 2A\phi_{SS} - (A + 2\beta_s + \gamma)\phi_{SI}, \quad (3.9)$$

$$\dot{\phi}_{SR} = \gamma\phi_{SI} - A\phi_{SR}, \quad (3.10)$$

$$\dot{\phi}_{II} = (A + \beta_s)\phi_{SI} - 2(\beta_s + \gamma)\phi_{II}, \quad (3.11)$$

$$\dot{\phi}_{IR} = A\phi_{SR} + 2\gamma\phi_{II} - (\beta_s + \gamma)\phi_{IR}. \quad (3.12)$$

Considering θ_4

To take into account the dynamic rewiring of edges, we introduce $\theta_4 = \psi_S + \psi_I + \psi_R$, where ψ_I denotes the probability that a random dynamic stub belonging to the test node u has never been involved in transmitting infection to u , and is *currently connected* to an infectious node. Other important assumptions with respect to dynamic edge rewiring are the following: we assume that when one partnership ends, a new partnership forms immediately, neglecting any between-partner period, and we assume that edges break at rate η . The flux between the various compartments of interest can be seen in Figure 3.3.

Previously, ϕ_S (which corresponds to ψ_S in this subsection) was calculated explicitly as the probability that the neighbour is susceptible. With dynamic edge rewiring, a line stub that previously transmitted infection to u may later become connected to a susceptible node, so the previous calculation of ϕ_S does not apply here. To find ψ_S , we need to calculate the probability that a *newly formed* edge connects to a susceptible, infectious, or recovered individual. We call these probabilities π_S , π_I and π_R and note that they are equivalent to the probabilities that a randomly chosen dynamic stub belongs to a node in each disease compartment. The flux between these probabilities can be seen in Figure 3.4.

First, we calculate the values π_S , π_I and π_R , beginning with π_S . If we select a dynamic stub at random, the probability that it belongs to an individual partaking in s static lines, t triangles and d dynamic stubs is $dp_{s,t,d}/M_d$, where $M_d = g^{(z)}(1,1,1)$ is the expected number of dynamic edges that a random individual belongs to. At time zero, infection is introduced at random to a proportion ρ of the population. Thus the probability of any node being susceptible at time zero is $(1 - \rho)$. The probability of a node with degree

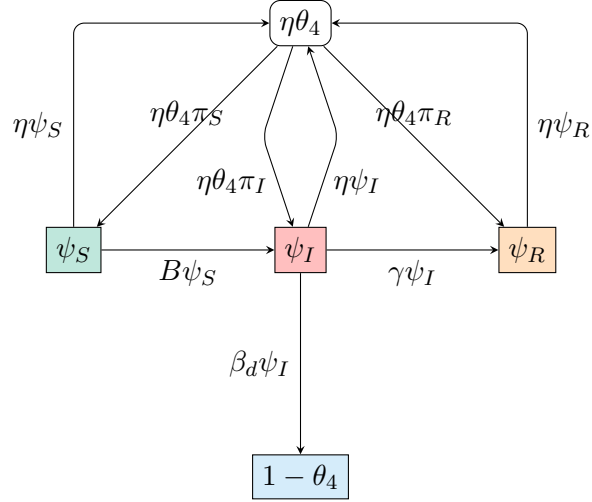


Figure 3.3: **Flow diagram for the flux of a dynamic edge partner through different states.** The flux between the probabilities $\theta_4 = \psi_S + \psi_I + \psi_R$ that a random stub currently connected to u on the dynamic network layer has never been involved in transmitting infection to u . Note that the compartment denoted $\eta\theta_4$ is not a compartment in the typical sense. When edges break (at rate η) in the model, moving into ‘compartment’ $\eta\theta_4$, new edges are formed *immediately* without delay, moving straight back into compartments ψ_S , ψ_I or ψ_R . π_S , π_I and π_R denote the probabilities that a randomly chosen dynamic stub belongs to a susceptible, infected, or recovered node, respectively

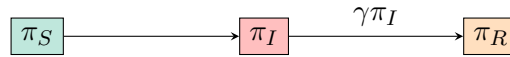


Figure 3.4: **Flow diagram for the flux of a dynamic line stub through different states.** The flux between π_S , π_I and π_R , the probabilities that a randomly chosen dynamic stub belongs to a susceptible, infected or recovered node, respectively

(s, t, d) being susceptible after some time, given that it was susceptible at time zero, is $\theta_2^s \theta_3^t \theta_4^d$. Hence $\pi_S = (1 - \rho) \sum_{s,t,d} p_{s,t,d} d \theta_2^s \theta_3^t \theta_4^d / M_d$, with the summation taken over all degree possibilities described by the probability mass function $p_{s,t,d}$. Stubs belonging to infected nodes become stubs belonging to recovered nodes at rate γ , hence $\dot{\pi}_R = \gamma \pi_I$, and $\pi_I = 1 - \pi_S - \pi_R$. The equation for π_S can be condensed using the PGF (3.1), so we have

$$\pi_S = \frac{(1 - \rho) \sum_{s,t,d} p_{s,t,d} d \theta_2^s \theta_3^t \theta_4^d}{\sum_{s,t,d} p_{s,t,d} d} = \frac{(1 - \rho) \theta_4 g^{(z)}(\theta_2, \theta_3, \theta_4)}{g^{(z)}(1, 1, 1)}, \quad (3.13)$$

$$\pi_I = 1 - \pi_S - \pi_R, \quad (3.14)$$

$$\dot{\pi}_R = \gamma \pi_I. \quad (3.15)$$

To complete the system we need to calculate the flux $B\psi_S$ from ψ_S to ψ_I by solving a differential equation for ψ_S . B describes the rate at which a susceptible dynamic-edge neighbour v of u becomes infected from outside the dynamic edge joining u and v . Consider a random test node u and a random dynamic-edge neighbour v of u , at some time t . Let ζ denote the probability that the two stubs joining u and v have not previously been involved in transmitting infection to u or to v , prior to the $u-v$ edge forming. The probability that v is susceptible and that u 's stub has not previously transmitted to u is $\zeta(1 - \rho)\theta_2^s \theta_3^t \theta_4^{d-1}$, where s is the number of static lines v partakes in, t is the number of triangles v partakes in, and d is the dynamic line stub degree of v . Since we do not know the values (s, t, d) for v , we must consider all possible combinations of degrees. The probability of a randomly chosen dynamic stub belonging to a node with degree (s, t, d) is $dp_{s,t,d}/g^{(z)}(1, 1, 1)$. We conclude that

$$\psi_S = \frac{\zeta(1 - \rho) \sum_{s,t,d} p_{s,t,d} d \theta_2^s \theta_3^t \theta_4^{d-1}}{g^{(z)}(1, 1, 1)} = \frac{\zeta(1 - \rho) g^{(z)}(\theta_2, \theta_3, \theta_4)}{g^{(z)}(1, 1, 1)}.$$

To calculate the derivative of ψ_S , we first consider the derivative of ζ . This is given by subtracting the rate at which such edges break, $\eta\zeta$, from the rate at which such edges form, $\eta\theta_4^2$ (one θ_4 for u 's stub and one for v 's stub). We have

$$\dot{\zeta} = \eta\theta_4^2 - \eta\zeta.$$

We have an expression for $\dot{\zeta}$, so the derivative of ψ_S can be found via the chain rule:

$$\begin{aligned}
\dot{\psi}_S &= \dot{\zeta} \frac{(1-\rho)g^{(z)}(\theta_2, \theta_3, \theta_4)}{g^{(z)}(1, 1, 1)} + \frac{\zeta(1-\rho)}{g^{(z)}(1, 1, 1)} \left(g^{(z)}(\theta_2, \theta_3, \theta_4) \right)' \\
&= \frac{\eta\theta_4^2(1-\rho)g^{(z)}(\theta_2, \theta_3, \theta_4)}{g^{(z)}(1, 1, 1)} - \frac{\eta\zeta(1-\rho)g^{(z)}(\theta_2, \theta_3, \theta_4)}{g^{(z)}(1, 1, 1)} + \frac{\zeta(1-\rho)}{g^{(z)}(1, 1, 1)} \left(g^{(z)}(\theta_2, \theta_3, \theta_4) \right)' \\
&= \eta\theta_4\pi_S - \eta\psi_S + \frac{\zeta(1-\rho)}{g^{(z)}(1, 1, 1)} \left(g^{(z,x)}(\theta_2, \theta_3, \theta_4)\dot{\theta}_2 + g^{(z,y)}(\theta_2, \theta_3, \theta_4)\dot{\theta}_3 + g^{(z,z)}(\theta_2, \theta_3, \theta_4)\dot{\theta}_4 \right) \\
&= \eta\theta_4\pi_S - \eta\psi_S + \frac{\psi_S \left(g^{(z,x)}(\theta_2, \theta_3, \theta_4)\dot{\theta}_2 + g^{(z,y)}(\theta_2, \theta_3, \theta_4)\dot{\theta}_3 + g^{(z,z)}(\theta_2, \theta_3, \theta_4)\dot{\theta}_4 \right)}{g^{(z)}(\theta_2, \theta_3, \theta_4)},
\end{aligned}$$

with simplifications achieved by utilising $\pi_S = (1-\rho)\theta_4g^{(z)}(\theta_2, \theta_3, \theta_4)/g^{(z)}(1, 1, 1)$ and $\psi_S = \zeta(1-\rho)g^{(z)}(\theta_2, \theta_3, \theta_4)/g^{(z)}(1, 1, 1)$. From Figure 3.3 we have $\dot{\psi}_S = \eta\theta_4\pi_S - \eta\psi_S - B\psi_S$, so we calculate the flux between compartments ψ_S and ψ_I using the rate

$$B = - \left(\frac{g^{(z,x)}(\theta_2, \theta_3, \theta_4)\dot{\theta}_2 + g^{(z,y)}(\theta_2, \theta_3, \theta_4)\dot{\theta}_3 + g^{(z,z)}(\theta_2, \theta_3, \theta_4)\dot{\theta}_4}{g^{(z)}(\theta_2, \theta_3, \theta_4)} \right). \quad (3.16)$$

The ψ_S to ψ_I flux is the product of ψ_S , the probability that a random dynamic stub has not transmitted infection to the test node u and is currently connected to a susceptible node, with rate B , the rate at which a susceptible dynamic-edge neighbour v of u becomes infected from outside the dynamic edge joining u and v . Following the flow diagram in Figure 3.3, we have the differential equations

$$\dot{\theta}_4 = -\beta_d\psi_I, \quad (3.17)$$

$$\dot{\psi}_S = \eta\theta_4\pi_S - (B + \eta)\psi_S, \quad (3.18)$$

$$\dot{\psi}_I = B\psi_S + \eta\theta_4\pi_I - (\eta + \gamma + \beta_d)\psi_I, \quad (3.19)$$

$$\dot{\psi}_R = \gamma\psi_I + \eta\theta_4\pi_R - \eta\psi_R. \quad (3.20)$$

Population-level equations

We began the EBCM derivation by considering the probability of a randomly selected test node u (which is prevented from transmitting infection) being susceptible as $\theta_2^s\theta_3^t\theta_4^d$, given that the node has degree (s, t, d) . Since we have calculated formulae for θ_2 , θ_3 and θ_4 , we can derive population-level equations describing the proportion of the population in each

disease compartment at each point in time:

$$S(t) = (1 - \rho)g(\theta_2(t), \theta_3(t), \theta_4(t)) = (1 - \rho) \sum_{s,t,d} p_{s,t,d} \theta_2(t)^s \theta_3(t)^t \theta_4(t)^d, \quad (3.21)$$

$$I(t) = 1 - S(t) - R(t), \quad (3.22)$$

$$\dot{R}(t) = \gamma I(t). \quad (3.23)$$

Equations (3.1)-(3.23) form a complete system describing an SIR epidemic spreading across a dual-layer multiplex network consisting of a static network layer constructed from line stubs and triangle corners and a dynamic network layer constructed from line stubs only, where edges rewire and degrees are conserved.

3.2.2 Deriving the basic reproduction number R_0

The basic reproduction number R_0 is defined as the average number of infections caused by a single infectious individual, early in an epidemic process, in an otherwise susceptible population. In the model, a multiplex network structure is generated using three distinct edge distributions (static line stubs, static triangle corners and dynamic line stubs). To compute R_0 we must consider the average number of infections caused across each type of edge, whilst also considering the type of edge that the infection was originally *received* across. With 3 edge types, this constitutes 9 values, grouped together to form the next generation matrix

$$\mathbf{G} = \begin{pmatrix} G_{ss} & G_{st} & G_{sd} \\ G_{ts} & G_{tt} & G_{td} \\ G_{ds} & G_{dt} & G_{dd} \end{pmatrix},$$

where matrix element G_{ij} describes the average number of infections caused across edges of type j , where the infector *received* infection across an edge of type i . Following the next generation matrix approach [20], the value of R_0 is found via the leading eigenvalue of the matrix \mathbf{G} , or equivalently, the eigenvalue with greatest magnitude. We note that the matrix \mathbf{G} defined here is the transpose of the next generation matrix as defined in [20]. However, this discrepancy does not affect the eigenvalues or therefore the value R_0 .

To find R_0 , we begin by deriving expressions for values in the first column of \mathbf{G} . Firstly, consider the non-diagonal matrix entries G_{ts} and G_{ds} . We want to compute the expected number of infection events occurring across static lines, when individuals contracted infection across a triangle edge or a dynamic line. In both cases, we require the expected static line stub degree, multiplied by the expected number of infections caused

across a *single* static line attached to the infectious individual. Say the expected static line stub degree is denoted $\langle k_s \rangle$. Now we require the expected number of infections caused across a single static edge attached to an infectious individual, in an otherwise susceptible population. A single static edge joining a susceptible and an infectious individual, in an otherwise susceptible population, has two event possibilities: a single recovery, or a single infection. Denote X as the random variable describing the number of infection events occurring across a single static line joining a susceptible to an infectious individual, in an otherwise susceptible population. Using the expectation formula, and since there can only be zero or one infection events occurring across such an edge, we find the expected number of infections across a static line joining a susceptible to an infectious individual simply as $\mathbb{P}(X = 1)$. The probability of a single infection occurring across such a static edge, prior to any recovery, is $\frac{\beta_s}{\beta_s + \gamma}$. Thus we can say that $G_{ts} = G_{ds} = \langle k_s \rangle \frac{\beta_s}{\beta_s + \gamma}$.

Finally, we calculate an expression for the diagonal matrix element G_{ss} , by multiplying the expected *excess* static line stub degree, denoted $\langle s \rangle$, by the expected number of infections caused across a single static line joining a susceptible individual to an infectious individual in an otherwise susceptible population. Following the same argument for G_{ts} and G_{ds} , we compute the expected number of infection events for G_{ss} as $\frac{\beta_s}{\beta_s + \gamma}$, and we obtain $G_{ss} = \langle s \rangle \frac{\beta_s}{\beta_s + \gamma}$.

Next we derive expressions for the values G_{st} , G_{tt} and G_{dt} in the second column of the matrix \mathbf{G} . We firstly consider the non-diagonal elements G_{st} and G_{dt} . Both G_{st} and G_{dt} are calculated by multiplying the expected triangle *corner* degree, denoted $\langle k_t \rangle$, by the expected number of infection events caused within a *single* triangle attached to an infectious node in an otherwise susceptible population. In a single triangle comprised of two susceptible individuals attached to an infectious individual, there are a finite number of infection event possibilities: either no further infections occur (the infectious individual recovers), one infection event occurs, or two infection events occur. Define Y as the random variable describing the number of infection events within such a triangle. Using the expectation formula, we find the expected number of infection events within a triangle comprised of two susceptible individuals and an infective, in an otherwise susceptible population, as $\mathbb{P}(Y = 1) + 2 \cdot \mathbb{P}(Y = 2)$. To continue, we must compute the probabilities $\mathbb{P}(Y = 1)$ and $\mathbb{P}(Y = 2)$ explicitly. $\mathbb{P}(Y = 1)$ describes the probability that the original infective infects *one* out of two triangle neighbours. In this case, either one of the two susceptible neighbours can become infectious, and both infectious triangle members must then recover, so that it is impossible for any more than one infection event to occur. In a

triangle comprised of a single infective and two susceptible nodes, there are four distinct nodal orders in which a single infection event is followed by the recovery of both infectious nodes. We find

$$\begin{aligned}\mathbb{P}(Y = 1) &= \frac{4\beta_s}{2\beta_s + \gamma} \left(\frac{\gamma}{2\beta_s + 2\gamma} \right) \left(\frac{\gamma}{\beta_s + \gamma} \right) \\ &= \frac{2\beta_s}{2\beta_s + \gamma} \left(\frac{\gamma}{\beta_s + \gamma} \right)^2.\end{aligned}$$

Considering $\mathbb{P}(Y = 2)$ is more complex, as there are two distinct ways in which two infection events can occur in a triangle between an infective and two susceptible individuals. Firstly, the original infective can infect both of its triangle neighbours consecutively, prior to any recovery events. The probability of both triangle infection events occurring in succession is given by $\left(\frac{2\beta_s}{2\beta_s + \gamma} \right) \left(\frac{2\beta_s}{2\beta_s + 2\gamma} \right) = \left(\frac{2\beta_s}{2\beta_s + \gamma} \right) \left(\frac{\beta_s}{\beta_s + \gamma} \right)$. Secondly, the original infective can cause two triangle infections via *three* consecutive events. In this case, the originally infectious triangle member firstly infects one susceptible triangle neighbour at rate $\frac{2\beta_s}{2\beta_s + \gamma}$. The triangle is now comprised of two infectious individuals attached to a single susceptible individual. The second event to occur is a recovery of either the original infector or its first infectee, occurring at rate $\frac{2\gamma}{2\beta_s + 2\gamma} = \frac{\gamma}{\beta_s + \gamma}$. The triangle is now comprised of a susceptible, an infective, and a recovered individual, in an otherwise susceptible population. Following the recovery event, the final event is an infection of the remaining susceptible triangle member, occurring at rate $\frac{\beta_s}{\beta_s + \gamma}$. The probability of all three events occurring in succession is thus $\frac{2\beta_s}{2\beta_s + \gamma} \left(\frac{\gamma}{\beta_s + \gamma} \right) \left(\frac{\beta_s}{\beta_s + \gamma} \right)$.

In the latter case of an infection, followed by a recovery, followed by another infection within a triangle originally composed of an infective and two susceptible individuals in an otherwise susceptible population, the original infector may not be directly involved in every single infection event. However, for the purposes of deriving R_0 , we say that the original infector *caused* these infections, regardless of the order in which triangle members recover and infect one another.

Since there are two distinct ways in which two infections can take place within a triangle comprised of an infective and two susceptible individuals, we take the sum of both individual probabilities to obtain $\mathbb{P}(Y = 2)$:

$$\begin{aligned}\mathbb{P}(Y = 2) &= \frac{2\beta_s}{2\beta_s + \gamma} \left(\frac{\beta_s}{\beta_s + \gamma} \right) + \frac{2\beta_s}{2\beta_s + \gamma} \left(\frac{\gamma}{\beta_s + \gamma} \right) \left(\frac{\beta_s}{\beta_s + \gamma} \right) \\ &= \frac{2\beta_s}{2\beta_s + \gamma} \left(\frac{\beta_s}{\beta_s + \gamma} \right) \left[1 + \frac{\gamma}{\beta_s + \gamma} \right].\end{aligned}$$

We find the expected number of infection events within a triangle comprised of two susceptible individuals and an infective, in an otherwise susceptible population, as

$$\begin{aligned}\mathbb{P}(Y = 1) + 2 \cdot \mathbb{P}(Y = 2) &= \frac{2\beta_s}{2\beta_s + \gamma} \left(\frac{\gamma}{\beta_s + \gamma} \right)^2 + \frac{4\beta_s}{2\beta_s + \gamma} \left(\frac{\beta_s}{\beta_s + \gamma} \right) \left[1 + \frac{\gamma}{\beta_s + \gamma} \right] \\ &= \frac{2\beta_s}{2\beta_s + \gamma} \left[2 - \left(\frac{\gamma}{\beta_s + \gamma} \right)^2 \right].\end{aligned}$$

Then we have $G_{st} = \langle k_t \rangle \frac{2\beta_s}{2\beta_s + \gamma} \left[2 - \left(\frac{\gamma}{\beta_s + \gamma} \right)^2 \right] = G_{dt}$, where $\langle k_t \rangle$ denotes the expected static triangle *corner* degree. Finally, we have $G_{tt} = \langle t \rangle \frac{2\beta_s}{2\beta_s + \gamma} \left[2 - \left(\frac{\gamma}{\beta_s + \gamma} \right)^2 \right]$, where $\langle t \rangle$ denotes the expected *excess* static triangle corner degree.

We conclude by deriving elements from the third column of \mathbf{G} , starting with non-diagonal matrix elements G_{sd} and G_{td} . In both cases, we multiply the expected dynamic line stub degree, denoted $\langle k_d \rangle$, by the expected number of infection events occurring across a single dynamic line stub attached to an infectious individual, in an otherwise susceptible population.

The probability of a dynamic stub attached to an infective in an otherwise susceptible population transmitting infection *at least once* is $\frac{\beta_d}{\beta_d + \gamma}$. If such an infection occurs, the I-S pairing becomes an I-I pairing with a dynamic edge joining the two individuals. The probability of a dynamic I-I edge rewiring, prior to any recovery event, is $\frac{\eta}{\eta + \gamma}$. We can assume that any I-I edge rewires to become an I-S edge in the limit of large population size, since we are early on in an epidemic process, and we began with an otherwise susceptible population. The probability that an infectious dynamic stub infects its new susceptible neighbour is $\frac{\beta_d}{\beta_d + \gamma}$. This rewiring and infecting process can occur an arbitrary number of times in the model. The expected number of infections of this type can be calculated by taking the sum

$$\sum_{n=0}^{\infty} \frac{\beta_d}{\beta_d + \gamma} r^n = \frac{\beta_d}{\beta_d + \gamma} \left(\frac{1}{1 - r} \right),$$

by the geometric series, and where r is defined as $\frac{\eta\beta_d}{(\eta + \gamma)(\beta_d + \gamma)}$, the probability of an infectious individual's dynamic edge rewiring, followed immediately by its dynamic stub infecting the new (susceptible) neighbour across the rewired edge. We obtain the matrix values $G_{sd} = \langle k_d \rangle \frac{\beta_d}{\beta_d + \gamma} \left(\frac{1}{1 - r} \right) = G_{td}$.

Finally, we compute G_{dd} , defined as the expected number of infections caused across dynamic edges, where the infector received infection across a dynamic edge itself. Firstly, consider the *single* dynamic I-I edge which originally infected our individual. The probability of the edge rewiring, leaving our infective in an I-S dynamic edge pairing, is $\frac{\eta}{\eta + \gamma}$.

The probability of the infectious dynamic stub infecting the new susceptible neighbour is $\frac{\beta_d}{\beta_d + \gamma}$. Thus the probability that the dynamic stub which originally contracted infection infects $\geq n$ individuals is r^n , where $r = \frac{\eta\beta_d}{(\eta + \gamma)(\beta_d + \gamma)}$. We compute the expected number of infections of this type by taking the sum of r^n for $n = 1 : \infty$

$$\sum_{n=1}^{\infty} r^n = \frac{r}{1-r},$$

by the geometric series. Now consider the remaining dynamic edges associated with our infectious individual. We require the expected number of infections caused by a single edge of this type. Using the same argument as for G_{sd} and G_{td} , we find the expected number of infections caused by one dynamic edge attached to our infectious individual as $\frac{\beta_d}{\beta_d + \gamma} \left(\frac{1}{1-r} \right)$. Thus we find $G_{dd} = \frac{r}{1-r} + \langle d \rangle \frac{\beta_d}{\beta_d + \gamma} \left(\frac{1}{1-r} \right)$, where $\langle d \rangle$ is the expected excess dynamic line stub degree.

In detail, the next generation matrix \mathbf{G} takes the form

$$\begin{pmatrix} \langle s \rangle \frac{\beta_s}{\beta_s + \gamma} & \langle k_t \rangle \frac{2\beta_s}{2\beta_s + \gamma} \left(2 - \left(\frac{\gamma}{\beta_s + \gamma} \right)^2 \right) & \langle k_d \rangle \frac{\beta_d}{\beta_d + \gamma} \left(\frac{1}{1-r} \right) \\ \langle k_s \rangle \frac{\beta_s}{\beta_s + \gamma} & \langle t \rangle \frac{2\beta_s}{2\beta_s + \gamma} \left(2 - \left(\frac{\gamma}{\beta_s + \gamma} \right)^2 \right) & \langle k_d \rangle \frac{\beta_d}{\beta_d + \gamma} \left(\frac{1}{1-r} \right) \\ \langle k_s \rangle \frac{\beta_s}{\beta_s + \gamma} & \langle k_t \rangle \frac{2\beta_s}{2\beta_s + \gamma} \left(2 - \left(\frac{\gamma}{\beta_s + \gamma} \right)^2 \right) & \frac{r}{1-r} + \langle d \rangle \frac{\beta_d}{\beta_d + \gamma} \left(\frac{1}{1-r} \right) \end{pmatrix}, \quad (3.24)$$

where $\langle k_s \rangle$, $\langle k_t \rangle$ and $\langle k_d \rangle$ denote the expected static line stub, static triangle *corner* and dynamic line stub degrees, $\langle s \rangle$, $\langle t \rangle$ and $\langle d \rangle$ denote the expected *excess* static line stub, static triangle *corner* and dynamic line stub degrees, and $r = \frac{\eta\beta_d}{(\eta + \gamma)(\beta_d + \gamma)}$. The basic reproduction number R_0 is the eigenvalue of the next generation matrix (3.24) with greatest magnitude.

3.2.3 Model implementation

A variable-order stiff differential equation solver (*ode15s* in the MATLAB environment) was used to solve all relevant systems of equations. Initial conditions were specified, consisting of appropriate degree distributions and parameters for each edge-based compartmental model type, and of a user specified end time for the computation.

Solutions to equations (3.1)-(3.23) were found using both interdependent and independent distributions for the three edge types. For interdependent distributions, a single probability distribution governed the distribution of *pairs* of edge stubs, and additional model parameters $(p_s + p_t + p_d) \equiv 1$ were used to distribute each pair of stubs into: two static line stubs (with probability p_s), a single static triangle corner (with probability

p_t), or two dynamic line stubs (with probability p_d). In such cases we used a negative binomial distribution for pairs of edge stubs with parameters p and r describing the probability of success in a single trial and the number of trial successes respectively, where the distribution itself is generated by $g_{nb}(x; r, p) = (\frac{p}{1-(1-p)^x})^r$ and models the number of failures before a specified number of successes is reached in a series of identical, independent Bernoulli trials. We also utilised a discrete homogeneous distribution for pairs of edge stubs where all individuals had identical degree. For independent distributions, we used three separate binomial distributions for the number of static line stubs, static triangle corners and dynamic line stubs.

3.2.4 Simulation implementation

To test the validity of solutions to equations (3.1)-(3.23), found in the MATLAB environment, Gillespie simulations [32] were implemented to produce statistically-correct trajectories of SIR epidemic processes occurring on equivalent static-dynamic multiplex networks. Prior to each simulation, static and ‘dynamic’ adjacency matrices were generated according to a configuration model approach, described as follows: for a population of N individuals, three vectors of length N were generated to record the number of static line stubs, static triangle corners, and dynamic line stubs associated with each individual, according to user-specified degree distributions provided to the script. The script ensured that the total number of static line stubs was even, the total number of dynamic line stubs was even, and that the total number of static triangle corners was a multiple of three.

Firstly, the static network layer was generated using vectors containing the number of static line stubs and triangle corners each individual partook in. Pairs of static line stubs and triples of static triangle corners were selected at random. Provided potential static lines and triangles did not generate self-loops (where an individual is joined to itself with an edge) or double edges (where an edge exists more than once within the static network layer), they were added to the static adjacency matrix. The *unmatched* static line stubs and static triangle corners lists were updated, and the process continued until all static line stubs and triangle corners were successfully matched.

Secondly, the initial structure of the dynamic network layer was generated using the vector storing the number of dynamic line stubs each individual partook in. Pairs of dynamic line stubs were selected at random. Provided a potential dynamic edge did not generate a self-loop or a double-edge within the dynamic network layer, it was added to the dynamic adjacency matrix. Successfully paired dynamic stubs were removed from

the *unmatched* stubs list, and the process continued until all dynamic line stubs were successfully matched.

The nature of this configuration model approach meant that the wiring processes for the static and dynamic network layers may have had to be restarted multiple times in order to achieve final network structures. Once all static line stubs, static triangle corners and dynamic line stubs had been wired up, the configuration process was complete. Although the script prevented double-edges from occurring within each network layer, it was possible for double-edges to occur *across* the network layers, i.e. for two individuals to share both a static and a dynamic connection simultaneously.

Given static and dynamic adjacency matrices describing the multiplex network structure, simulated epidemic processes were implemented. In each Gillespie simulation, ρN initially infectious individuals were selected at random from the population. At each time step, a vector of length $(N + 1)$ described the state transition rate (infection or recovery) for all N individuals, followed by a single edge swapping rate, $\frac{\eta M}{2}$, where $M :=$ total number of edges in the dynamic network layer. Inter-event times followed an exponential distribution with scale parameter $\frac{1}{R}$, where $R :=$ the sum of the rates vector at the current time step. Each event occurring was either an infection, a recovery or an edge swap. Uniformly distributed random numbers were generated at each time step to determine the next event to occur. When an edge swap event occurred, the script selected two dynamic edges at random, ensuring that all four nodes involved in these edges were unique. The script also ensured that the proposed new dynamic edges did not already exist within the dynamic network layer. Given these conditions, an edge swap occurred and the Gillespie process continued. The process terminated once the user specified end time was reached.

3.3 Results

In what follows, we assess the validity of equations (3.1)-(3.23) and of the basic reproduction number R_0 , obtained via the next generation matrix (3.24). We firstly consider two extreme cases of the multiplex model: when either the static or the dynamic network layers are negligible (close to zero). In such cases, we show that predictions made by equations (3.1)-(3.23) resolve to predictions made by existing uniplex EBCM equations. When the full multiplex model is considered, with static and dynamic network elements present, there exists no basis for comparison other than generating exact simulations of the epidemic process. To this end, we utilise Gillespie simulations to demonstrate the validity of equations (3.1)-(3.23) in predicting the epidemic process for a number of multiplex

network configurations. By solely considering the predictions of equations (3.1)-(3.23), we explore the consequences of varying individual model parameters and of considering various combinations of model parameters $(p_s + p_t + p_d) \equiv 1$, governing the contributions of each edge type. Further, we explore the contributions of each edge type and how the resulting final epidemic size is altered within a systematic consideration of combinations of model parameters β_s , β_d and η . Finally, we test the performance of the derived basic reproduction number R_0 in predicting the outcome of an epidemic and we explore variations in the value of R_0 and the associated final epidemic size predicted by equations (3.1)-(3.23) when altering the rate of rewiring, the extent of clustering, and the average degree in the multiplex model.

3.3.1 Model convergence to existing uniplex model equations

Model without dynamic layer

When the dynamic network component of the dual-layer static-dynamic multiplex is removed, the model reduces to describe an SIR epidemic on a static uniplex network generated by lines and triangles. Biologically speaking, this reduced model tracks the epidemic as it spreads across persistent connections in a population with community structure. The EBCM approach was followed to derive equations describing an SIR epidemic on such a network in [125].

By comparing predictions made by uniplex model equations in [125] with those of multiplex model equations (3.1)-(3.23) when dynamic network elements are close to zero, we were able to test the multiplex model's convergence (Figure 3.5). Excellent agreement was observed between multiplex model equations where dynamic network elements are negligible, uniplex model equations [125] and Gillespie simulated epidemics on equivalent multiplex networks, for a number of scenarios with varying forces of infection.

Model without static layer

When the static component of the dual-layer static-dynamic multiplex is removed, the model describes an SIR epidemic on a dynamic uniplex network generated by lines, where edges rewire at constant rate η and degrees are conserved. Biologically, the reduced model describes an epidemic spreading through a population where connections between pairs of individuals are temporary but the number of connections an individual partakes in remains fixed. The EBCM approach was followed to derive equations describing an SIR epidemic spreading on such a network in [77].

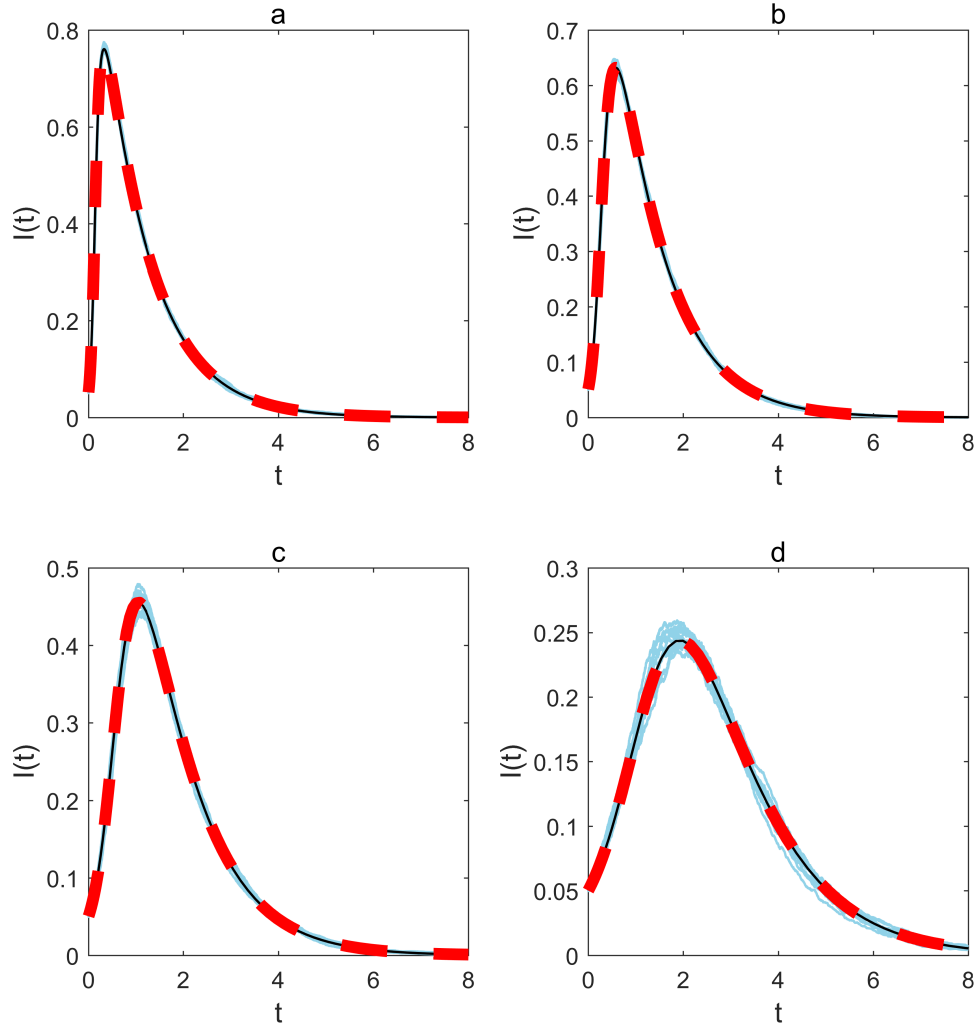


Figure 3.5: Multiplex model convergence — no dynamic layer, with simulation. The time evolution of infection prevalence for the original EBCM of an SIR epidemic on a static uniplex network (solid black line), for the proposed EBCM of an SIR epidemic on a dual-layer multiplex with the dynamic network layer being close to zero (thick dashed red line), and for 10 Gillespie simulations of the SIR epidemic on a single network of size $N = 5000$ (solid blue lines). In all panels $\gamma = 1$, $\rho = 0.05$, and $p = 0.5$ and $r = 10$ generate a negative binomial distribution for pairs of edge stubs. For the original static derivation (solid black line) $p_s = 0.5 = p_t$, describing the proportion of edge-pairs that are split into two single lines or remain as a triangle corner, respectively. For the multiplex derivation (thick dashed red line) $\beta_s = \beta_d$, $\eta = 0.01$, and $p_s = 0.4999999$, $p_t = 0.5$ and hence $p_d = 10^{-7}$ describe the proportion of edge-pairs that become two static lines, a static triangle corner, or two dynamic edges respectively. (a) $\beta's = 1$, $C = 0.02677$, (b) $\beta's = 0.5$, $C = 0.02670$, (c) $\beta's = 0.25$, $C = 0.02658$, (d) $\beta's = 0.125$, $C = 0.02685$, where C denotes the global clustering coefficient of each static network layer generated for simulation

Excellent agreement was observed between predictions made by equations (3.1)-(3.23) when static network elements are close to zero, output from the dynamic fixed-degree

derivation in [77] and Gillespie simulations describing the SIR epidemic and edge rewire processes occurring simultaneously on equivalent multiplex networks, for a number of setups with varying forces of infection (Figure 3.6).

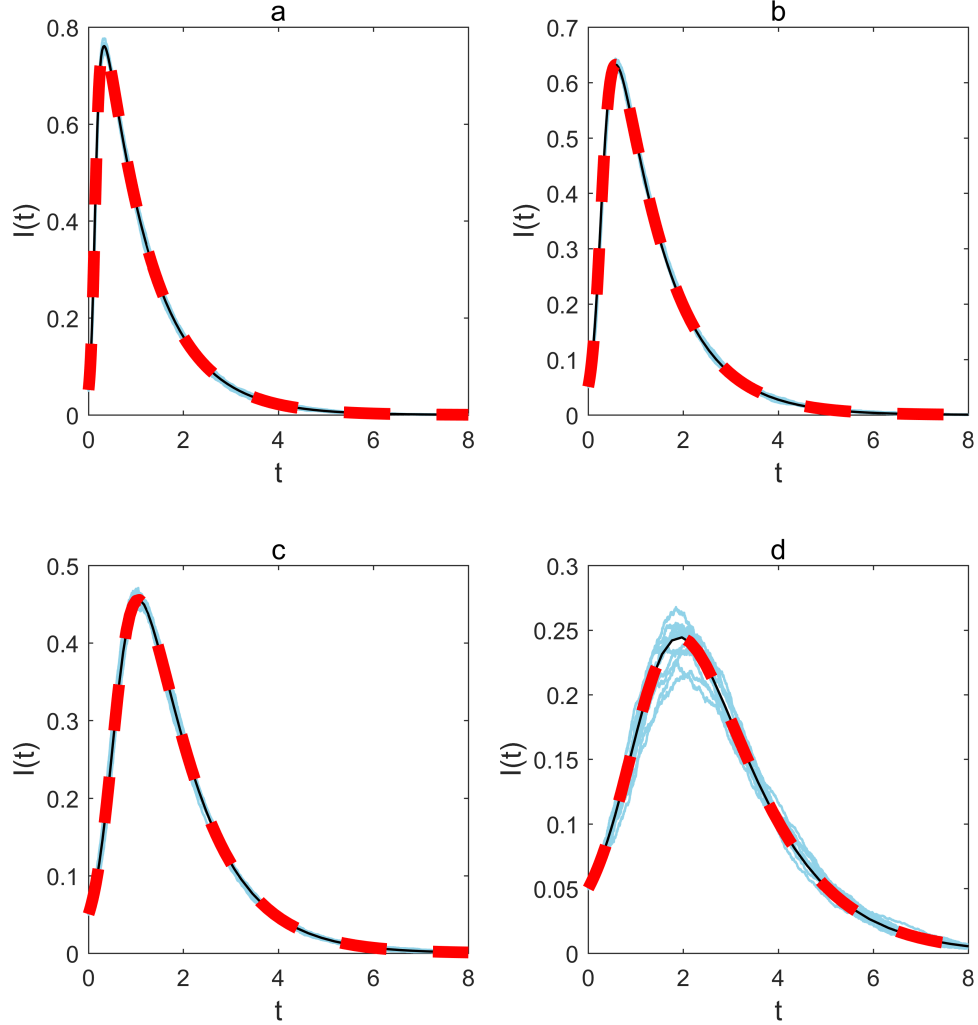


Figure 3.6: **Multiplex model convergence — no static layer, with simulation.**

The time evolution of infection prevalence for the original EBCM of an SIR epidemic on a dynamic uniplex network with conserved degrees and edge re-wiring (solid black line), for the proposed multiplex EBCM of an SIR epidemic with the static network layer being close to zero (thick dashed red line), and for 10 Gillespie simulations of the process on a single network of size $N = 5000$ (solid blue lines). In all panels $\gamma = 1$, $\rho = 0.05$, and $p = 0.5$ and $r = 10$ generate a negative binomial distribution for pairs of edge stubs. For the original conserved-degree derivation (solid black line) $p_d = 1$, indicating that all edge-pairs become two disjoint dynamic edges. For the multiplex derivation (thick dashed red line), $\eta = 0.01$ and $p_s = p_t = 10^{-7}$ and $p_d = 0.9999998$ describe the proportion of edge-pairs that become two static lines, single triangle corners, or two dynamic edges respectively. (a) $\beta's = 1$, $C = 0.004944$, (b) $\beta's = 0.5$, $C = 0.005285$, (c) $\beta's = 0.25$, $C = 0.005344$, (d) $\beta's = 0.125$, $C = 0.005127$, where C denotes the global clustering coefficient of each dynamic network layer generated for simulation, at time zero

3.3.2 Model validation by comparison with simulation

We have observed excellent agreement between multiplex model predictions, uniplex model predictions and Gillespie simulated epidemics in extreme cases where either static or dynamic network elements are negligible (Figures 3.5 - 3.6). When multiplex network elements are non-negligible, static and dynamic network layers coexist in the model. In such cases, Gillespie simulated epidemics become the sole basis for assessing the validity of multiplex model equations (3.1)-(3.23).

A number of comparisons have been made between multiplex model predictions and Gillespie simulations when static and dynamic network elements coexist (Figures 3.7 - 3.8). Excellent agreement was observed for a number of comparisons with various average degrees (imposed via negative binomial parameters p and r , describing the distribution governing pairs of edge stubs) and various levels of clustering (imposed by varying parameter p_t with the constraint $(p_s + p_t + p_d) \equiv 1$) (Figure 3.7). Excellent agreement was also observed for a number of comparisons with various combinations of the multiplex model's infection parameters β_s and β_d (Figure 3.8).

3.3.3 A brief exploration of parameter spaces

Having observed excellent agreement between simulated epidemic processes and equivalent predictions made by multiplex model equations, we investigated the effects of varying single parameters on the dynamics of epidemics predicted by equations (3.1)-(3.23). In total, 9 individual model parameters were varied systematically whilst all (or the majority of) other parameters were held constant (Figure 3.9). Across all parameters being varied, an identical baseline parameter set was utilised, with the resulting prediction made by equations (3.1)-(3.23) plotted in black to enable ease of comparison between different parameter scenarios.

This brief exploration highlights the effect that increasing or decreasing a single parameter has on the global dynamics of an SIR epidemic spreading across a dual-layer static-dynamic multiplex. Larger values of p , where p describes the probability of success in a single Bernoulli trial, generate a negative binomial distribution with smaller average degree and a reduction in variance, slowing the epidemic's spread. Larger values of r , where r denotes the number of successful Bernoulli trials that must be reached before the experiment is stopped, led the epidemic to spread more rapidly due to an increase in average degree and variance of the negative binomial distribution for pairs of edge stubs. Varying the rewiring rate η led to less pronounced differences, where larger values of η

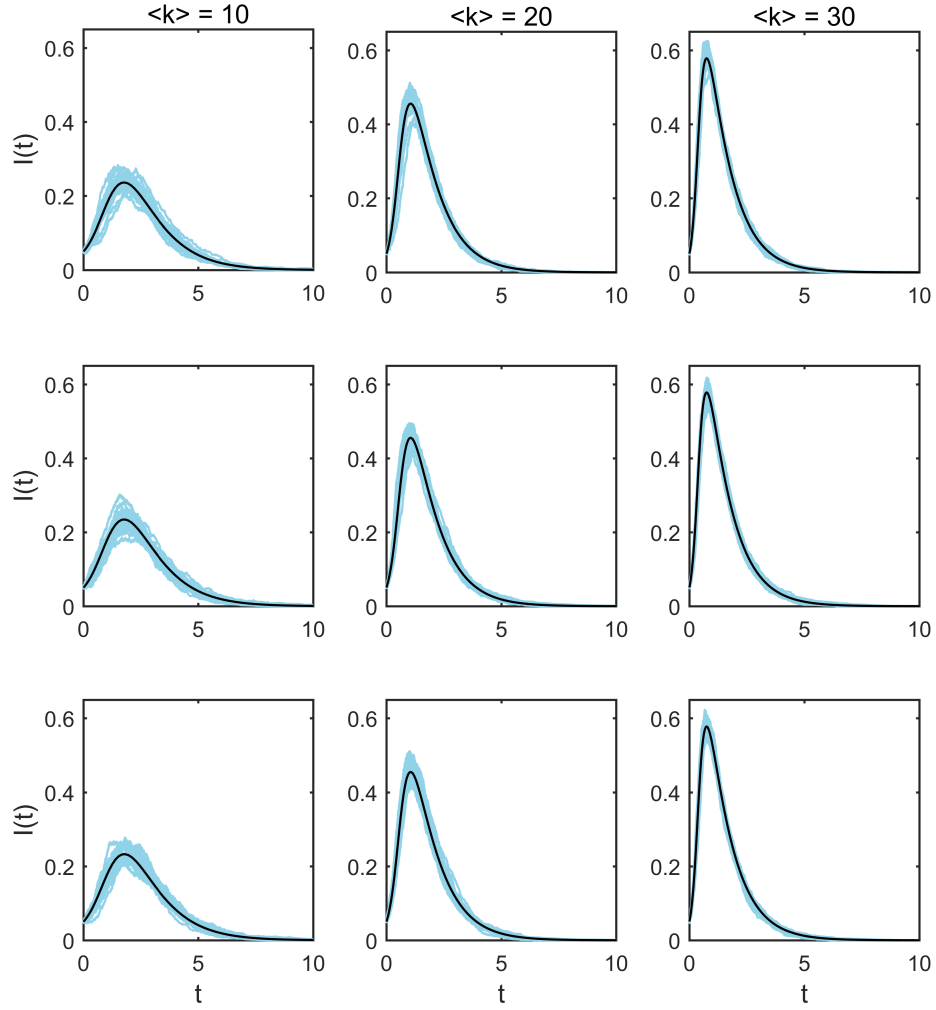


Figure 3.7: Multiplex model prediction vs. simulation — varying clustering and average degree. Plotting the dynamics of the proportion of infected individuals over time. Each panel contains 25 Gillespie simulations on a single multiplex network comprised of $N = 1000$ individuals (blue lines) and the associated EBCM prediction (black line). All networks are generated using a negative binomial distribution for pairs of edge stubs with parameters $p = 0.5$ and various values for r . Networks in column 1 (counting from left to right) have average degree 10 (achieved via $r = 5$), networks in column 2 have average degree 20 (achieved via $r = 10$) and networks in column 3 have average degree 30 (achieved via $r = 15$). Networks in row 1 (counting from top to bottom) have minimised clustering via values $p_s = 0.99999998$ and $p_t = 10^{-8}$. Networks in row 2 have the values $p_s = 0.49999999 = p_t$. Networks in row 3 have maximised clustering via the values $p_s = 10^{-8}$ and $p_t = 0.99999998$. Counting panels from left to right and top to bottom, static networks have the following clustering coefficients: $C = 0.0161$, $C = 0.0267$, $C = 0.0370$, $C = 0.0535$, $C = 0.0473$, $C = 0.0493$, $C = 0.0898$, $C = 0.0662$, $C = 0.0629$. In all panels, $tmax = 10$, $\rho = 0.05$, $\beta_s = \beta_d = 0.25$, $\gamma = 1$, $\eta = 0.01$

led to a slight increase in the speed at which the epidemic spread through the population. Increasing a single infection parameter β_s or β_d leads to an increase in the rate of epidemic

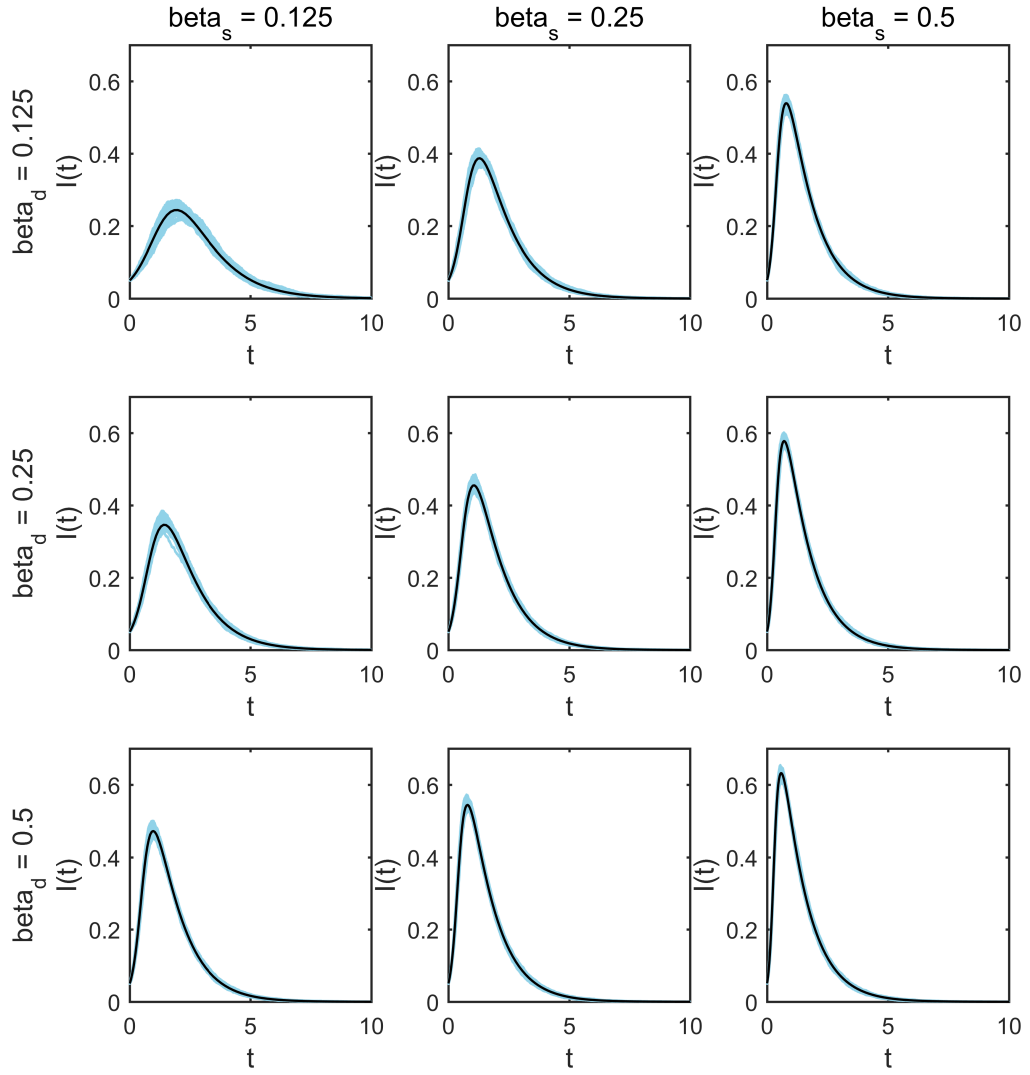


Figure 3.8: **Multiplex model prediction vs. simulation — varying infection parameters β_s and β_d .** Plotting the dynamics of the proportion of infected individuals over time. Each panel contains 100 Gillespie simulations (10 simulations on 10 multiplex networks comprised of $N = 5000$ individuals) (blue lines) and the associated EBCM prediction (black line). All multiplex networks follow a negative binomial distribution for pairs of edge stubs with parameters $p = 0.5$ and $r = 10$, which were split into three edge types via $p_s = 0.3 = p_t$ and thus $p_d = 0.4$. In all panels $tmax = 10$, $\rho = 0.05$, $\gamma = 1$, $\eta = 0.01$. Across the panels, different values for β_s and β_d have been used in the range $[0.125, 0.25, 0.5]$, indicated by individual column and row headings

spread. Altering the parameter ρ means changing the number of individuals who are infectious at the start of an epidemic process. Increasing the value of ρ leads to changes in the shape of the curve $I(t)$, describing the prevalence of infection at time t , and to the epidemic process finishing sooner. Altering the values p_s , p_t and p_d , with the constraint $(p_s + p_t + p_d) \equiv 1$, demonstrates the range of dynamics that can be achieved using a fixed

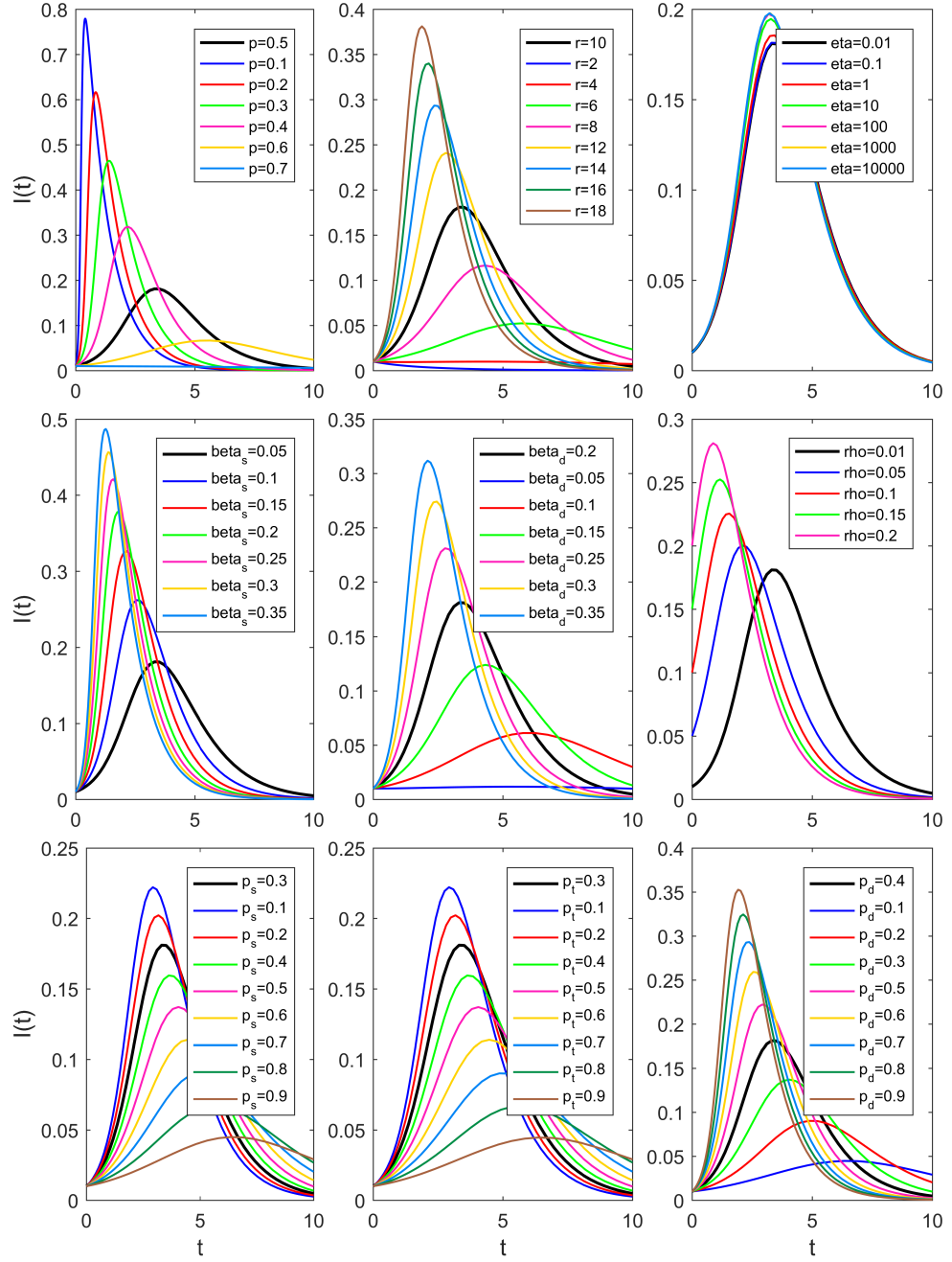


Figure 3.9: Multiplex model predictions. Plotting the dynamics of the proportion of infected individuals over time, for a number of different parameter sets. In all panels, a baseline parameter set ($p = 0.5$, $r = 10$, $p_s = 0.3 = p_t$, $p_d = 0.4$, $\beta_s = 0.05$, $\beta_d = 0.2$, $\gamma = 1$, $\eta = 0.01 = \rho$, $tmax = 10 \Rightarrow R_0 = 1.076$) is used to plot dynamics predicted by multiplex model equations (3.1)-(3.23) (thick black line). In each panel, a single parameter is varied and the resultant predictions are plotted in various colours, indicated by individual panel legends. In the bottom row of panels, parameters p_s , p_t and p_d are being varied. Since the model has the constraint $(p_s + p_t + p_d) \equiv 1$, we alter the triplet values in each panel in the following way. Assume we are varying the parameter p_s . If the new p_s is larger than the baseline p_s , we subtract $\frac{1}{2}$ the difference from the remaining baseline parameters p_t and p_d . Conversely, if the new p_s is smaller than the baseline p_s , $\frac{1}{2}$ the difference is added to each of the values p_t and p_d .

distribution for pairs of edge stubs with additional parameters to distribute edge pairs into three edge types. Baseline infection parameters are used across all three panels, thus $\beta_s = 0.05 < 0.2 = \beta_d$, meaning that an increase in the proportion of dynamic edges leads to an increase in the speed of the epidemic, whilst any increase in the proportion of static edges leads to a decrease in the rate of epidemic spread.

3.3.4 Contribution of network layers via $(p_s + p_t + p_d) \equiv 1$

When degree distributions are interdependent, the parameters $(p_s + p_t + p_d) \equiv 1$ afford the ability to investigate the effects on epidemic dynamics of altering the proportion of edges of each type. Previously, we observed changes in the dynamics of $I(t)$, caused by altering the contributions of each edge type (Figure 3.9), where $\beta_d > \beta_s$, rewiring was slow, and pairs of edge stubs were governed by a negative binomial distribution.

In this multiplex setting, increasing the force of infection on one network layer effectively reduces the force of infection on remaining network layers. Thus the value of parameters β_s , β_d and η , and the ratios between them, bias the effect of varying model parameters p_s , p_t and p_d . To take this into account, we allowed parameters β_s , β_d and η to take three distinct values (specifically $\beta_s \in [0.55, 0.6, 0.65]$, $\beta_d \in [\frac{\beta_s}{2}, \beta_s, 2\beta_s]$ and $\eta \in [0.01, 1, 100]$), and we considered all 27 combinations of their values, before varying the contributions of each edge type and recording the final epidemic size predicted by equations (3.1)-(3.23) in each case (Figure 3.10). This approach enabled isolation of the effects of changing single infection or rewiring parameters and exploration of the contributions made by various combinations of edge proportions p_s , p_t and p_d in distinct parameter settings.

Increasing the proportion of triangle corners via p_t consistently led to decreases in final epidemic size, suggesting that clustering slows the epidemic process regardless of the choice of parameters β_s , β_d and η (Figure 3.10). Generally, increasing the value of η resulted in an increase in final epidemic size when comparing identical edge contributions. Likewise, increasing the value of infection parameters β_s or β_d led to an increase in final epidemic size. Dependant on the combination of parameters β_s , β_d and η , different behavioural regimes emerge, indicated by the orientation of colours and the direction in which they change in individual panels. We observe that a single edge proportion can have a more or less dominant effect on the outcome, dependent on the particular parameter set. For example, when $\eta = 0.01$ and $\beta_s = 0.55 = \beta_d$, changing the proportion of dynamic edges p_d has little effect on the final epidemic size. However, when $\eta = 100$, $\beta_s = 0.65$ and

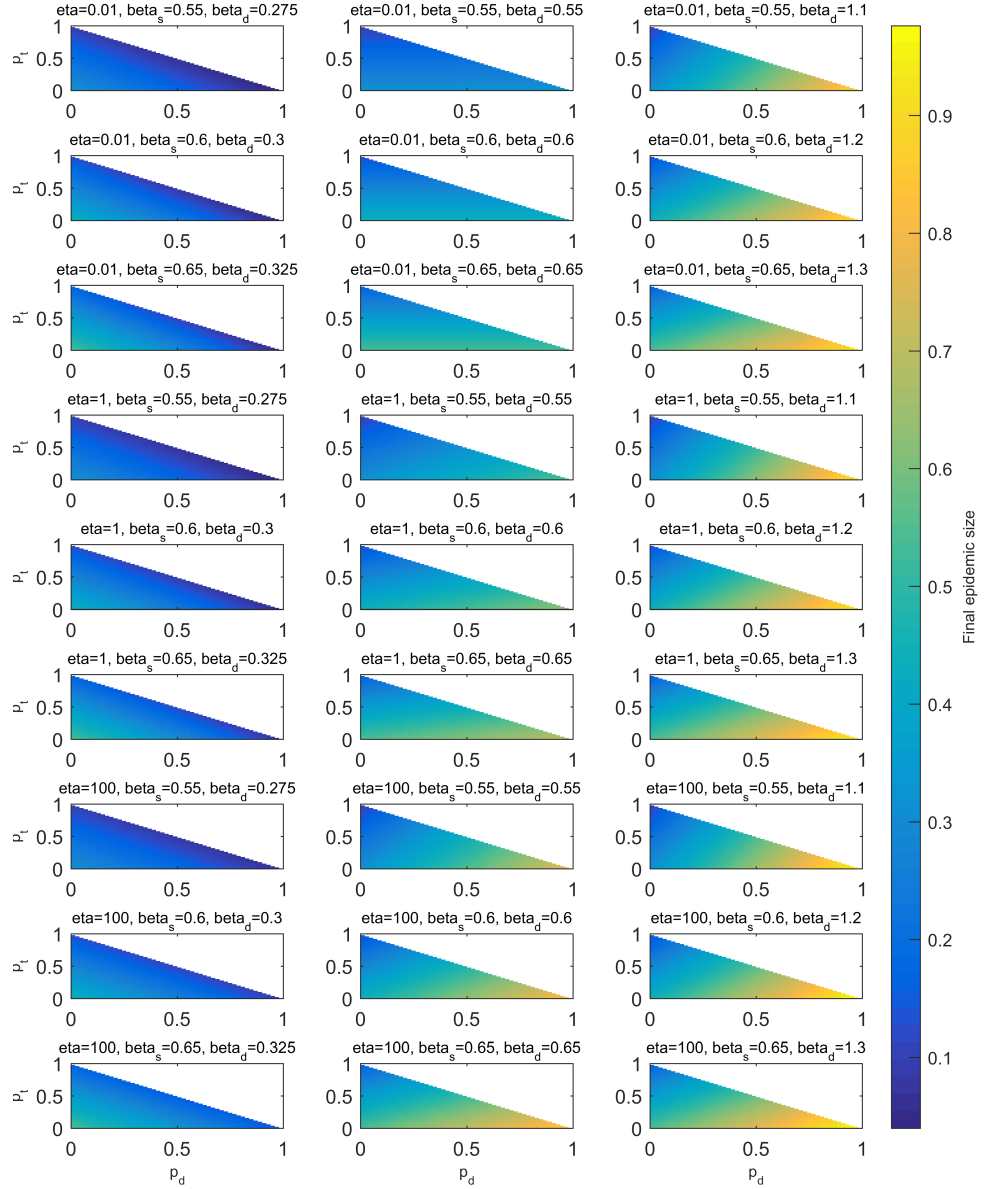


Figure 3.10: **Multiplex model layer contributions.** Heat map plots depicting the final epidemic size (equal to the fraction of the population who are either infectious or recovered at the end of the epidemic process) predicted by equations (3.1)-(3.23) for a multiplex network of various proportions p_s , p_t (y -axes) and p_d (x -axes), with the model constraint $(p_s + p_t + p_d) \equiv 1$. For all setups $\gamma = 1$, $\rho = 0.01$, $tmax = 25$ and pairs of edge stubs followed a discrete homogeneous distribution where all individuals had 2 edge pairs (and hence total degree 4). The values of remaining model parameters η , β_s and β_d are indicated above each panel, with $\eta \in [0.01, 1, 100]$, $\beta_s \in [0.55, 0.6, 0.65]$ and $\beta_d \in [\beta_s/2, \beta_s, 2\beta_s]$. All 27 possible combinations of the parameters η , β_s and β_d are considered. Prior to implementation, a number of setups across the (p_s, p_t, p_d) parameter spaces in each panel were tested by hand to ensure that the epidemic process had concluded by time $tmax = 25$

$\beta_d = 1.3$, altering the parameter p_d leads to more extreme changes in final epidemic size, a result of β_d dominating β_s and an increased rate of dynamic edge rewiring.

3.3.5 Validation of basic reproduction number R_0

The next generation matrix \mathbf{G} (3.24) and the value R_0 can be validated by testing to see if the final epidemic size is disturbed as R_0 exceeds the epidemic threshold ($R_0 = 1$). When the basic reproduction number is sub-threshold ($R_0 < 1$), the associated epidemic process is expected to ‘die-out’. However, when $R_0 > 1$ the epidemic is expected to take hold and spread within a population.

For a number of setups, we recorded the final epidemic size predicted by equations (3.1)-(3.23), the final epidemic size of a single Gillespie simulation of the same process, and the associated R_0 value (Figure 3.11). To obtain a suitable range of R_0 values we systematically increased $\beta_s = \beta_d$ from sub-threshold values, while all other parameters were held constant. Independent binomial distributions were used for static line stubs, static triangle corners, and dynamic line stubs. In Gillespie simulations where $R_0 > 1$, we imposed an additional constraint requiring the number of infectives to reach at least ten times the initial number of infected individuals, otherwise a new Gillespie simulation was implemented. As R_0 exceeded the epidemic threshold, the final epidemic size predicted by model equations (3.1)-(3.23) and from individual simulations increased rapidly, suggesting the derivation of the next generation matrix \mathbf{G} and associated R_0 is rigorous.

We plotted R_0 and the associated final epidemic size predicted by equations (3.1)-(3.23) for a number of scenarios to investigate the impact on their values of varying specific multiplex network attributes (rewiring, clustering and average degree), and to explore the relationship between R_0 and final epidemic size (Figure 3.12). Varying the rewiring rate η demonstrates that R_0 and the associated final epidemic size increase with the value of η . Varying η can also move the system below or above the epidemic threshold $R_0 = 1$. However, there is a limit to this relationship; as η increases above 20, the changes in R_0 and final epidemic size are negligible. We have seen previously that larger values of p_t result in smaller final epidemic sizes, suggesting that increased clustering slows epidemic processes on multiplex networks (Figure 3.10). Here, we find that increasing p_t leads to decreases in both R_0 and the associated final epidemic size (Figure 3.12). The relationship between p_t and final epidemic size appears to be linear. For smaller p_t the curve with R_0 appears to be linear, but as p_t tends towards its maximal value, the reduction in R_0 increases.

An increase in average degree $\langle k \rangle$, where pairs of edge stubs follow a negative binomial

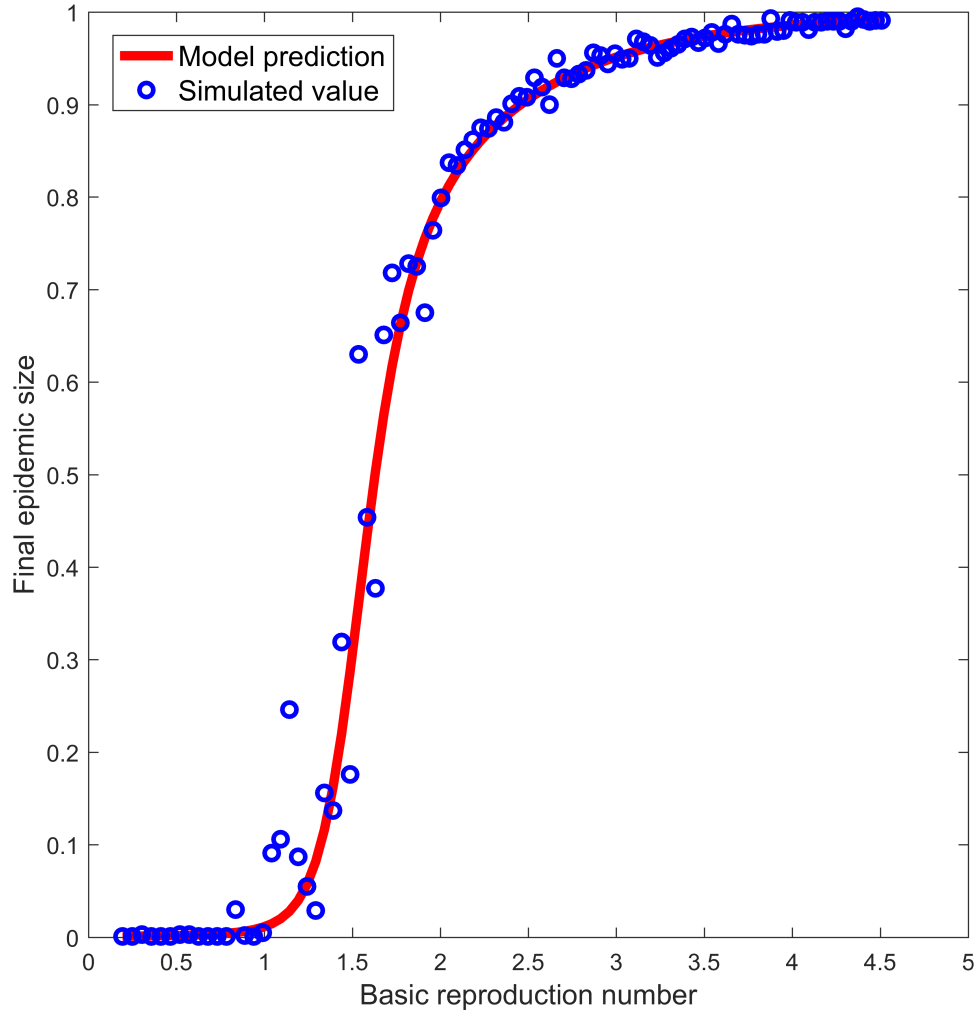


Figure 3.11: **Validation of the basic reproduction number R_0 .** Plotting values of the basic reproduction number R_0 (x -axis), found via the leading eigenvalue of the matrix (3.24), against the associated final epidemic sizes (y -axis) predicted by multiplex equations (3.1)-(3.23) (red line) and recorded by single statistically-correct Gillespie simulations (blue circles). Static and dynamic line stubs follow binomial distributions with parameters $n = 20$ and $p = 0.5$. The distribution of triangle corners follows a binomial distribution with parameters $n = 1$ and $p = 0.001$ to minimise clustering. Fixed parameters were $\gamma = 1$, $\rho = 0.001$, $\eta = 0.01$, $tmax = 10$, $N = 1000$. In each setup $\beta_s = \beta_d$. 100 transmission rates were tested, from $\beta_s = \beta_d = 0.01$ up to $\beta_s = \beta_d = 0.3$, in equal-sized increments. In Gillespie simulations where $R_0 > 1$, if the number of infected individuals did not reach 10 times the initial number of infectives, all data was discarded and the Gillespie script restarted from initial conditions at time zero

distribution, led to increases in R_0 and final epidemic size (Figure 3.12). The relationship between $\langle k \rangle$ (negative binomial) and R_0 appears to be linear. However, the relationship between $\langle k \rangle$ and final epidemic size differs. The final epidemic size increases at a faster rate above some critical average degree, say $\langle k \rangle = 12$. A similar pattern emerges in

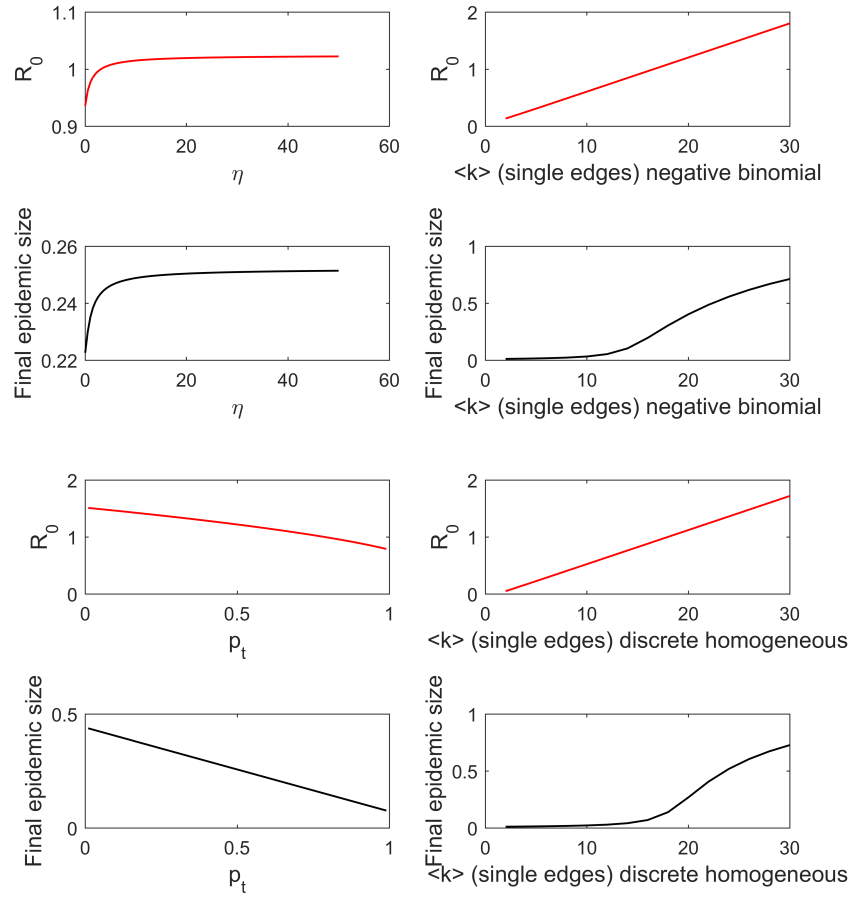


Figure 3.12: **Effects of rewiring, average degrees and clustering.** Plotting the value of R_0 and the associated final epidemic size found using EBCM equations (3.1)-(3.23), for a number of different setups. Upper-left panels: Testing 100 evenly-spaced values for η in the range $[0.01, 50]$. Remaining model parameters were $p_s = 0.3 = p_t$, $\beta_s = 0.1 = \beta_d$, $\gamma = 1$, $\rho = 0.01$ and $tmax = 25$. Pairs of edge stubs followed a negative binomial distribution with parameters $p = 0.5$ and $r = 5$. Upper-right panels: Testing 15 evenly-spaced values for $\langle k \rangle \in [2, 30]$, generated using a negative binomial distribution for pairs of edge stubs with fixed $p = 0.5$ and $r \in [1, 15]$. Remaining model parameters were $p_s = 0.3 = p_t$, $\beta_s = 0.0625 = \beta_d$, $\gamma = 1$, $\eta = 0.1$, $\rho = 0.01$, $tmax = 25$. Lower-left panels: Testing 100 evenly-spaced values for p_t in the range $[0.01, 0.99]$. The proportion $(1 - p_t)$ was split equally between parameters p_s and p_d . Remaining model parameters were $\beta_s = 0.5 = \beta_d$, $\gamma = 1$, $\rho = 0.01$, $\eta = 0.1$ and $tmax = 25$. Pairs of edge stubs followed a discrete homogeneous distribution where all individuals had 2 edge pairs. Lower-right panels: Testing 15 evenly-spaced values for $\langle k \rangle \in [2, 30]$, generated using a discrete homogeneous distribution for pairs of edge stubs where all individuals have identical degree. Remaining model parameters were $p_s = 0.3 = p_t$, $\beta_s = 0.0625 = \beta_d$, $\gamma = 1$, $\rho = 0.01$, $\eta = 0.1$, $tmax = 25$

the relationship between the average degree, R_0 and final epidemic size when pairs of edge stubs follow a discrete homogeneous distribution. This is not surprising, as we

saw previously that the relationship between R_0 and final epidemic size is non-linear (Figure 3.11). However, these results show that small average degrees make it hard for the epidemic to take hold in the population. Potentially, this is a result of the multiplex network becoming divided into more than one connected component, meaning the disease can get trapped within smaller sub-populations of individuals, limiting its effect.

3.4 Discussion

We have proposed a model describing the time evolution of an SIR epidemic spreading through a population of individuals in a multiplex network consisting of two layers: a static network layer representing persistent human connections and a dynamic network layer representing temporary human interactions made outside of a typical household. The model incorporates heterogeneity in the structure, type and duration of connections between individuals and the number of model equations remains fixed regardless of population size. We designed the multiplex model to afford control of network transitivity (clustering), on the static layer only, by generating the associated network structure using a combination of 2-vertex and 3-vertex cliques, referred to here as static lines and triangles. The dynamic network layer was generated via a single distribution for 2-vertex cliques. Following the EBCM approach [74], we obtained expressions for time-evolving quantities of interest, such as the infectious proportion of the population $I(t)$. We have also applied the next generation matrix method [20] to compute the basic reproduction number R_0 , a measure of the expected number of infections a typical infectious individual will cause during an epidemic, in an otherwise susceptible population.

Multiplex model equations (3.1)-(3.23) were validated, first by testing convergence of epidemic dynamics to predictions made by existing uniplex edge-based compartmental model equations, when either network layer (static or dynamic) was eliminated, and second by comparing full model (with static and dynamic elements) predictions to the dynamics of corresponding statistically-correct Gillespie simulations [32].

The multiplex model's parameter space was explored by varying individual parameters and plotting the resulting epidemic dynamics, and by mapping the outcome on final epidemic size of having various proportions of each edge type when considering different combinations of model parameters β_s , β_d and η . The basic reproduction number R_0 , found via the leading eigenvalue of the next generation matrix \mathbf{G} (3.24), was validated by demonstrating that continually incrementing infection parameters β_s and β_d , with all else held constant, led to a rapid increase in final epidemic size as R_0 exceeded its epidemic

threshold. Finally, we explored the effect on R_0 and the associated final epidemic size predicted by equations (3.1)-(3.23) of altering specific multiplex network attributes governing the rate of rewiring, the extent of clustering and the average degree.

Our unique contribution towards the literature is a model with a combination of static *and* dynamic network elements, derived by combining the EBCM approach to modelling an SIR epidemic on a static network with tunable clustering [125] with the EBCM approach to modelling an SIR epidemic on a dynamic fixed-degree network [77], under the framework of a dual-layer multiplex network.

The EBCM approach allows us to model variations in contact structure, contact type, and contact duration simultaneously. Modelling such heterogeneities via EBCM provides an opportunity to investigate the effects of heterogeneities observed in real-world networks [91, 58, 121], alongside consideration of common network attributes such as clustering and degree distributions. EBCM also affords a huge reduction in the number of equations required to track the epidemic, compared with full simulation.

This work progresses the drive to derive population models that capture reasonable levels of complexity and heterogeneity whilst exhibiting a tractable number of equations. By providing a clear and concise ‘walkthrough’ to deriving and validating our desired model, we hope that future researchers are inspired to build on these results by designing and implementing novel models, modelling approaches, and computational algorithms.

The work here extends previous research following the edge-based compartmental modelling approach. Prior EBCM approaches derived model equations describing the SIR epidemic process on wholly static or wholly dynamic uniplex networks. For example, EBCM has been utilised to describe the SIR epidemic on static actual-degree configuration model (CM) networks [77], static CM networks with tunable clustering [125], and static expected degree mixed Poisson (MP) networks [77].

Dynamic uniplex networks have also been considered via the EBCM approach. Namely, CM networks with mean-field social heterogeneity (edges are broken and rewired at a very fast rate, meaning all pairs of individuals contact each other at the same rate, and edge durations are fleeting), dynamic fixed-degree CM networks (edges are rewired but edge durations are finite), dormant contact CM networks (existing edges are broken and remain dormant for some time, before being re-established), MP networks with mean-field social heterogeneity (fleeting edge duration), and dynamic variable-degree MP networks (finite edge duration) [77].

Existing modelling approaches incorporating heterogeneity include the consideration

of an epidemic with two ‘levels’ of mixing between individuals (but no network structure) [4], and the later considerations of epidemic processes occurring on structured populations with two levels of mixing [129], and with two routes of transmission [130]. Recently, the EBCM approach was used to derive equations describing an SIR epidemic process with non-sexual and sexual transmission routes, a characteristic of diseases such as Ebola and Zika [75].

Other modelling approaches have incorporated dynamicity of connections between individuals (and hence heterogeneity in contact duration) by, e.g., considering an SIR epidemic on a network with intermittent social distancing, where susceptible individuals break links with infectious individuals for some time t_b , after which the connection is re-established [115]. Another approach considered the effects of constrained rewiring during an SIS epidemic, whereby susceptible individuals cut links to infectious individuals regardless of distance, and rewire to a susceptible individual within a given radius, where the nodes of the network were embedded in Euclidean space [95].

Research considering the large graph limit of an SIR epidemic on a dynamic multi-layer network affords heterogeneity in contact type and in contact duration by allowing individual network layers to contain either activating or de-activating edges, and by allowing edges in different layers to correspond to different types of contacts [47]. Although [47] considers the SIR epidemic spreading on a multiplex network, including providing a dual-layer multiplex example where edge types correspond to community and healthcare contacts, they do not consider any fully static network components.

There are a number of adaptations that can be made to the proposed model. The model considers a heterogeneous contact structure between N individuals. However, the locations of N individuals are not taken into account. Real-world networks occur in space [6] and thus it is important to investigate the effects of considering node locations. In this study, we have chosen to disregard the spatial locations of individuals. A more realistic model of an SIR epidemic spreading on a multiplex network of individuals would be achieved by embedding the locations of each individual into Euclidean space. Even more complex models could consider dynamic node locations, or a combination of static and dynamic node locations.

Another potential adaptation is considering weighted network connections. In the proposed model, all connections are considered to be unweighted, or equivalently to share equal weight (homogeneity). The model could be adapted by, e.g., making the weight of each connection proportional to the Euclidean distance between the two node locations

(given spatial embedding), by imposing a distribution of connection weights, or by assigning weights at random. Then, the probability of contracting disease across a connection can be made proportional to the weight of that connection.

In the present model, the population of N individuals is fixed. We do not consider the effect of flux in or out of the population, e.g. by births, deaths or migration events. An important next step is to adapt the model presented here to consider in- and out-flow of members of the population, or at least to consider whether such in- and outflows significantly influence disease dynamics.

Another model limitation concerns the assumptions made surrounding edge rewire events on the dynamic network layer. Here, we assume that when one partnership ends, a new partnership forms immediately. Thus, given a non-zero degree on the dynamic network layer, individuals remain connected to strangers from the wider population (via dynamic network connections) at all times. In reality, the fleeting connections an individual makes with strangers are temporary, and individuals can remain disconnected from these connections for some time. An improvement to the model could thus be achieved by allowing for gaps to occur between partnerships by implementing the dormant contact approach on the dynamic network layer (e.g. see Section 3.3 of [77], [115], [105] and [113]). The immediate implication of such an approach is a more accurate model in relation to observed human behaviours. However, the dynamics of the epidemic process will be slowed, especially if the duration of the gap (in time) between partnerships is comparable to or longer than the typical time it takes to transmit infection to a partner. Alternative rules for edge dynamicity can also be considered, such as constrained rewiring [95] and edge activation and deletion [47, 102, 111]. Other model adaptations include allowing for tunable clustering on all network layers (and thus imposing two edge distributions on each network layer), implementing more complex distributions governing the degrees of each node and biasing initially infectious individuals instead of selecting them at random.

The multiplex model affords tunable clustering on the static network layer by generating its contact structure using a distribution of line stubs and a distribution of triangle corners. However, the configuration model wiring process requires that any two individuals share at most one connection within a single network layer. Double edges can occur across network layers (i.e. when the same edge is present in both network layers), but not within them. This constraint greatly reduces the possibilities for placing triangles suitably into the network, meaning the configuration process is slowed down and the extent of clustering that can be achieved is reduced. Greater control over clustering could be achieved

by adapting the model to allow for overlapping triangles (and either allowing double edges to occur in single network layers, or amalgamating any double edges that occur into single edges, or doubly-weighted edges).

Other than making adaptations to the proposed model, there are a number of tests and analyses which are beyond the scope of this work. Firstly, a comprehensive exploration of the entire parameter space would elucidate the behavioural ‘envelope’ of the model and uncover any parameter regions where the model poorly predicts the SIR epidemic process, compared with simulation. A more thorough understanding of the impact of degree and degree heterogeneity on the relationship between parameters and system behaviour will require consideration of additional edge distributions with various levels of heterogeneity and average degrees. Secondly, the model’s utility can be investigated by using real-world data from historical epidemics or similar processes, e.g. livestock herd contact tracing data or Twitter data tracking the prevalence of a hashtag over time. Using real data, model parameters could be estimated using Bayesian estimation techniques and the resulting model predictions compared with prior knowledge of what occurred. The basic reproduction number R_0 can be tested in the same way.

This work considers an SIR compartmental model under the guise of a disease spreading through a networked population. Thought must be given to what other real-world processes can be well described by the SIR compartmental model, such as opinion formation, rumour spreading or uptake of fashion trends. Further, a two-layer multiplex like the proposed model could be used to investigate the dynamics of two *interacting* SIR-type processes, such as a physical disease spreading process occurring on one network layer in combination with a disease awareness process occurring on the opposing network layer, using similar approaches to those of [29] and [61].

Future research can build on these observations by considering similar modelling approaches that account for compartmental models other than the SIR-type. For example, the SIS model (describing infections that do not confer lasting immunity, such as the common cold) and the SEIR model (describing infections with incubation periods, where individuals have contracted a disease but are not yet infectious and hence are in the ‘exposed’ disease state) are not considered here. Modelling an SEIR infection may require simple adaptation of the existing EBCM approach. However, consideration of an SIS-type epidemic process requires an altogether new modelling approach. A key assumption of the present approach is the consideration of all neighbours of the test node u as being independent. Attempting to impose this assumption would prevent modelling of SIS dynamics, a

consequence which is discussed in [76] and [77].

Experiments that can be performed to improve and inform future modelling approaches include: quantifying the levels of heterogeneity in existing populations, including behavioural and structural heterogeneity, gaining a deeper understanding of the biological processes underlying disease spreading processes, improving on existing algorithmic and analytic approaches, and fostering closer relations between modellers and practitioners, in order to maximise the benefits arising from research.

3.5 Acknowledgements

Rosanna C Barnard acknowledges funding from the Engineering and Physical Sciences Research Council, EP/M506667/1. Joel C Miller was funded by the Global Good Fund through the Institute for Disease Modeling.

Chapter 4

Epidemic threshold in pairwise models for clustered networks: closures and fast correlations

4.1 Introduction

Epidemic dynamics on networks, being susceptible-infected-susceptible (SIS), susceptible-infected-recovered/removed (SIR) or otherwise, are often modelled as continuous time Markov chains with discrete but extremely large state spaces of order m^N , where m is the number of different disease statuses (e.g. $m = 2$ for SIS and $m = 3$ for SIR) and N is the number of nodes/individuals in the network. This makes the analysis of the resulting exact system almost impossible, except for some specific network topologies such as the fully connected network, networks with considerable structural symmetry or networks with few nodes [57, 44] that allow for simplification.

This problem, instead, has been dealt with by focusing on mean-field models where the goal is to derive, often heuristically, a system of ordinary or integro-differential equations that describe (non-Markovian) epidemics for some average quantities, such as the expected number of nodes in various states, the expected number of links in various states or the expected number of star-like structures (focusing on a node and all of its neighbours). These methods usually rely on closures to break the dependency on higher-order moments (e.g. the expected number of nodes in a state depends on the expected number of links in certain states and so on). Such an approach has led to a number of models including heterogeneous or degree-based mean-field [89, 88], pairwise [94, 54], effective-degree [62], edge-based compartmental [77] and message passing [51], to name a few. These models

essentially differ in the choice of variables over which the averaging is done. Perhaps the most compact model with the fewest number of equations is the edge-based compartmental model [78] and this is valid for heterogeneous networks with Markovian SIR epidemics, although extensions of this model for arbitrary infection and recovery processes are also possible [104].

Pairwise models have been extremely popular and the very first model for regular networks and SIR epidemics [94, 54] has been generalised to heterogeneous networks [23], preferentially mixing networks [23], directed [103] and weighted networks [96], adaptive networks [37, 56, 109], and structured networks [45] among others. Perhaps this is due to the relative simplicity and transparency of the pairwise model, whereby variables have a straightforward interpretation and a basic understanding of the network and epidemic dynamics coupled with good bookkeeping leads to valid and analytically tractable model equations. Pairwise models have been successfully used to derive analytically the epidemic threshold and final epidemic size, with these results mostly limited to networks without clustering. The propensity of contacts to cluster, i.e. that two friends of an individual/node are also friends of each other, is known to lead to many complications, and modelling epidemics on clustered networks using analytically tractable mean-field models is still limited to networks with very specific structural features [45, 85, 71, 72, 52, 125, 98]. However, using approaches borrowed from percolation theory [72] and focusing more on the stochastic process itself [112], some results have been obtained. For example, in [72] it was shown that for the susceptible-infected-recovered (SIR) epidemic on clustered networks with heterogeneous degree distributions, the basic reproduction number is given by

$$R_0 = \frac{\langle k^2 - k \rangle}{\langle k \rangle} T - \frac{2\langle n_\Delta \rangle}{\langle k \rangle} T^2 + \dots, \quad (4.1)$$

where $\langle k^i \rangle$ stands for the i th moment of the degree distribution, T is the probability of infection spreading across a link connecting an infected to a susceptible node and $\langle n_\Delta \rangle$ denotes the average number of triangles that a node belongs to. The first positive term in (4.1) corresponds to the threshold for configuration-type networks without clustering. The second term, which is negative, shows that clustering reduces the epidemic threshold when compared to the unclustered case, the contribution of the remaining terms being of a smaller order.

For pairwise models, clustering first manifests itself by requiring a different and more complex closure, which makes the analysis of the resulting system, even for regular networks and SIR dynamics, challenging. Furthermore, it turns out that such a closure may

in fact fail to conserve pair-level relations and may not accurately reflect the early growth of quantities such as closed loops of three with all nodes being infected [46]. Such considerations have led to an improved closure being developed in an effort to keep as many true features of the exact epidemic process as possible [46]. In this chapter we focus on the classic pairwise model for regular networks with clustering, using both the simplest closure and a variant of the improved closure. We show that by working with two fast variables corresponding to correlations between neighbouring nodes during the epidemic, we can determine the epidemic threshold analytically as an asymptotic expansion in terms of the global clustering coefficient ϕ , defined in Section 4.2.1.

The use of fast variables is not completely new and has been used in [54] and [22], but the epidemic threshold has only been obtained numerically and it was framed in terms of a growth-rate-based threshold which is equivalent to the basic reproduction number at the critical point of the epidemic spread. In [22] a hybrid pairwise model incorporating random and clustered contacts is considered, with the analysis focused on the growth-rate-based threshold. The authors of [22] managed to derive a number of results, some analytic (the critical clustering coefficient for which an epidemic can take off) and some semi-analytic, and have shown, in agreement with most studies, that clustering inhibits the spread of the epidemic when compared to an equivalent network without clustering but with equivalent parameter values governing the epidemic process. However, no analytic expression for the threshold was provided.

More recently, in [60], the epidemic threshold in a pairwise model for clustered networks with closures based on the number of links in a motif, rather than nodes, was calculated as

$$R_0 = \frac{(n-1)\tau}{\tau + \gamma + \tau\phi}, \quad (4.2)$$

where n is the average number of links per node, ϕ is the global clustering coefficient and τ and γ are the infection and recovery rates, respectively. The expression above can be expanded in terms of ϕ to give

$$R_0 = \frac{(n-1)\tau}{\tau + \gamma} \left(\frac{1}{1 + \phi \frac{\tau}{\tau + \gamma}} \right) \simeq \frac{(n-1)\tau}{\tau + \gamma} \left(1 - \phi \frac{\tau}{\tau + \gamma} + \dots \right), \quad (4.3)$$

which again demonstrates that clustering reduces the epidemic threshold.

Building on these results, and effectively extending the work in [54, 22], our work presents a method to determine the epidemic threshold analytically and applies it in the context of pairwise models with two different closures for clustered networks. The

chapter is structured as follows. In Section 4.2 we outline the model with closures for unclustered and clustered networks discussed in Section 4.3. In Section 4.4 we briefly review existing results and approaches for the pairwise model with the simple closure and then focus on the correlation structure in terms of fast variables, showing that the epidemic threshold can be expressed via the solution of a cubic polynomial. This key solution is determined numerically and analytically as an asymptotic expansion in terms of the clustering coefficient. In Section 4.5 we show that our approach can be extended to consider a compact version of the improved closure, thus validating and generalising our approach. Finally we conclude with a discussion of the results, including comparing the threshold to other known results and touching upon a number of possible extensions.

4.2 Model formulation

4.2.1 The network

We begin by considering a population of N individuals with its contact structure described by an undirected network with adjacency matrix $G = (g_{ij})_{i,j=1,2,\dots,N}$ where $g_{ij} = 1$ if nodes i and j are connected and zero otherwise. Self-loops are excluded, so $g_{ii} = 0$ and $g_{ij} = g_{ji}$ for all $i, j = 1, 2, \dots, N$. The network is static and regular, such that each individual has exactly n edges or links. The sum over all elements of G is defined as $\|G\| = \sum_{i,j} g_{ij}$. Hence, the number of doubly counted links in the network is $\|G\| = nN$. More importantly, using simple matrix operations on G , we can calculate the global clustering coefficient of the network

$$\phi = \frac{\text{trace}(G^3)}{\|G^2\| - \text{trace}(G^2)}, \quad (4.4)$$

where $\text{trace}(G^3)$ yields six times the number of closed triples or loops of length three (uniquely counted) and $\|G^2\| - \text{trace}(G^2)$ is twice the number of triples (open and closed, also uniquely counted).

4.2.2 SIR dynamics

The standard SIR epidemic dynamics are considered on the network defined in Section 4.2.1. The dynamics are driven by two processes: (a) infection and (b) recovery from infection. Infection can spread from an infected/infectious node to any of its susceptible neighbours and this is modelled as a Poisson point process with per-link infection rate τ . Infectious nodes recover from infection at constant rate γ .

4.2.3 The unclosed pairwise model

Let A_i equal 1 if the individual at node i is of type A and equal zero otherwise. Then single nodes (singles) of type A can be counted as $[A] = \sum_i A_i$, pairs of nodes (pairs) of type $A - B$ can be counted as $[AB] = \sum_{i,j} A_i B_j g_{ij}$ and triples of nodes (triples) of type $A - B - C$ can be counted as $[ABC] = \sum_{i,j,k} A_i B_j C_k g_{ij} g_{jk}$. This method of counting means that pairs are counted once in each direction, so $[AB] = [BA]$, and $[AA]$ is even. Using this notation to keep track of singles, pairs and triples leads to the following system of pairwise equations describing the SIR epidemic process on networks:

$$[\dot{S}] = -\tau[SI], \quad (4.5)$$

$$[\dot{I}] = \tau[SI] - \gamma[I], \quad (4.6)$$

$$[\dot{SI}] = \tau([SSI] - [ISI] - [SI]) - \gamma[SI], \quad (4.7)$$

$$[\dot{SS}] = -2\tau[SSI], \quad (4.8)$$

$$[\dot{II}] = 2\tau([ISI] + [SI]) - 2\gamma[II]. \quad (4.9)$$

We note that equations (4.7)-(4.9) contain triples which are not defined within the entire system of equations (4.5)-(4.9). The flow between compartments and the associated rates of the SIR pairwise model are illustrated in Figure 4.1. To determine solutions of the system, we must find a way to account for these triples in terms of pairs and singles, a method referred to as *closing the system*.

4.3 Closures

A quick inspection of the unclosed pairwise system (4.5)-(4.9) reveals that only triples of type $[ASI]$ need closing, with $A \in \{S, I\}$. These triples, as well as triples of type $[RSI]$, are illustrated in Figure 4.2 for unclustered and clustered networks.

4.3.1 Closure for unclustered networks

First, we consider the situation depicted in Figure 4.2a. Several observations can be made. The expected number of $A - S$ type links is $[AS]$ and the total number of links emanating from susceptible nodes counted across the whole network is $n[S]$. Hence, the most straightforward approximation would be to assume that X_i , with $i = 1, 2, \dots, n-1$, are independent and identically Bernoulli distributed random variables with a probability of success being equal to $p_{A|S-I}^{uc} = \frac{[AS]}{n[S]}$, where $p_{A|S-I}^{uc}$ stands for the probability that a

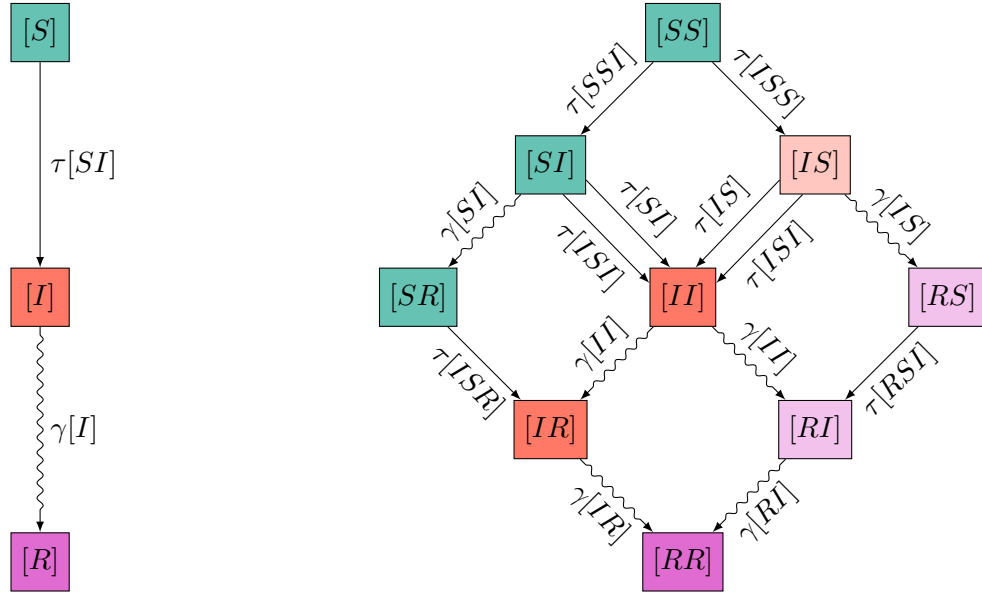


Figure 4.1: Flow diagrams showing the flux between compartments of singles (left) and compartments of pairs (right) in the SIR pairwise model. In the compartments of pairs, straight arrows denote infections coming from within the pair (with a rate depending on a pair) or from outside the pair (with a rate depending on a triple), and curved arrows denote a recovery. The colour indicates the status of the “first” node in the pair. Symmetry allows us to conclude that some of the variables (see lighter shaded variables on the right hand side of the pairs diagram) must equal their symmetric version (e.g. $[RS] = [SR]$), so we do not need to directly calculate both quantities.

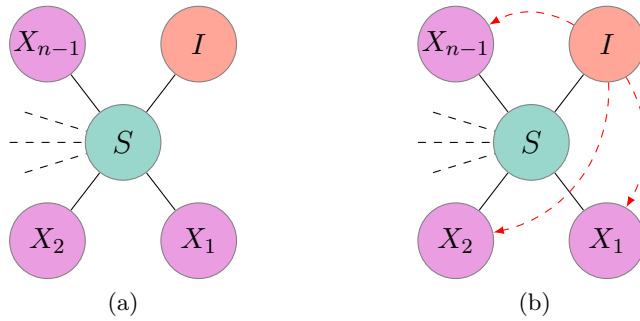


Figure 4.2: General setup for a central susceptible node with a given infected neighbour for (a) unclustered and (b) clustered regular networks with degree n . Dashed arrows indicate that the infected node may be connected to the other neighbours of the central susceptible node. Random variables X_1, X_2, \dots, X_{n-1} take values from the set $\{S, I, R\}$.

neighbour of a susceptible node already connected to an infected node will be in state A , provided that the network is unclustered. Averaging across the whole network leads to the closure

$$[AST] = [SI](n-1)p_{A|S-I}^{uc} = \frac{n-1}{n} \frac{[AS][SI]}{[S]}. \quad (4.10)$$

It is important to note that the new, closed system, obtained upon using equation (4.10) in the exact pairwise model (4.5)-(4.9), is effectively an approximation of the exact pairwise model (4.5)-(4.9) and one should question if the closure (4.10) conserves the properties of the stochastic process and of the counting on the network. For example, it is expected that in the closed system the number of nodes is conserved, i.e. $[S] + [I] + [R] = N$. Furthermore, the number of pairs of different types must sum to nN . More subtle conditions refer to the conservation of link types at node level ($[SS] + [SI] + [SR] = n[S]$) and pair level ($[SSI] + [ISI] + [RSI] = (n-1)[SI]$), respectively. It turns out that the closure for unclustered networks (4.10) conserves these relations [57]. Finally, the validity of closures can be empirically assessed by looking at the initial growth rate of the number of open and closed triples, where the number of open triples comprised of three infectious nodes should grow differently to the number of such closed triples. Of course such subtle tests are usually preceded by direct comparisons between the numerical solution of the closed pairwise system and explicit stochastic network simulations for a range of parameters. Such tests initially focus on prevalence of infection and final epidemic size but may include expected number of pairs.

4.3.2 Closure for clustered networks

Simple closure

The presence of closed loops of length three, as illustrated in Figure 4.2b, introduces some complications. Namely, a neighbour of the central susceptible node that is itself connected to an infected neighbour of the central node is less likely to be susceptible due to the added pressure from the infected neighbour, when compared to the case when the force of infection is distributed evenly, as is the case for the closure for unclustered networks (4.10). More precisely, the epidemic process on the network displays clear correlations. In [14] it has been shown that the exact SIS and SIR epidemics on networks are non-negatively correlated in the sense that $\mathbf{P}(I_i I_j) \geq \mathbf{P}(I_i) \mathbf{P}(I_j)$. Here, $\mathbf{P}(I_i I_j)$ represents the probability that nodes i and j , connected by a link, are both infected, while $\mathbf{P}(I_i)$ stands for the probability of node i being infected. For this result to hold, all processes must be Markovian and infection rates across all links and recovery rates of all nodes have

to be fixed a priori. Using the pairwise model for an *SIS* epidemic on an unclustered network with closure (4.10), it has been shown that the same correlation is preserved when averaging at the population level [57]. While the proof has not been extended to the pairwise *SIR* model, intuitively we expect to find the same correlation structure. Based on these observations, we assume that the correlation structure in exact *SIS* and *SIR* epidemics on networks averaged at the population level is maintained. Hence, the inequalities

$$[SI] \leq n[S] \frac{[I]}{N}, \quad [II] \geq n[I] \frac{[I]}{N}, \quad \text{and} \quad [SS] \geq n[S] \frac{[S]}{N}, \quad (4.11)$$

hold, where $[AB]$ and $[A]$ with $A, B \in \{S, I\}$ represent the expected counts of pairs and singles of the corresponding types taken from the exact model, i.e., the continuous time full Markov chain.

Intuitively, this means that as the epidemic spreads on the network, infected nodes are more likely to have neighbours which are themselves infected (either those that infected the node or were infected by it), and at the ‘front’ of the epidemic we would expect to observe a ‘sea’ of susceptible nodes alongside a ‘front’ of links between susceptible and infected nodes that drives the epidemic. Hence, clustering and correlations need to be accounted for and a new $p_{A|S-I}^c$ for clustered networks needs to be defined. This has been done in [54] and relies on a correlation factor, C_{AB} , that is able to capture the propensity that two nodes connected by a link are in states A and B , respectively. This is given by

$$C_{AB} = \frac{[AB]}{n[A] \frac{[B]}{N}}, \quad (4.12)$$

where $A, B \in \{S, I\}$. This effectively compares the expected number of edges of type $[AB]$ to what its value would be if nodes were labelled at random with $[A]$ nodes of type A and $[B]$ nodes of type B . If $C_{AB} > 1$, then nodes of type A and B are positively correlated, whereas if nodes of type A and B are negatively correlated, $C_{AB} < 1$. As expected, $C_{AB} = 1$ means that nodes are effectively labelled as type A or B at random. Equation (4.11) implies that

$$C_{SI} \leq 1, \quad C_{II} \geq 1 \quad \text{and} \quad C_{SS} \geq 1. \quad (4.13)$$

We can modify $p_{A|S-I}^{uc} = \frac{[AS]}{n[S]}$ to reflect these observations, leading to $p_{A|S-I}^c = \frac{[AS]}{n[S]} C_{AI}$. However, before the closure can be expressed, open and closed loops need to be treated separately. In order to do this, we split the closure based on whether the neighbour whose state is to be determined is part of a closed loop of three nodes and thus in direct contact

with an infectious node, or not. This leads to

$$p_{A|S-I}^c = \begin{cases} p_{A|S-I}^{uc} & \text{with probability } (1 - \phi), \\ p_{A|S-I}^{uc} C_{AI} & \text{with probability } \phi, \end{cases} \quad (4.14)$$

where ϕ is defined in equation (4.4). With this in mind, the closure can be derived by averaging equation (4.10) over the unclustered and clustered parts of the network. This leads to

$$[AST] = (1 - \phi)(n - 1)[SI]p_{A|S-I}^{uc} + \phi(n - 1)[SI]p_{A|S-I}^{uc} C_{AI} \quad (4.15)$$

$$= \frac{(n - 1)}{n} \frac{[AS][SI]}{[S]} \left((1 - \phi) + \phi \frac{N[AI]}{n[A][I]} \right). \quad (4.16)$$

Framing $p_{A|S-I}^{uc}$ and $p_{A|S-I}^c$ more generally and independently of the network type, i.e. simply considering p_A , the following statement holds:

Proposition 1. *Consider a closure of the following form $[AST] = (n - 1)[SI]p_A$. If $\sum_A p_A = 1$, where A is taken over all possible states, then $\sum_A [AST] = (n - 1)[SI]$.*

Proof. $\sum_A [AST] = (n - 1)[SI] \sum_A p_A = (n - 1)[SI]$. □

Improved closure

We note that while $p_{A|S-I}^{uc}$ satisfies the above proposition, $p_{A|S-I}^c$ does not. In particular, we find

$$\begin{aligned} \sum_A [AST] &= \sum_A (n - 1)[SI]p_{A|S-I}^{uc} = \sum_A (n - 1)[SI] \frac{[AS]}{n[S]} \\ &= \frac{(n - 1)[SI]}{n[S]} \sum_A [AS] = \frac{(n - 1)[SI]}{n[S]} n[S] = (n - 1)[SI]. \end{aligned}$$

However, for the clustered part of the network this is not the case. We find that

$$\begin{aligned} \sum_A [AST] &= \sum_A (n - 1)[SI]p_{A|S-I}^c = \sum_A (n - 1)[SI] \frac{[AS]}{n[S]} \frac{N[AI]}{n[A][I]} \\ &= \frac{(n - 1)N[SI]}{n^2[S][I]} \sum_A \frac{[AS][AI]}{[A]}, \end{aligned}$$

which does not result in the desired $(n-1)[SI]$. This can be corrected in a straightforward way by defining

$$p_{A|S-I}^{c_{new}} = \begin{cases} p_{A|S-I}^{uc} & \text{with probability } (1 - \phi), \\ \frac{p_{A|S-I}^c}{\sum_a p_{a|S-I}^c} & \text{with probability } \phi. \end{cases} \quad (4.17)$$

Hence we can now write

$$\begin{aligned} \sum_A [ASI] &= \sum_A ((1 - \phi)[ASI] + \phi[ASI]) \\ &= (1 - \phi)(n - 1)[SI] \sum_A p_{A|S-I}^{uc} + \phi(n - 1)[SI] \sum_A p_{A|S-I}^{c_{new}} \\ &= (1 - \phi)(n - 1)[SI] \sum_A \frac{[AS]}{n[S]} + \phi(n - 1)[SI] \sum_A \frac{p_{A|S-I}^c}{\sum_a p_{a|S-I}^c} \\ &= (1 - \phi)(n - 1)[SI] \frac{1}{n[S]} \sum_A [AS] + \phi(n - 1)[SI] \\ &= (1 - \phi)(n - 1)[SI] + \phi(n - 1)[SI] \\ &= (n - 1)[SI], \end{aligned}$$

as required. It is informative to investigate the relationship between the various probability models that lead to different closures. This is summarised in the following proposition.

Proposition 2. *For closures applied across the clustered part of the network and assuming that the number of nodes in state R is negligible, it follows that*

$$p_{S|S-I}^{c_{new}} = \frac{[SS][I]}{[SS][I] + [II][S]}, \quad p_{S|S-I}^c = \frac{[SS]}{n[S]} \frac{N[SI]}{n[S][I]}, \quad p_{S|S-I}^{uc} = \frac{[SS]}{n[S]}, \quad (4.18)$$

and

$$p_{S|S-I}^c \leq p_{S|S-I}^{uc} \quad \text{and} \quad p_{S|S-I}^{c_{new}} \leq p_{S|S-I}^{uc}. \quad (4.19)$$

Proof. All three probabilities follow from their definitions and assuming that $A \in \{S, I\}$. Since $S - I$ links are negatively correlated (4.11), it follows that $C_{SI} = \frac{N[SI]}{n[S][I]} \leq 1$ and as a result

$$p_{S|S-I}^c = \frac{[SS]}{n[S]} C_{SI} \leq \frac{[SS]}{n[S]} = p_{S|S-I}^{uc}. \quad (4.20)$$

While $p_{S|S-I}^c$ has a natural interpretation (it is a simple discounted variant of the probability from the unclustered network case and takes into account the observation that if

the neighbour of a central susceptible node is connected to one of the infected neighbours of the same node then it is less likely that the node in question is susceptible), the interpretation of $p_{S|S-I}^{c_{new}}$ is less obvious. A close inspection reveals that $p_{S|S-I}^{c_{new}}$ can be rewritten as

$$p_{S|S-I}^{c_{new}} = \frac{[SS][I]}{[SS][I] + [II][S]} = \frac{[SS]}{[SS] + [II]\frac{[S]}{[I]}}. \quad (4.21)$$

However, combining $[SI] \leq n[S]\frac{[I]}{N}$ with $[I] \leq \frac{N}{n}\frac{[II]}{[I]}$, as given in equation (4.11), leads to $[SI] \leq [II]\frac{[S]}{[I]}$. Finally, using the relation $[SI] \leq [II]\frac{[S]}{[I]}$ in equation (4.21) yields

$$p_{S|S-I}^{c_{new}} = \frac{[SS]}{[SS] + [II]\frac{[S]}{[I]}} \leq \frac{[SS]}{[SS] + [SI]} = \frac{[SS]}{n[S]} = p_{S|S-I}^{uc}. \quad (4.22)$$

Equation (4.22) illustrates that as expected $p_{S|S-I}^{c_{new}} \leq p_{S|S-I}^{uc}$. Again, this simply shows that for clustered networks and for the setup in Figure 4.2, it is less likely to find neighbours who are susceptible compared with the unclustered network case. \square

Taking into account the new way of defining $p_{A|S-I}^{c_{new}}$, the improved closure yields

$$\begin{aligned} [ASI] &= (1 - \phi)[ASI] + \phi[ASI] \\ &= (1 - \phi)(n - 1)[SI]\frac{[AS]}{n[S]} + \phi(n - 1)[SI]\frac{\frac{[AS]}{n[S]}C_{AI}}{\sum_a p_{a|S-I}^c} \\ &= (1 - \phi)\frac{(n - 1)}{n}\frac{[AS][SI]}{[S]} + \phi(n - 1)[SI]\frac{\frac{[AS]}{n[S]}\frac{N[A]}{n[A][I]}}{\sum_a \frac{[aS]}{n[S]}\frac{N[a]}{n[a][I]}} \\ &= (1 - \phi)\frac{(n - 1)}{n}\frac{[AS][SI]}{[S]} + \phi(n - 1)\frac{[AS][SI][IA]}{[A]\sum_a \frac{[aS][aI]}{[a]}} \\ &= (n - 1)\left((1 - \phi)\frac{[AS][SI]}{n[S]} + \phi\frac{[AS][SI][IA]}{[A]\sum_a [aS][aI]/[a]}\right). \end{aligned} \quad (4.23)$$

We finally note that the closures rely heavily on the assumption of how the states of the neighbours are distributed, and the assumption of independent and identically Bernoulli-distributed variables is a strong one. For clustered networks in particular, we have illustrated different ways of incorporating correlations induced by closed cycles of length three. Despite these seemingly strong assumptions, it is known that the pairwise model for unclustered networks is equivalent to the edge-based compartmental equivalent on configuration networks [76, 57] and the latter has been shown to be the limiting system of the stochastic network epidemic model [18, 48]. For clustered networks we are not aware of such results.

4.4 Results for the pairwise model with the simple closure

4.4.1 Background

Using the simple closure for clustered networks (4.16), and writing $\xi = \frac{(n-1)}{n}$, we obtain the following closed pairwise model equations describing an SIR epidemic on a clustered regular network of N individuals with degree n :

$$[\dot{S}] = -\tau[SI], \quad (4.24)$$

$$[\dot{I}] = \tau[SI] - \gamma[I], \quad (4.25)$$

$$[\dot{SI}] = -(\tau + \gamma)[SI] + \tau\xi \frac{[SS][SI]}{[S]} \left((1 - \phi) + \phi \frac{N[SI]}{n[S][I]} \right) - \tau\xi \frac{[SI]^2}{[S]} \left((1 - \phi) + \phi \frac{N[II]}{n[I]^2} \right), \quad (4.26)$$

$$[\dot{SS}] = -2\tau\xi \frac{[SS][SI]}{[S]} \left((1 - \phi) + \phi \frac{N[SI]}{n[S][I]} \right), \quad (4.27)$$

$$[\dot{II}] = 2\tau[SI] - 2\gamma[II] + 2\tau\xi \frac{[SI]^2}{[S]} \left((1 - \phi) + \phi \frac{N[II]}{n[I]^2} \right). \quad (4.28)$$

For model equations (4.24)-(4.28), in [54] the basic reproductive ratio (R_0) is considered. Starting from the evolution equation for the expected number of infectious individuals leads to

$$\begin{aligned} [\dot{I}] &= \tau[SI] - \gamma[I] \\ &= \left(\frac{\beta[S]}{N} C_{SI} - \gamma \right) [I], \end{aligned}$$

where C_{SI} is defined in equation (4.12). Taking into account that $\tau n = \beta$ and that initially $[S] \simeq N$, in [54] it is claimed that $R_0 = C_{SI}\beta/\gamma$. It is important to note that this R_0 is not the classical R_0 in the sense of describing the expected number of new infections produced by a typical infectious individual when introduced into a fully susceptible population. Rather it can be thought of as a growth-rate-based threshold, and has the same properties as the classical R_0 when both are exactly one. In what follows, we will simply refer to it as R [22, 56].

In order to determine R explicitly, the author in [54] considered the early behaviour of C_{SI} and found that this variable is given by the ordinary differential equation (ODE)

$$\dot{C}_{SI} = -\tau \left(C_{SI} + C_{SI}^2 - n\xi(C_{SI} - C_{SI}^2)(1 - \phi) + n\xi C_{SI}^2 \phi \frac{[I]C_{II}}{N} \right). \quad (4.29)$$

However, the ODE (4.29) depends on the behaviour of $[I]C_{II}/N$ and in [54] it was shown

that

$$\frac{[I]C_{II}}{N} \rightarrow \frac{2\tau C_{SI}}{\gamma + \beta C_{SI} - 2\xi\beta C_{SI}^2\phi}. \quad (4.30)$$

Considering the quasi-equilibrium of C_{SI} , referred to as C_{SI}^* , in equation (4.29) together with the expression for $[I]C_{II}/N$ in equation (4.30), one finds that C_{SI}^* is given by

$$1 + C_{SI}^* - n\xi(1 - C_{SI}^*)(1 - \phi) + \frac{2\tau n\xi\phi C_{SI}^{*2}}{\gamma + \beta C_{SI}^* - 2\xi\beta C_{SI}^{*2}\phi} = 0. \quad (4.31)$$

Hence, R can be calculated as $C_{SI}^*\beta/\gamma$, at least numerically. Variables such as C_{SI} and C_{II} describe the correlations between the states of neighbouring nodes on the network as the epidemic unfolds and these have been studied numerically in [54].

For model equations (4.24)-(4.28) and when there is no clustering present in the network structure (thus $\phi = 0$), a further simplification of equation (4.31) can be achieved [54]. To determine $R = C_{SI}^*\beta/\gamma$ in this case, simply solve

$$1 + C_{SI}^* - n\xi(1 - C_{SI}^*) = 0 \quad (4.32)$$

to find $C_{SI}^* = \frac{n-2}{n}$ and thus $R = \frac{(n-2)\tau}{\gamma}$.

Unfortunately when $\phi \neq 0$, according to our knowledge, the quasi-equilibrium values can only be determined numerically via equation (4.31). In what follows, we show that by working with two new variables, $\alpha := [SI]/[I]$ and $\delta := [II]/[I]$, which are still closely linked to the correlations formed during the spreading process, it is possible to obtain the epidemic threshold as the solution of a cubic equation and, more importantly, we show that this solution can be approximated by an asymptotic expansion in powers of ϕ .

4.4.2 Epidemic threshold

Consider the initial phase of an infection invading an entirely susceptible population in the pairwise model, described by equations (4.24)-(4.28). We find that

$$[\dot{I}] = \tau[SI] - \gamma[I] = \gamma[I] \left(\frac{\tau[SI]}{\gamma[I]} - 1 \right). \quad (4.33)$$

We know the quantity $\gamma[I]$ remains non-negative regardless of time in the epidemic process, and we choose to consider the threshold in terms of $\frac{[SI]}{[I]}$. This leads to $R = \frac{\tau[SI]}{\gamma[I]}$. When $R > 1$ an epidemic will occur, and when $R < 1$ the epidemic will die out. Although we know the values of τ and γ , to determine if an epidemic will occur *a priori*, we require further knowledge about the quantity $\frac{[SI]}{[I]}$ at some initial time close to $t = 0$. At $t = 0$

and at the disease-free steady state, both $[SI]$ and $[I]$ equal zero and hence their ratio is ill-defined. We will see that gaining knowledge about the behaviour of $\frac{[SI]}{[I]}$ will involve $\frac{[II]}{[I]}$ and this term is also ill-defined at time zero and at the disease-free steady state.

While this is similar to the approach taken in [54], we focus on the variables $\frac{[SI]}{[I]}$ and $\frac{[II]}{[I]}$, and we motivate our choice below. The problem of finding the epidemic threshold can be dealt with in at least two more different but equivalent ways. First, one can carry out a simple linear stability analysis of the disease-free steady state and this is shown in Appendices 4.C and 4.D. Second, the threshold can also be computed as the largest eigenvalue of the next generation matrix, see Section 4.6. However, in both cases, the variables $[SI]/[I]$ and $[II]/[I]$ turn out to play a key role and their values for small times need to be determined.

4.4.3 Fast variables with the simple closure

To circumvent the problem of the ill-defined variables above, we exploit the fact that $\alpha = \frac{[SI]}{[I]}$ and $\delta = \frac{[II]}{[I]}$ are fast variables when compared to the time course of the epidemic. Figure 4.3 shows clearly that α and δ are fast compared to the epidemic process and that they quickly converge to a quasi-equilibrium. Hence, at early times α and δ attain their quasi-equilibrium values, and these are the values that can be used to compute the epidemic threshold.

We continue by deriving differential equations for the variables $\alpha = \frac{[SI]}{[I]}$ and $\delta = \frac{[II]}{[I]}$. Differentiating α and δ and using equations (4.24)-(4.28) leads to

$$\frac{d\alpha}{dt} = -\tau\alpha + \tau\xi n(1-\phi)\alpha + \tau\xi\phi\alpha^2 - \tau\xi\frac{1}{n}\phi\alpha^2\delta - \tau\alpha^2, \quad (4.34)$$

$$\frac{d\delta}{dt} = 2\tau\alpha - \gamma\delta + 2\tau\xi\frac{1}{n}\phi\alpha^2\delta - \tau\alpha\delta. \quad (4.35)$$

The detailed derivation for equations (4.34) and (4.35) can be found in Appendix 4.A.

Fast variables without clustering

When clustering is negligible and hence $\phi = 0$, we find that

$$\frac{d\alpha}{dt} = -\tau\alpha + \tau\xi n\alpha - \tau\alpha^2, \quad (4.36)$$

$$\frac{d\delta}{dt} = 2\tau\alpha - \gamma\delta - \tau\alpha\delta, \quad (4.37)$$

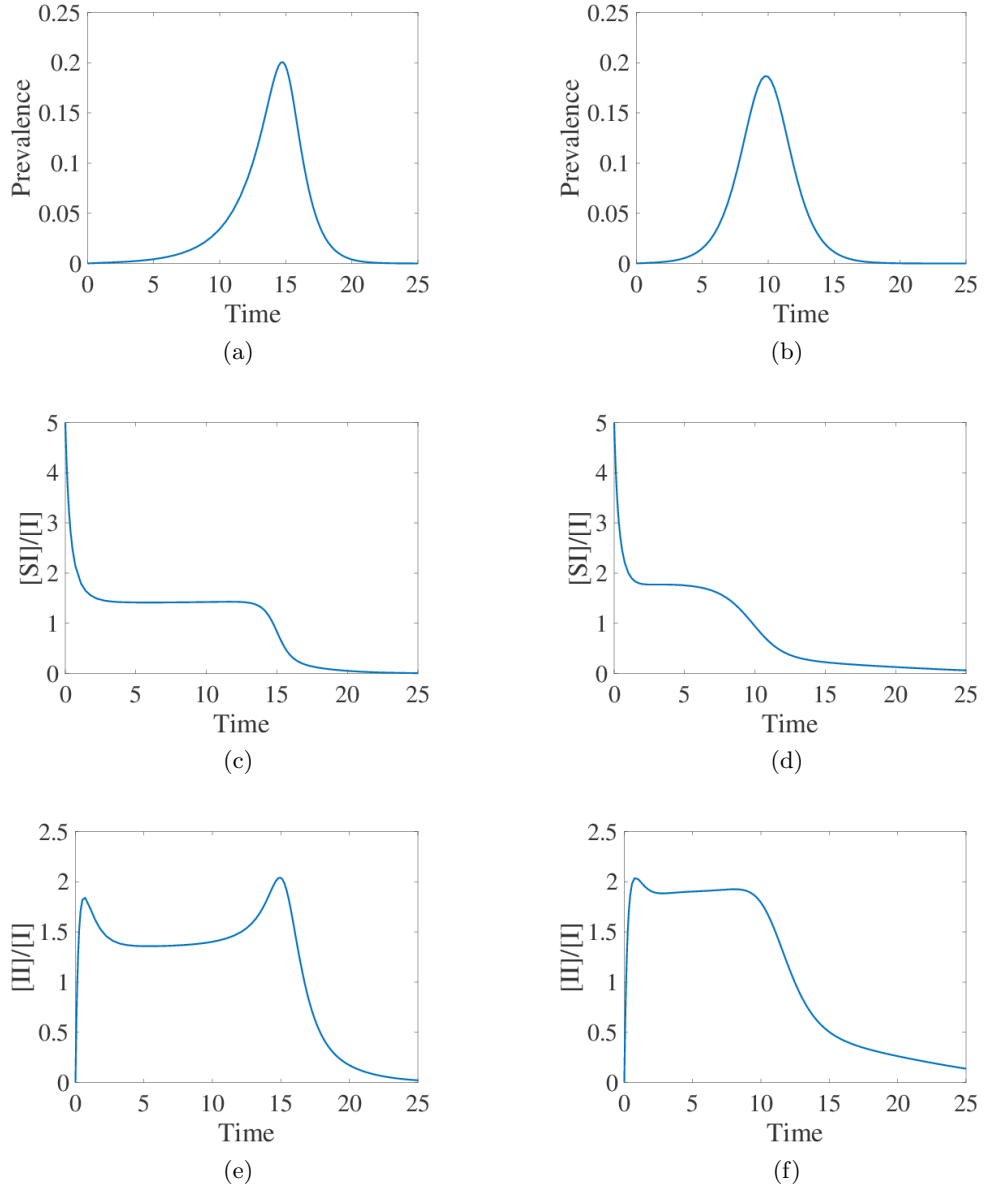


Figure 4.3: Illustration of the dynamics of prevalence, $[I]/N$, over time ((a)-(b)), compared to that of $\alpha = \frac{[SI]}{[I]}$ ((c)-(d)) and $\delta = \frac{[II]}{[I]}$ ((e)-(f)) for the pairwise model with the simple (left column) and the improved (right column) closures. Parameter values are $N = 10000$, $n = 5$, $\phi = 0.5$ and $\tau = \gamma = 1$.

where $\xi = \frac{(n-1)}{n}$. The steady states of the system (4.36)-(4.37) are given by $(\alpha_1^*, \delta_1^*) = (0, 0)$ and $(\alpha_2^*, \delta_2^*) = \left((n-2), \frac{2\tau(n-2)}{\gamma + \tau(n-2)} \right)$. Based on equation (4.33), it follows that $R = \frac{\tau\alpha_2^*}{\gamma} = \frac{\tau(n-2)}{\gamma}$.

Fast variables with clustering

When clustering is present in the network, the differential equations for α and δ are more complex and thus steady states are harder to compute. Firstly, we set equation (4.34)

equal to zero and rearrange to isolate δ , finding

$$\delta = \frac{-1 + \xi n(1 - \phi) + \xi \phi \alpha - \alpha}{\xi \frac{1}{n} \phi \alpha}. \quad (4.38)$$

Plugging equation (4.38) into equation (4.35) leads to the following cubic equation in α :

$$\begin{aligned} & (2\tau\xi\phi(1 - \xi\phi))\alpha^3 + (\tau\xi n\phi - 2\tau\xi^2 n\phi(1 - \phi) - \tau n)\alpha^2 \\ & + (-n(\tau + \gamma) + \tau\xi n^2(1 - \phi) + \gamma\xi n\phi)\alpha + (\gamma\xi n^2(1 - \phi) - \gamma n) = 0. \end{aligned} \quad (4.39)$$

The solution of the cubic equation (4.39) provides the steady state(s) of system (4.34)-(4.35), and allows the computation of the threshold via the formula $R^c = \frac{\tau\alpha^*}{\gamma}$. We note that the steady state in α has to be biologically plausible. $\alpha = \frac{[SI]}{[I]}$ restricts the steady state to be positive and to be less than n , since the average number of susceptible neighbours averaged over all infected nodes needs to be less than the average degree.

4.4.4 Asymptotic expansion of the epidemic threshold

The case of $\phi \neq 0$ can be regarded as a perturbation of the case with no clustering and we thus set out to find α using a perturbation method. More precisely, we seek to find the roots of the cubic polynomial, given in equation (4.39), in terms of an asymptotic expansion in powers of ϕ , that is

$$\alpha = \alpha_0 + \phi\alpha_1 + \phi^2\alpha_2 + \dots. \quad (4.40)$$

Plugging (4.40) into equation (4.39) leads to

$$\begin{aligned} & 2\tau\xi\phi(1 - \xi\phi)(\alpha_0 + \phi\alpha_1 + \phi^2\alpha_2 + \dots)^3 \\ & + (\tau\xi n\phi - 2\tau\xi^2 n\phi(1 - \phi) - \tau n)(\alpha_0 + \phi\alpha_1 + \phi^2\alpha_2 + \dots)^2 \\ & + (-n(\tau + \gamma) + \tau\xi n^2(1 - \phi) + \gamma\xi n\phi)(\alpha_0 + \phi\alpha_1 + \phi^2\alpha_2 + \dots) \\ & + (\gamma\xi n^2(1 - \phi) - \gamma n) = 0. \end{aligned} \quad (4.41)$$

Collecting terms of order ϕ^0 in (4.41) and after some algebra we find that α_0 satisfies:

$$n(\alpha_0 - (n - 2))(\tau\alpha_0 + \gamma) = 0. \quad (4.42)$$

Hence, $\alpha_0 = (n - 2)$. The other solution $\alpha_0 = -\gamma/\tau$ is not biologically feasible since by definition α is positive. As expected, $\alpha_0 = (n - 2)$ corresponds to the unclustered case.

Collecting terms of order ϕ in (4.41), we find a polynomial in terms of α_0 and α_1 :

$$2\tau\xi\alpha_0^3 + (\tau\xi n - 2\tau\xi^2 n)\alpha_0^2 + (\gamma\xi n - \tau\xi n^2)\alpha_0 - 2\tau n\alpha_0\alpha_1 + (\tau\xi n^2 - n(\tau + \gamma))\alpha_1 - \gamma\xi n^2 = 0. \quad (4.43)$$

Equation (4.43) leads to

$$\alpha_1 = \frac{\gamma\xi n^2 - 2\tau\xi\alpha_0^3 + (2\tau\xi^2 n - \tau\xi n)\alpha_0^2 + (\tau\xi n^2 - \gamma\xi n)\alpha_0}{\tau\xi n^2 - n(\tau + \gamma) - 2\tau n\alpha_0},$$

which after substituting $\alpha_0 = (n - 2)$ and $\xi = \frac{(n-1)}{n}$ yields

$$\alpha_1 = \frac{-2(n-1)}{n^2} \left(\frac{2\tau(n-1)(n-2) + \gamma n}{\tau(n-2) + \gamma} \right). \quad (4.44)$$

To summarise, we have determined the first two coefficients α_0 and α_1 of the asymptotic expansion (4.40) which solves the cubic equation (4.39). Hence, the true solution is approximated by:

$$\alpha = (n-2) - \phi \frac{2(n-1)}{n^2} \left(\frac{2\tau(n-1)(n-2) + \gamma n}{\tau(n-2) + \gamma} \right) + \mathcal{O}(\phi^2). \quad (4.45)$$

We make several remarks. First, the epidemic threshold will be given by $R^c = \tau\alpha/\gamma$. Second, the coefficient of the first order correction of α can be rearranged in terms of $R = \frac{\tau(n-2)}{\gamma}$, the threshold for the case of unclustered networks, leading to

$$R^c = R - \phi a \frac{\tau}{\gamma} \left(\frac{aR + 1}{R + 1} \right), \quad (4.46)$$

where $a = 2(n-1)/n$ and where terms in ϕ of order larger than one have been neglected. Finally, it is clear that due to the first order correction being negative, we have that

$$R^c = R - \phi a \frac{\tau}{\gamma} \left(\frac{aR + 1}{R + 1} \right) \leq R = \frac{\tau(n-2)}{\gamma}. \quad (4.47)$$

The goodness of the estimate for α (4.45) is tested by comparing it to the numerical solution of the cubic equation (4.39). This is done in Figure 4.4 for five different values of the clustering coefficient. The asymptotic approximation performs well and only breaks down for values of clustering larger than $\simeq 0.3$. From the same figure it is clear that higher values of clustering push the critical $R^c = 1$ curve to higher values of τ and n . Hence, in the presence of clustering a viable epidemic requires either a denser network or a higher transmission rate, noting that the transmission rate and the recovery rate γ are not strictly independent.

4.4.5 Numerical examples

In the previous section we have demonstrated that for the pairwise model with the simplest closure for clustered networks, the determination of the epidemic threshold involves the solution of a cubic equation. While this can be obtained numerically, we presented an asymptotic approximation of the solution in terms of powers of the clustering coefficient ϕ . In Figure 4.4 we present a systematic test of the newly determined threshold by comparing the threshold based on the numerical solution of the cubic equation (4.39) (continuous line in the $(\tau, n, 0)$ plane), the asymptotic approximation of the solution to the cubic equation (4.45) (dashed line and markers - \circ) and the numerical solution of the full ODE system corresponding to the closed pairwise model (4.24)-(4.28).

The agreement between the explicit numerical solution of the closed pairwise system and threshold based on the numerical solution of the cubic equation is excellent for all clustering values and other parameter combinations. Moreover, the agreement of these results with the threshold based on the asymptotic approximation is also excellent and remains valid for values of $0 \leq \phi \leq 0.3$. Our numerical tests confirm that our analytical results are correct. The initial conditions for the closed pairwise systems were set in the following way: $[I](0) = I_0 = 1$, $[S](0) = N - I_0 = S_0$, $[SI](0) = nI_0 \frac{S_0}{N}$, $[SS](0) = nS_0 \frac{S_0}{N}$ and $[II](0) = nI_0 \frac{I_0}{N}$. The ODEs were run for a sufficiently long time ($T_{max} = 1000$) to ensure that the epidemic died out. It is worth noting that the correct numerical solution of the cubic equation can be chosen by keeping in mind that $0 \leq \alpha = \frac{[SI]}{[I]} \leq n$.

4.5 Results for the pairwise model with the compact improved closure

Starting from the improved closure (4.23) but in line with Proposition 2, we adapt the closure so that the term responsible for the approximation on the clustered part of the network does not consider variables, singles or pairs involving the recovered/removed class. This leads to the new closure

$$[AST] = (n - 1) \left((1 - \phi) \frac{[AS][SI]}{n[S]} + \phi \frac{[AS][SI][IA]}{[A] \left(\frac{[SS][SI]}{[S]} + \frac{[SI][II]}{[I]} \right)} \right), \quad (4.48)$$

which we refer to as the compact improved closure. Plugging equation (4.48) into the exact system (4.5)-(4.9) leads to a self-consistent system that is written out in full in Appendix 4.B.

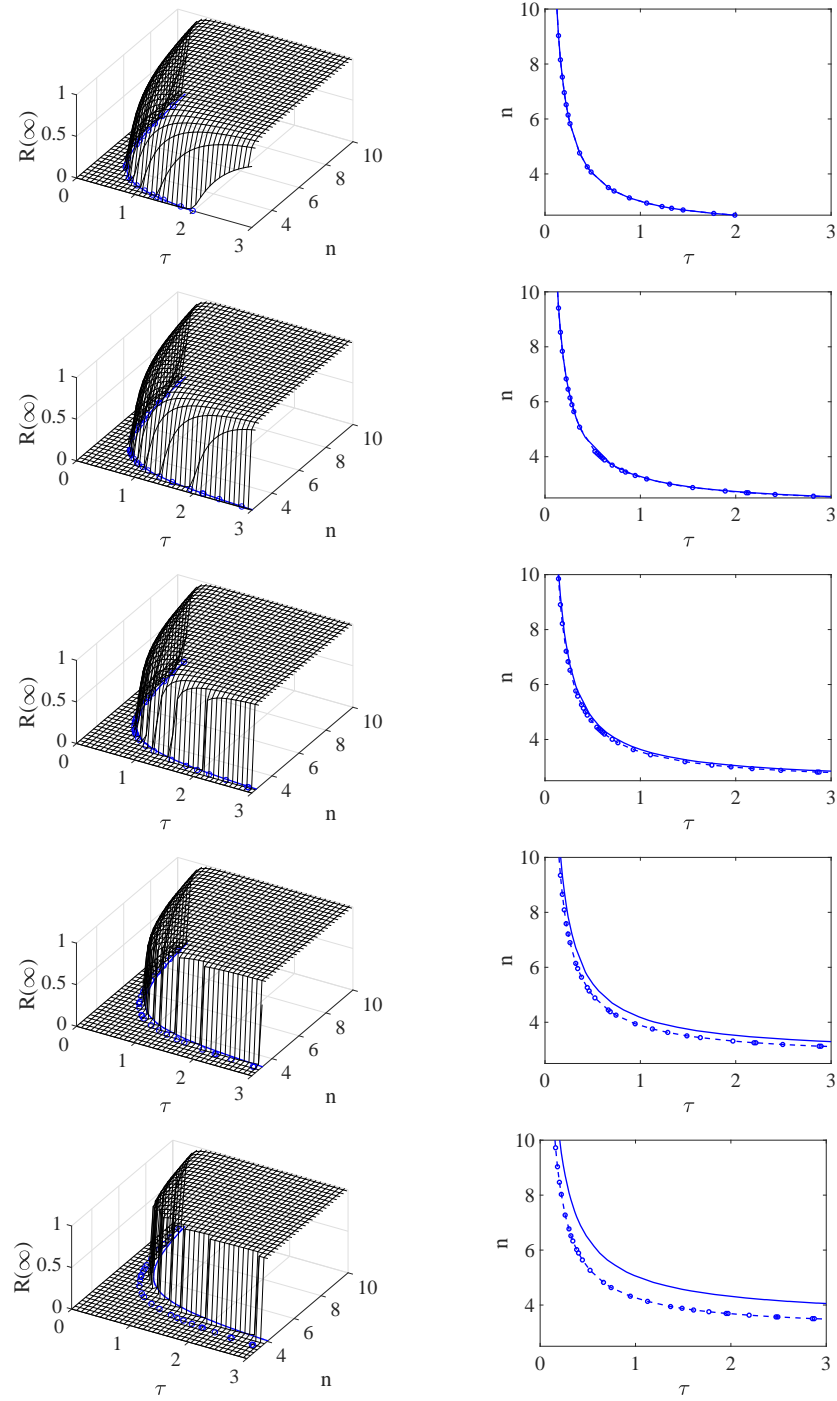


Figure 4.4: Assessing the validity of the epidemic threshold based on the asymptotic approximation (4.45) (dashed line and markers - \circ) by comparing it to the epidemic threshold based on the numerical solution of the cubic equation (4.39) (continuous lines). In the right hand column we compare both threshold curves in the $(\tau, n, 0)$ plane. In the left hand column both curves are compared to the final epidemic size based on numerical integration of the pairwise model equations with the simple closure. Parameter values are $N = 10000$, $\gamma = 1$ and from top to bottom the clustering coefficients are $\phi = 0, 0.15, 0.3, 0.45, 0.6$.

In line with our procedure so far, we aim to find the epidemic threshold of this new pairwise system with the compact improved closure. It turns out that the approach used

for the pairwise system with the simple closure is applicable to this case, and the steps and results are summarised below.

4.5.1 Fast variables with the compact improved closure

As we have shown before, finding the threshold relies on finding the quasi-equilibrium of $\alpha = \frac{[SI]}{[I]}$. In Appendix 4.B we show that this requires knowledge about the behaviour of the $\delta = \frac{[II]}{[I]}$ variable and indeed a system of differential equations involving these two variables can be derived. This system is given below

$$\frac{d\alpha}{dt} = -\tau\alpha - \tau\alpha^2 + \tau(n-1) \left((1-\phi)\alpha + \phi\alpha \left(\frac{n-\delta}{n+\delta} \right) \right), \quad (4.49)$$

$$\frac{d\delta}{dt} = 2\tau\alpha - \gamma\delta + 2\tau(n-1) \left(\frac{\phi\alpha\delta}{n+\delta} \right) - \tau\alpha\delta. \quad (4.50)$$

As previously, the steady states of this system are of interest and apart from the trivial $(\alpha^*, \delta^*) = (0, 0)$ steady state, the quasi-equilibrium can be found by first expressing δ as a function of α . This can be done by setting equation (4.49) equal to zero and rearranging, leading to

$$\alpha = (n-2) - (n-1)\phi \frac{2\delta}{n+\delta}. \quad (4.51)$$

Plugging equation (4.51) into equation (4.50) and collecting powers of δ leads to the following cubic equation

$$\begin{aligned} &(-A-B)\delta^3 + (-n(n-2) - A^2 - 2nB)\delta^2 \\ &+ (-n(n-2)A + 2nA - n^2B)\delta + 2n^2(n-2) = 0, \end{aligned} \quad (4.52)$$

where $A = (n-2) - 2\phi(n-1)$ and $B = \gamma/\tau$. It is worth noting that in this case it is easier to work with δ , but any results can be converted in terms of α which is the main variable of interest.

4.5.2 Asymptotic expansion of the epidemic threshold

As in Section 4.4.4, we require the roots of the cubic polynomial given in equation (4.52). To do so, we express δ as an asymptotic expansion in powers of ϕ . We substitute

$$\delta = \delta_0 + \delta_1\phi + \delta_2\phi^2 + \dots. \quad (4.53)$$

Plugging the expansion for δ (4.53) into equation (4.52) leads to

$$\begin{aligned} & (-A-B)(\delta_0+\delta_1\phi+\delta_2\phi^2+\dots)^3 + (-n(n-2)-A^2-2nB)(\delta_0+\delta_1\phi+\delta_2\phi^2+\dots)^2 \\ & + (-n(n-2)A+2nA-n^2B)(\delta_0+\delta_1\phi+\delta_2\phi^2+\dots) + 2n^2(n-2) = 0. \end{aligned} \quad (4.54)$$

Alternatively, substituting (4.51) into the differential equation for δ (4.50), setting the expression equal to zero and rearranging leads to

$$\gamma\delta(n+\delta)^2 = \tau[(n-2)(n+\delta) - 2\phi(n-1)\delta][(2-\delta)(n+\delta) + 2\phi(n-1)\delta]. \quad (4.55)$$

Substituting (4.53) into (4.55) and collecting terms of order ϕ^0 yields

$$\gamma\delta_0(n+\delta_0)^2 = \tau[(n-2)(n+\delta_0)][(2-\delta_0)(n+\delta_0)] \quad (4.56)$$

$$\gamma\delta_0 = \tau(n-2)(2-\delta_0) \quad (4.57)$$

$$\delta_0(\gamma + \tau(n-2)) = 2\tau(n-2) \quad (4.58)$$

$$\delta_0 = \frac{2\tau(n-2)}{\gamma + \tau(n-2)}. \quad (4.59)$$

Following the same process to collect terms of order ϕ^1 , we find

$$\begin{aligned} \gamma\delta_1[(n+\delta_0)^2 + 2(n+\delta_0)\delta_0] &= \tau(n-2)(n+\delta_0)[\delta_1(2-n-2\delta_0) + 2(n-1)\delta_0] \\ &+ \tau(2-\delta_0)(n+\delta_0)[(n-2)\delta_1 - 2(n-1)\delta_0], \end{aligned} \quad (4.60)$$

which can be rearranged to yield

$$\delta_1 = \frac{2\tau(n-1)\delta_0(n-4+\delta_0)}{\gamma(n+3\delta_0) + \tau(n-2)(n+3\delta_0-4)}, \quad (4.61)$$

with δ_0 defined in (4.59). In summary, we have determined the first two coefficients δ_0 and δ_1 of the asymptotic expansion for δ given in equation (4.53). Hence, the true solution is approximated by the following expression:

$$\delta = \frac{2\tau(n-2)}{\gamma + \tau(n-2)} + \frac{2\tau(n-1)\delta_0(n-4+\delta_0)\phi}{\gamma(n+3\delta_0) + \tau(n-2)(n+3\delta_0-4)} + \mathcal{O}(\phi^2). \quad (4.62)$$

Finally, we are able to plug (4.62) into the quasi-equilibrium point for α , given in equation (4.51), to obtain

$$\alpha = (n-2) - 2(n-1)\phi \frac{\delta_0}{n+\delta_0} + \mathcal{O}(\phi^2), \quad (4.63)$$

which, upon neglecting terms in ϕ of order larger than one, can be rearranged to find

$$\alpha = (n-2) - \phi \frac{4\tau(n-1)(n-2)}{\tau(n+2)(n-2) + \gamma n}. \quad (4.64)$$

The expression for α (4.64) can be used to determine the epidemic threshold as follows

$$R^{cci} = \frac{\tau\alpha}{\gamma} = \frac{(n-2)\tau}{\gamma} - \phi \frac{\tau}{\gamma} \left(\frac{4\tau(n-1)(n-2)}{\tau(n+2)(n-2) + \gamma n} \right). \quad (4.65)$$

It is straightforward to see that again $R^{cci} \leq R$, with clustering making the spread of the epidemic less likely.

4.5.3 Numerical examples

In Figure 4.5 we repeat the systematic test of comparing the epidemic threshold generated via the numerical solution of the cubic equation (4.52), the epidemic threshold generated by the asymptotic expansion (4.65) and the numerical value of the final epidemic size predicted by pairwise model with the compact improved closure, over a wide range of (τ, n) values. Several observations can be made. First, it is clear that higher values of clustering push the location of the threshold to higher τ and n values, meaning that the limiting effect of clustering on the epidemic spread can only be overcome if either the value of the transmission rate or average degree increases. Second, the agreement between the threshold based on the numerical solution of the cubic equation (4.52) and the asymptotic expansion (4.62) is excellent over a wide range of ϕ values. In fact, in this case the agreement is excellent for $0 \leq \phi \leq 0.45$, with only small deviations even for $\phi = 0.6$. The agreement between the numerical solution of the pairwise model and the threshold based on the numerical solution of the cubic equation (4.52) remains excellent across all parameter values.

4.6 Discussion

In this chapter we set out to obtain an analytic epidemic threshold using pairwise models but for clustered networks. For the unclustered case this problem has been solved previously [54]. Furthermore, in [54] it was shown that one way to approach the computation of the threshold is to exploit the presence of fast variables. In particular, working out the quasi-steady state of the fast variables allowed the authors to determine the epidemic threshold analytically. However, this was done only for the case when the network is unclustered. Here, we went one step further and showed that the quasi-equilibrium can be found as an asymptotic expansion in powers of the clustering coefficient. Prior to this new result we re-derived known closures by providing extra intuition for the assumptions underlying them as well as for the motivation for deriving them.

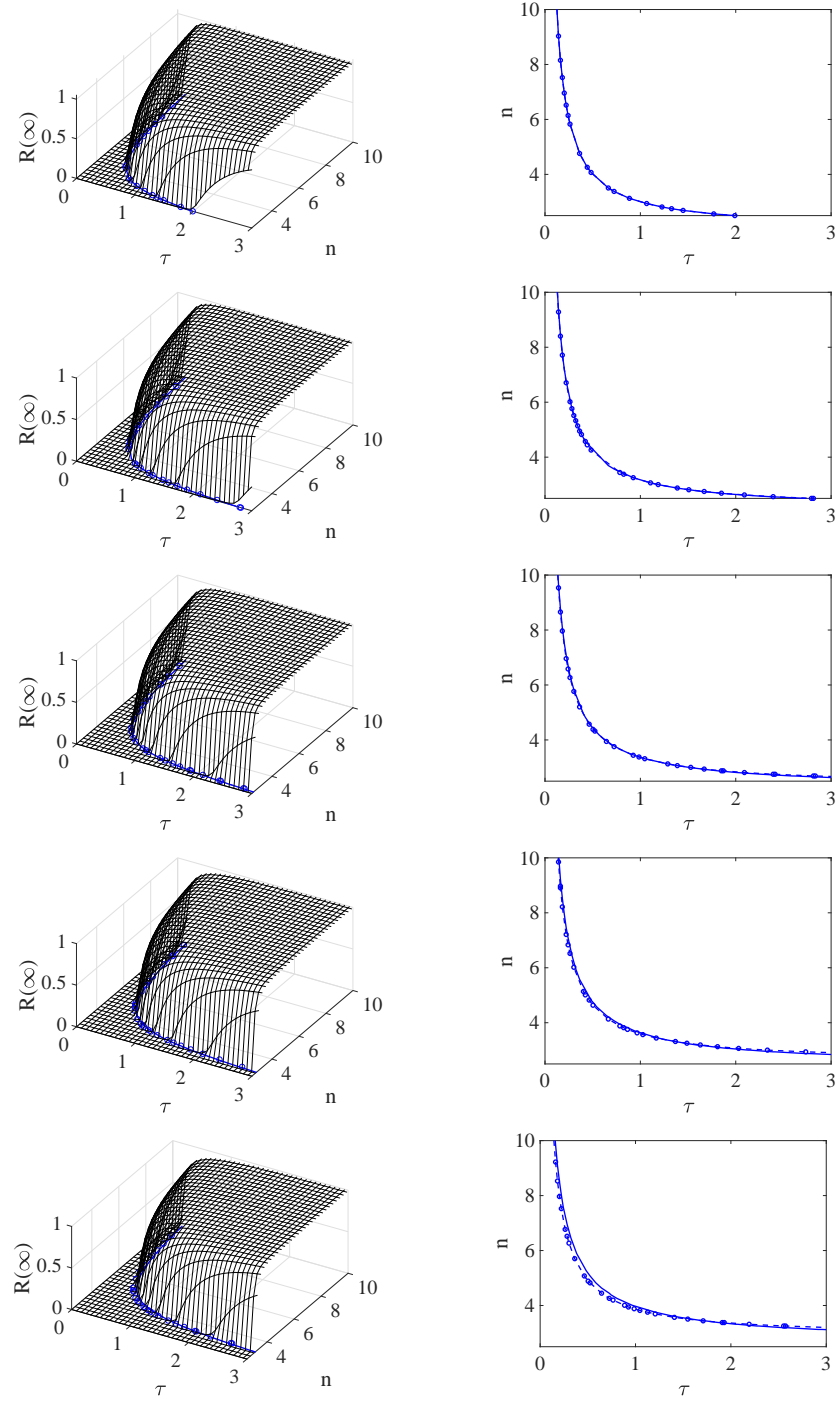


Figure 4.5: Assessing the validity of the epidemic threshold based on the asymptotic expansion (4.62) (dashed line and markers - \circ) by comparing it to the epidemic threshold based on the numerical solution of the cubic equation (4.52) (continuous lines). In the right hand column we compare both threshold curves in the $(\tau, n, 0)$ plane. In the left hand column both curves are compared to the final epidemic size based on numerical integration of the pairwise model equations with the compact improved closure. Parameter values are $N = 10000$, $\gamma = 1$ and from top to bottom the clustering coefficients are $\phi = 0, 0.15, 0.3, 0.45, 0.6$.

Exploiting the presence of fast variables and combining this with elements of perturbation theory allowed us to compute the epidemic threshold for the pairwise model with two different closures that take clustering into account. Our results are in line with the findings of [60] and [72]. In [60], the epidemic threshold in a pairwise model for clustered networks with a closure based on the number of links in a motif, rather than nodes, was calculated as

$$R_0 = \frac{(n-1)\tau}{\tau + \gamma + \tau\phi}. \quad (4.66)$$

Equation (4.66) can be expanded in terms of ϕ to give

$$R_0 = \frac{(n-1)\tau}{\tau + \gamma} \left(\frac{1}{1 + \phi \frac{\tau}{\tau + \gamma}} \right) \simeq \frac{(n-1)\tau}{\tau + \gamma} \left(1 - \phi \frac{\tau}{\tau + \gamma} + \dots \right), \quad (4.67)$$

which again reflects our finding that clustering reduces the epidemic threshold.

Similarly but for clustered networks with heterogeneous degree distributions, in [72] it was found that

$$R_0 = \frac{\langle k^2 - k \rangle}{\langle k \rangle} T - \frac{2\langle n_\Delta \rangle}{\langle k \rangle} T^2 + \dots, \quad (4.68)$$

where $\langle k^i \rangle$ stands for the i th moment of the degree distribution, T is the probability of infection spreading across a link connecting an infected to a susceptible node and $\langle n_\Delta \rangle$ denotes the average number of triangles that a node belongs to. The expression above again shows that clustering reduces the epidemic threshold when compared to the unclustered case. Furthermore, if the network is regular and we assume that infections and recoveries are Markovian processes with rates τ and γ respectively, giving $T = \tau/(\tau + \gamma)$, R_0 above reduces to

$$R_0 = \frac{\tau(n-1)}{\tau + \gamma} - (n-1)\phi \left(\frac{\tau}{\tau + \gamma} \right)^2 + \dots, \quad (4.69)$$

where we have used the fact that a global clustering coefficient of ϕ translates to a node on average being part of $\frac{1}{2}n(n-1)\phi$ uniquely counted triangles. This in turn coincides with equation (4.67), and this is perhaps unexpected since the first expression was obtained based on a new type of closure for pairwise models while the other expression was based on percolation theory type arguments. In [112], specific networks with household structure were used to investigate the effects of clustering and infectious period distribution on a modified version of R_0 referred to as R_* , and lower and upper bounds for the value of this quantity were found.

Our analysis confirms that clustering starves the spreading epidemic of susceptible neighbours such that the epidemic is less likely to spread if the networks are clustered,

all other parameters being equal. More importantly, the epidemic threshold is model-dependent and the pairwise model with the compact improved closure leads more readily to epidemic outbreaks when compared to the pairwise model with the simple closure, see Figures 4.4 - 4.5. While this ordering is true for the parameters used in this chapter, it is easy to show that this relation can change if parameters are tuned accordingly. For example, looking at the limit of $\gamma \rightarrow 0$ (or τ/γ large limit), the two epidemic thresholds are the same if

$$\frac{2(n-1)}{n^2} \left(\frac{2(n-1)(n-2)}{(n-2)} \right) = \frac{4(n-1)(n-2)}{(n-2)(n+2)}. \quad (4.70)$$

After some simple algebra this reduces to $n = 2$. Hence, if the τ/γ ratio is large we will essentially have that (i) if $n > 2$ then $R_0^c < R_0^{cci}$, and (ii) if $n < 2$ then $R_0^c > R_0^{cci}$. This highlights the difficulty of determining the epidemic threshold and emphasises the importance of model choice when modelling real-world epidemics.

The analysis of the pairwise model with the full improved closure is still outstanding and will be the subject of a separate research paper. In this case, we expect that additional fast-variables need to be identified. Intuition tells us that $\frac{[SI]}{[I]}$ and $\frac{[II]}{[I]}$ may need to be extended to include $\frac{[SR]}{[R]}$ and $\frac{[RI]}{[I]}$.

The computation of the true R_0 for pairwise models can be attempted by considering the next generation matrix approach [116]. Looking at the pairwise model with the simplest closure and ordering the variables involved in the spreading process as: $[I], [SI]$, the generation of new infectious cases at the disease-free steady state is given by

$$F = \begin{pmatrix} 0 & \tau \\ 0 & \tau(n-1)(1-\phi) + \tau\xi\phi\alpha \end{pmatrix}, \quad (4.71)$$

where the lower right term is obtained from equation (4.26) by looking at the rate of growth of $[SI]$ in terms of $[SI]$ itself and evaluating the terms $[S]$ and $[SS]$ at the disease-free equilibrium, that is

$$[\dot{SI}] = +\tau\xi \frac{[SS]}{[S]} \left((1-\phi) + \phi \frac{N}{n} \frac{[SI]}{[I]} \right) [SI] \simeq (\tau(n-1)(1-\phi) + \tau\xi\phi\alpha) [SI].$$

Now all other transfers between compartments are summarised in the V matrix, which is given below

$$V = \begin{pmatrix} \gamma & 0 \\ 0 & (\tau + \gamma) + \tau \frac{\xi}{n} \alpha \delta \phi \end{pmatrix}, \quad (4.72)$$

where the lower right term describes the rate at which $[SI]$ pairs are depleted. This is

obtained from equation (4.26) by looking at the rate at which $[SI]$ pairs are depleted and evaluating the terms $[S]$ and $[SI]$ at the disease-free equilibrium, as shown below

$$[\dot{SI}] = - \left((\tau + \gamma) + \tau \xi \frac{[SI]}{[S]} (1 - \phi) + \phi \tau \xi \frac{[SI]}{[S]} \frac{N[II]}{n[I]^2} \right) [SI] \simeq -((\tau + \gamma) + \tau \frac{\xi}{n} \alpha \delta \phi) [SI].$$

Now R_0 is given by the leading eigenvalue of FV^{-1} , which turns out to be

$$R_0 = \frac{\tau n(n-1) - \tau(n-1)(n-\alpha)\phi}{n(\tau + \gamma) + \tau \xi \alpha \delta \phi}. \quad (4.73)$$

Obviously, this seems like a rather complicated expression since the quasi-equilibrium values for α and δ are needed. These are only available as asymptotic expansions in powers of ϕ . Nevertheless, for $\phi = 0$, $R_0 = \frac{\tau(n-1)}{\tau + \gamma}$, which agrees perfectly with the two results quoted above. Considering the $\phi > 0$ case, we write $R_0 = r_0 + \phi r_1$, $\alpha = \alpha_0 + \phi \alpha_1$ and $\delta = \delta_0 + \phi \delta_1$. Plugging these into equation (4.73) leads to

$$r_0 = \frac{\tau(n-1)}{\tau + \gamma} \quad \text{and} \quad r_1 = - \frac{\tau^2(n-1)}{(\tau + \gamma)^2} \left[\frac{2(\tau + \gamma)}{n\tau} + \frac{(n-1)}{n} \alpha_0 \delta_0 \right].$$

While the first term in the expansion for R_0 agrees with the results quoted above, the second term seems less likely to be equivalent to those shown above. This same approach can be used to compute R_0 when the compact improved closure is used. We believe that comparing these different ways of computing the epidemic threshold can contribute to reconciling different methods and will lead to more clarity and transparency between various modelling approaches.

The ODE systems for the fast variables are worth investigating in more detail. We expect that these systems will exhibit a number of steady states, some stable and some unstable. Namely, we expect the quasi-steady states to be unstable and the trivial zero steady states to be stable. However, numerical solutions of the cubic polynomials show that other equilibria exist. It will also be worthwhile to compare different models in order to identify the impact of clustering on epidemics by mapping out regions in the parameter space where its effect is strongest. It is known that when the network is dense the effect of clustering is limited and the same holds when the transmission/recovery rates are high/low, respectively. Of course there remains the issue of accounting for degree heterogeneity and this has been addressed to some extent by using percolation type approaches. The approach that we presented in this chapter may be extended to degree-heterogeneous clustered networks, but this will require more sophisticated models such as effective-degree, or compact/super-compact pairwise models [106]. These will no doubt lead to more com-

plex systems which are more challenging to analyse. However, we hope that the results of this chapter may encourage other researchers to consider and tackle the challenges posed by modelling epidemic dynamics on clustered networks with heterogeneous degree distributions. Finally, it would be worthwhile to test our findings against explicit stochastic network simulations. This was beyond the scope of the present work, whose focus was on exploiting the presence of fast variables and the use of perturbation analysis to determine the epidemic threshold analytically.

4.7 Acknowledgements

Rosanna C Barnard acknowledges funding for her PhD studies from the Engineering and Physical Sciences Research Council (EP/M506667/1). Péter L. Simon acknowledges support from Hungarian Scientific Research Fund, OTKA, (grant no. 115926).

Appendices

4.A Derivation of evolution equations for the fast variables with simple closure

We begin by computing differential equations for the variables $\alpha := \frac{[SI]}{[I]}$ and $\delta := \frac{[II]}{[I]}$.

Differentiating $\alpha = \frac{[SI]}{[I]}$ gives

$$\begin{aligned}\frac{d\alpha}{dt} &= \frac{[\dot{S}I][I] - [SI][\dot{I}]}{[I]^2} \\ &= \frac{[\dot{S}I]}{[I]} - \frac{[SI][\dot{I}]}{[I]^2},\end{aligned}$$

and substituting $[\dot{S}I]$ from equation (4.26) and $[\dot{I}]$ from equation (4.25), we obtain

$$\begin{aligned}\frac{d\alpha}{dt} &= -(\tau + \gamma) \frac{[SI]}{[I]} + \tau\xi \frac{[SS][SI]}{[S][I]} \left((1 - \phi) + \phi \frac{N[SI]}{n[S][I]} \right) \\ &\quad - \tau\xi \frac{[SI]^2}{[S][I]} \left((1 - \phi) + \phi \frac{N[II]}{n[I]^2} \right) - \tau \frac{[SI]^2}{[I]^2} + \gamma \frac{[SI]}{[I]}.\end{aligned}$$

Replacing all $\frac{[SI]}{[I]}$ terms by α and all $\frac{[II]}{[I]}$ terms by δ gives

$$\begin{aligned}\frac{d\alpha}{dt} &= -(\tau + \gamma)\alpha + \tau\xi \frac{[SS]}{[S]}\alpha \left((1 - \phi) + \phi \frac{N}{n[S]}\alpha \right) - \tau\xi \frac{[SI]}{[S]}\alpha \left((1 - \phi) + \phi \frac{N}{n[I]}\delta \right) - \tau\alpha^2 + \gamma\alpha \\ &= -\tau\alpha + \tau\xi \frac{[SS]}{[S]}\alpha \left((1 - \phi) + \phi \frac{N}{n[S]}\alpha \right) - \tau\xi \frac{[SI]}{[S]}\alpha \left((1 - \phi) + \phi \frac{N}{n[I]}\delta \right) - \tau\alpha^2 \\ &= -\tau\alpha + \tau\xi \frac{[SS]}{[S]}(1 - \phi)\alpha + \tau\xi\phi \frac{N[SS]}{n[S]^2}\alpha^2 - \tau\xi \frac{[SI]}{[S]}(1 - \phi)\alpha - \tau\xi \frac{N[SI]}{n[S][I]}\phi\alpha\delta - \tau\alpha^2 \\ &= -\tau\alpha + \tau\xi \frac{[SS]}{[S]}(1 - \phi)\alpha + \tau\xi\phi \frac{N[SS]}{n[S]^2}\alpha^2 - \tau\xi \frac{[SI]}{[S]}(1 - \phi)\alpha - \tau\xi \frac{N}{n[S]}\phi\alpha^2\delta - \tau\alpha^2\end{aligned}$$

In Section 4.4.2 we considered an epidemic threshold and a condition for stability of the disease-free steady state. In both cases, we consider the state of the system at time zero. At time zero we assume that $[S] = N$, $[SS] = nN$, and $[SI] = 0$, therefore we substitute

these values into the differential equation for α to obtain

$$\begin{aligned}\frac{d\alpha}{dt} &= -\tau\alpha + \tau\xi\frac{nN}{N}(1-\phi)\alpha + \tau\xi\phi\frac{NnN}{nN^2}\alpha^2 - \tau\xi\frac{N}{nN}\phi\alpha^2\delta - \tau\alpha^2 \\ &= -\tau\alpha + \tau\xi n(1-\phi)\alpha + \tau\xi\phi\alpha^2 - \tau\xi\frac{1}{n}\phi\alpha^2\delta - \tau\alpha^2,\end{aligned}$$

where $\xi = \frac{(n-1)}{n}$. Differentiating $\delta = \frac{[II]}{[I]}$ gives

$$\begin{aligned}\frac{d\delta}{dt} &= \frac{[\dot{II}][I] - [II][\dot{I}]}{[I]^2} \\ &= \frac{[II]}{[I]} - \frac{[II][\dot{I}]}{[I]^2},\end{aligned}$$

and substituting $[\dot{II}]$ from equation (4.28) and $[\dot{I}]$ from equation (4.25), we obtain

$$\frac{d\delta}{dt} = 2\tau\frac{[SI]}{[I]} - 2\gamma\frac{[II]}{[I]} + 2\tau\xi\frac{[SI]^2}{[S][I]} \left((1-\phi) + \phi\frac{N[II]}{n[I]^2} \right) - \tau\frac{[SI][II]}{[I]^2} + \gamma\frac{[II]}{[I]}.$$

Replacing all $\frac{[SI]}{[I]}$ terms by α and all $\frac{[II]}{[I]}$ terms by δ gives

$$\begin{aligned}\frac{d\delta}{dt} &= 2\tau\alpha - 2\gamma\delta + 2\tau\xi\frac{[SI]}{[S]}\alpha \left((1-\phi) + \phi\frac{N}{n[I]}\delta \right) - \tau\alpha\delta + \gamma\delta \\ &= 2\tau\alpha - \gamma\delta + 2\tau\xi\frac{[SI]}{[S]}\alpha \left((1-\phi) + \phi\frac{N}{n[I]}\delta \right) - \tau\alpha\delta \\ &= 2\tau\alpha - \gamma\delta + 2\tau\xi\frac{[SI]}{[S]}(1-\phi)\alpha + 2\tau\xi\frac{N[SI]}{n[S][I]}\phi\alpha\delta - \tau\alpha\delta \\ &= 2\tau\alpha - \gamma\delta + 2\tau\xi\frac{[SI]}{[S]}(1-\phi)\alpha + 2\tau\xi\frac{N}{n[S]}\phi\alpha^2\delta - \tau\alpha\delta.\end{aligned}$$

At time zero we assume that $[S] = N$ and $[SI] = 0$. We substitute these values into the differential equation for δ to obtain

$$\frac{d\delta}{dt} = 2\tau\alpha - \gamma\delta + 2\tau\xi\frac{1}{n}\phi\alpha^2\delta - \tau\alpha\delta.$$

Combining the differential equations for both $\alpha = \frac{[SI]}{[I]}$ and $\delta = \frac{[II]}{[I]}$, we have

$$\frac{d\alpha}{dt} = -\tau\alpha + \tau\xi n(1-\phi)\alpha + \tau\xi\phi\alpha^2 - \tau\xi\frac{1}{n}\phi\alpha^2\delta - \tau\alpha^2, \quad (4.74)$$

$$\frac{d\delta}{dt} = 2\tau\alpha - \gamma\delta + 2\tau\xi\frac{1}{n}\phi\alpha^2\delta - \tau\alpha\delta. \quad (4.75)$$

4.B Derivation of evolution equations for the fast variables with the compact improved closure

Using the improved closure (4.23) in line with Proposition 2, which we refer to as the reduced improved closure, we find that

$$[ASI] = (n-1) \left((1-\phi) \frac{[AS][SI]}{n[S]} + \phi \frac{[AS][SI][IA]}{[A] \sum_a [aS][aI]/[a]} \right) \quad (4.76)$$

$$= (n-1) \left((1-\phi) \frac{[AS][SI]}{n[S]} + \phi \frac{[AS][SI][IA]}{[A] \left(\frac{[SS][SI]}{[S]} + \frac{[SI][II]}{[I]} \right)} \right). \quad (4.77)$$

Using equation (4.77) to close the original pairwise equations (4.5)-(4.9), we obtain the following system of equations:

$$[\dot{S}] = -\tau[SI] \quad (4.78)$$

$$[\dot{I}] = \tau[SI] - \gamma[I] \quad (4.79)$$

$$\begin{aligned} [\dot{SI}] = & -(\tau + \gamma)[SI] + \tau(n-1) \left((1-\phi) \frac{[SS][SI]}{n[S]} + \phi \frac{[I][SS][SI]}{[I][SS] + [S][II]} \right) \\ & - \tau(n-1) \left((1-\phi) \frac{[SI]^2}{n[S]} + \phi \frac{[S][SI][II]}{[I][SS] + [S][II]} \right) \end{aligned} \quad (4.80)$$

$$[\dot{SS}] = -2\tau(n-1) \left((1-\phi) \frac{[SS][SI]}{n[S]} + \phi \frac{[I][SS][SI]}{[I][SS] + [S][II]} \right) \quad (4.81)$$

$$[\dot{II}] = 2\tau[SI] - 2\gamma[II] + 2\tau(n-1) \left((1-\phi) \frac{[SI]^2}{n[S]} + \phi \frac{[S][SI][II]}{[I][SS] + [S][II]} \right). \quad (4.82)$$

As we have shown in the main body of the chapter, the computation of the threshold requires a system of differential equations for the fast variables $\alpha = [SI]/[I]$ and $\delta = [II]/[I]$. We find

$$\frac{d\alpha}{dt} = \frac{[\dot{SI}]}{[I]} - \frac{[SI][\dot{I}]}{[I]^2}$$

and substituting $[\dot{SI}]$ from equation (4.80) and $[\dot{I}]$ from equation (4.79), we obtain

$$\begin{aligned} \frac{d\alpha}{dt} = & -(\tau + \gamma) \frac{[SI]}{[I]} + \tau(n-1) \left((1-\phi) \frac{[SS][SI]}{n[S][I]} + \phi \frac{[SS][SI]}{[I][SS] + [S][II]} \right) \\ & - \tau(n-1) \left((1-\phi) \frac{[SI]^2}{n[S][I]} + \phi \frac{[S][SI][II]}{[I]^2[SS] + [S][I][II]} \right) - \tau \frac{[SI]^2}{[I]^2} + \gamma \frac{[SI]}{[I]}. \end{aligned} \quad (4.83)$$

Replacing all $\frac{[SI]}{[I]}$ terms by α and all $\frac{[II]}{[I]}$ terms by δ gives

$$\begin{aligned} \frac{d\alpha}{dt} = & -(\tau + \gamma)\alpha + \tau(n-1) \left((1-\phi) \frac{[SS]}{n[S]} \alpha + \phi \alpha \frac{[SS]}{[SS] + [S]\delta} \right) \\ & - \tau(n-1) \left((1-\phi) \frac{[SI]}{n[S]} \alpha + \phi \alpha \delta \frac{[S]}{[SS] + [S]\delta} \right) - \tau\alpha^2 + \gamma\alpha, \end{aligned} \quad (4.84)$$

and evaluating $\frac{d\alpha}{dt}$ at the disease-free steady state $([S], [I], [SI], [SS], [II]) = (N, 0, 0, nN, 0)$ (4.93) gives

$$\begin{aligned} \frac{d\alpha}{dt} = & -(\tau + \gamma)\alpha + \tau(n-1) \left((1-\phi)\alpha + \phi \alpha \frac{nN}{nN + N\delta} \right) \\ & - \tau(n-1) \left(\phi \alpha \delta \frac{N}{nN + N\delta} \right) - \tau\alpha^2 + \gamma\alpha. \end{aligned} \quad (4.85)$$

After simplification we find that

$$\frac{d\alpha}{dt} = -\tau\alpha + \tau(n-1) \left((1-\phi)\alpha + \phi \alpha \frac{n}{n+\delta} - \phi \alpha \delta \frac{1}{n+\delta} \right) - \tau\alpha^2 \quad (4.86)$$

$$= -\tau\alpha + \tau(n-1) \left((1-\phi)\alpha + \phi \alpha \left(\frac{n-\delta}{n+\delta} \right) \right) - \tau\alpha^2. \quad (4.87)$$

Differentiating $\delta = \frac{[II]}{[I]}$ gives

$$\frac{d\delta}{dt} = \frac{[\dot{II}]}{[I]} - \frac{[II][\dot{I}]}{[I]^2},$$

and substituting $[\dot{II}]$ from equation (4.82) and $[\dot{I}]$ from equation (4.79), we obtain

$$\begin{aligned} \frac{d\delta}{dt} = & 2\tau \frac{[SI]}{[I]} - 2\gamma \frac{[II]}{[I]} + 2\tau(n-1) \left((1-\phi) \frac{[SI]^2}{n[S][I]} + \phi \frac{[S][SI][II]}{[I]^2[SS] + [S][I][II]} \right) \\ & - \tau \frac{[SI][II]}{[I]^2} + \gamma \frac{[II]}{[I]}. \end{aligned} \quad (4.88)$$

Replacing all $\frac{[SI]}{[I]}$ terms by α and all $\frac{[II]}{[I]}$ terms by δ gives

$$\begin{aligned} \frac{d\delta}{dt} = & 2\tau\alpha - 2\gamma\delta + 2\tau(n-1) \left((1-\phi) \frac{[SI]}{n[S]} \alpha + \phi \alpha \delta \frac{[S]}{[SS] + [S]\delta} \right) - \tau\alpha\delta + \gamma\delta \\ = & 2\tau\alpha - \gamma\delta + 2\tau(n-1) \left((1-\phi) \frac{[SI]}{n[S]} \alpha + \phi \alpha \delta \frac{[S]}{[SS] + [S]\delta} \right) - \tau\alpha\delta, \end{aligned}$$

and evaluating $\frac{d\delta}{dt}$ at the disease-free steady state (4.93) gives

$$\frac{d\delta}{dt} = 2\tau\alpha - \gamma\delta + 2\tau(n-1) \left(\phi \alpha \delta \frac{N}{nN + N\delta} \right) - \tau\alpha\delta \quad (4.89)$$

$$= 2\tau\alpha - \gamma\delta + 2\tau(n-1) \left(\phi \alpha \delta \frac{1}{n+\delta} \right) - \tau\alpha\delta. \quad (4.90)$$

Combining the differential equations for both $\alpha = \frac{[SI]}{[I]}$ and $\delta = \frac{[II]}{[I]}$, we have

$$\frac{d\alpha}{dt} = -\tau\alpha + \tau(n-1) \left((1-\phi)\alpha + \phi\alpha \left(\frac{n-\delta}{n+\delta} \right) \right) - \tau\alpha^2 \quad (4.91)$$

$$\frac{d\delta}{dt} = 2\tau\alpha - \gamma\delta + 2\tau(n-1) \left(\frac{\phi\alpha\delta}{n+\delta} \right) - \tau\alpha\delta. \quad (4.92)$$

4.C Standard linear stability analysis for the case of the simple closure

An alternative way to determine the epidemic threshold is to consider the stability of the disease-free steady state

$$([S], [I], [SI], [SS], [II]) = (N, 0, 0, nN, 0). \quad (4.93)$$

When the disease-free steady state is stable, the system will always end up at the disease-free steady state and thus no epidemic will occur. When the disease-free steady state becomes unstable, there exists (at least) a second steady state whereby an epidemic will occur and $[S]$ will no longer be equal to N . To determine a stability condition for the disease-free steady state (4.93), we must compute the Jacobian matrix J of the system (4.24)-(4.28), evaluated at the disease-free steady state, and solve to find its eigenvalues.

By computing partial derivatives of each differential equation (4.24)-(4.28) with respect to each model variable $[S]$, $[I]$, $[SI]$, $[SS]$ and $[II]$, and evaluating each expression at the disease-free steady state (4.93), we obtain

$$J_{df} = \begin{pmatrix} 0 & 0 & -\tau & 0 & 0 \\ 0 & -\gamma & \tau & 0 & 0 \\ 0 & \frac{\partial[SI]}{\partial[I]} & \frac{\partial[SI]}{\partial[SI]} & 0 & \frac{\partial[SI]}{\partial[II]} \\ 0 & \frac{\partial[SS]}{\partial[I]} & \frac{\partial[SS]}{\partial[SI]} & 0 & 0 \\ 0 & \frac{\partial[II]}{\partial[I]} & \frac{\partial[II]}{\partial[SI]} & 0 & \frac{\partial[II]}{\partial[II]} \end{pmatrix}, \quad (4.94)$$

with $\frac{\partial[SI]}{\partial[I]} = \tau\xi\phi \left(\frac{2[SI]^2[II]}{n[I]^3} - \frac{[SI]^2}{[I]^2} \right)$, $\frac{\partial[SI]}{\partial[SI]} = -(\tau + \gamma) + \tau\xi(1-\phi)n + 2\tau\xi\phi \left(\frac{[SI]}{[I]} - \frac{[SI][II]}{n[I]^2} \right)$, $\frac{\partial[SI]}{\partial[II]} = -\tau\xi\phi \frac{[SI]^2}{n[I]^2}$, $\frac{\partial[SS]}{\partial[I]} = 2\tau\xi\phi \frac{[SI]^2}{[I]^2}$, $\frac{\partial[SS]}{\partial[SI]} = -2\tau\xi(1-\phi)n - 4\tau\xi\phi \frac{[SI]}{[I]}$, $\frac{\partial[II]}{\partial[I]} = -4\tau\xi\phi \frac{[SI]^2[II]}{n[I]^3}$, $\frac{\partial[II]}{\partial[SI]} = 2\tau + 4\tau\xi\phi \frac{[SI][II]}{n[I]^2}$ and $\frac{\partial[II]}{\partial[II]} = -2\gamma + 2\tau\xi\phi \frac{[SI]^2}{n[I]^2}$ all containing variables $\frac{[SI]}{[I]}$ and $\frac{[II]}{[I]}$.

The zero entries in J_{df} reflect the true values that the respective partial derivatives attain at the disease-free equilibrium. However, the majority of the non-zero matrix entries involve $\frac{[SI]}{[I]}$ and $\frac{[II]}{[I]}$. Since $[I] = [SI] = [II] = 0$ at the disease-free steady state, both of

these quantities are ill-defined. Hence, not all entries of the Jacobian can be evaluated at the equilibrium. This issue prevents the computation of the eigenvalues of J_{df} and thus the value of the epidemic threshold. In order to progress, we need to determine the correct values for $\alpha = \frac{[SI]}{[I]}$ and $\delta = \frac{[II]}{[I]}$. We note that the correct value of $\alpha = \frac{[SI]}{[I]}$ is also required in equation (4.33), and the threshold cannot be computed without it.

In fact, using only $\phi = 0$, the Jacobian at the disease-free steady state (4.93) becomes

$$J_{df_no_clust} = \begin{pmatrix} 0 & 0 & -\tau & 0 & 0 \\ 0 & -\gamma & \tau & 0 & 0 \\ 0 & 0 & -\gamma + \tau(n-2) & 0 & 0 \\ 0 & 0 & -2\tau(n-1) & 0 & 0 \\ 0 & 0 & 2\tau & 0 & -2\gamma \end{pmatrix}. \quad (4.95)$$

It is straightforward to show that the eigenvalues are given by $\lambda_1 = 0$, $\lambda_2 = -\gamma$, $\lambda_3 = \tau(n-2) - \gamma$, $\lambda_4 = 0$ and $\lambda_5 = -2\gamma$. The only eigenvalue that can be non-zero and non-negative is $\lambda_3 = \tau(n-2) - \gamma$. Hence, we know that the disease-free steady state (4.93) is stable when $\lambda_3 \leq 0$ and becomes unstable when $\lambda_3 > 0$. Thus, the epidemic threshold is given by $\lambda_3 = 0$ and this can be rearranged to give $\tau(n-2)/\gamma = 1$. This is equivalent to the calculation based on determining the quasi-equilibrium of the fast variables.

4.D Standard linear stability analysis for the case of the compact improved closure

To determine an epidemic threshold, we consider conditions for stability of the disease-free steady state (4.93). To do so, we compute the Jacobian matrix evaluated at the disease-free steady state as

$$J_{df_2} = \begin{pmatrix} 0 & 0 & -\tau & 0 & 0 \\ 0 & -\gamma & \tau & 0 & 0 \\ 0 & \frac{\partial[SI]}{\partial[I]} & \frac{\partial[SI]}{\partial[SI]} & 0 & \frac{\partial[SI]}{\partial[II]} \\ 0 & \frac{\partial[SS]}{\partial[I]} & \frac{\partial[SS]}{\partial[SI]} & 0 & \frac{\partial[SS]}{\partial[II]} \\ 0 & \frac{\partial[II]}{\partial[I]} & \frac{\partial[II]}{\partial[SI]} & 0 & \frac{\partial[II]}{\partial[II]} \end{pmatrix} \quad (4.96)$$

where $\frac{\partial[SI]}{\partial[I]} = 2\tau(n-1)\phi\alpha\delta\frac{n}{n^2+2n\delta+\delta^2}$, $\frac{\partial[SI]}{\partial[SI]} = -(\tau + \gamma) + \tau(n-1)\left((1-\phi) + \phi\left(\frac{n-\delta}{n+\delta}\right)\right)$, $\frac{\partial[SI]}{\partial[II]} = -2\tau(n-1)\left(\phi\alpha\delta\frac{n}{n^2+2n\delta+\delta^2}\right)$, $\frac{\partial[SS]}{\partial[I]} = -2\tau(n-1)\left((1-\phi) + \phi\frac{n}{n+\delta}\right)$, $\frac{\partial[SS]}{\partial[SI]} = 2\tau(n-1)\left(\phi\alpha\delta\frac{n}{n^2+2n\delta+\delta^2}\right)$, $\frac{\partial[II]}{\partial[I]} = -2\tau(n-1)\left(\phi\alpha\delta\frac{n}{n^2+2n\delta+\delta^2}\right)$,

$\frac{\partial[\dot{II}]}{\partial[SI]} = 2\tau + 2\tau(n-1) \left(\phi \delta \frac{1}{n+\delta} \right)$ and $\frac{\partial[\dot{II}]}{\partial[II]} = -2\gamma + 2\tau(n-1) \left(\phi \alpha \frac{n}{n^2 + 2n\delta + \delta^2} \right)$ cannot be fully evaluated as they contain products of the problematic variables $\alpha = \frac{[SI]}{[I]}$ and $\delta = \frac{[II]}{[I]}$.

The Jacobian (4.96) becomes useful once analytic expressions for α and δ are obtained (or it could be approximate values obtained via an asymptotic expansion or even numerical values). Plugging these values into the Jacobian (4.96) will allow either numerical or analytical computation of the threshold. We note that using linear-stability analysis or focusing on the initial growth rate should lead to the same threshold value, as was shown previously for the case of the system with the simple closure, see Section 4.C.

Chapter 5

Discussion

In this thesis, I have presented three pieces of research, contained in Chapters 2-4, which consider dynamic processes occurring on complex structured networks. A key theme considered in all three pieces of research is the influence of local spatial or network structure on the dynamic process(es) being modelled on a global scale. The first piece of research, in Chapter 2, considers a neuroscience-based model describing the activity-dependent growth and development of a network of excitatory and inhibitory neurons embedded in space. The second and third pieces of research, in Chapters 3 and 4 respectively, consider models tracking the SIR epidemic spreading on complex networks. Here, I will summarise the research and results presented in Chapters 2-4, as well as considering potential improvements to each piece of work. I will also discuss the implications of the results presented and consider ideas for future research, as well as interesting open questions related to the research of complex systems.

In Chapter 2, the model allows for a dual-direction interaction between the network's structure and the dynamic process being modelled, namely the electrical activity of the neurons. In this model, there exists a feedback loop whereby structure influences electrical activity, and electrical activity influences structure, as illustrated by the feedback loop in Figure 1.2. This process occurs until a system steady state can be reached whereby all neurons achieve a desired level of electrical activity simultaneously. In Chapter 3, the network consists of a static and a dynamic network layer whose structures influence the SIR epidemic process. In Chapter 4, the network consists of a single, fully static network layer which also influences the process of the SIR epidemic. However, in both Chapter 3 and Chapter 4, the SIR epidemic process cannot influence the network's structure, and therefore only a one-way interaction between structure and the dynamic process being modelled is considered in these cases.

5.1 Summarising the work presented in Chapter 2

In Chapter 2, we consider the effects of local spatial structure on a published model [119] describing the activity-dependent growth and development of a network of excitatory and inhibitory neurons embedded in space. We introduce the model, outlining its equations and parameters, and we discuss the implementation of growth simulations including detailing the choices made regarding initial conditions, model parameters and spatial arrangements of excitatory and inhibitory neurons. We hypothesised that the spatial arrangement of neurons would be an important factor in determining global outcome and thus derived novel measures for inhibitory clustering within one- and two-dimensional lattice networks with periodic boundary conditions.

We performed various tests and analyses on growth simulations of one- and two-dimensional arrangements of excitatory and inhibitory neurons within lattice networks exhibiting periodic boundary conditions. Considering one-dimensional arrangements of neurons, we demonstrated that the proportion of inhibitory neurons in a system cannot accurately predict global outcome, by showing that systems with distinct neuron arrangements but identical proportions of inhibitory neurons can exhibit qualitatively distinct behaviours.

By considering an exhaustive list of one-dimensional arrangements of neurons, and recording the behavioural outcome against the associated inhibitory clustering measure (2.8), we demonstrate that, in one-dimensional lattice networks, arrangements with highest inhibitory clustering exhibit the most extreme oscillatory dynamics. We observe an idiosyncratic outcome of the model where neurons are unable to achieve the desired electrical activity, and neurite outgrowth continues indefinitely. The global outcomes observed in one-dimensional examples are characterised as stabilisation, stable oscillatory, unstable oscillatory and unbounded growth behaviour types. We conclude that stabilisation of electrical activity and network structure occurs most often when inhibitory neurons are evenly distributed onto lattice positions. We map the relationship between the proportion of inhibitory neurons in the system and the extent of inhibitory clustering within each network, recording the behavioural outcome in each case.

Further, we considered one-dimensional networks comprised of multiple excitatory and inhibitory clusters of neurons. This was done by considering adjacent repeats of one-dimensional networks containing contiguous arrangements of excitatory and inhibitory neurons. In this case, we investigated what proportions of inhibitory neurons were likely to result in specific behavioural outcomes. We found that networks with proportions

of inhibition below 20% exhibited stabilisation, proportions of inhibition in the range [20%, 50%] induced oscillatory behaviours, and proportions of inhibition above 50% induced unbounded growth. Finally, we investigated what network attributes characterised each behavioural outcome observed.

In two-dimensional lattice networks, we considered growth simulations of various spatial arrangements of neurons and observed two behaviour types: complete stabilisation of electrical activity and network structure, and stable oscillatory behaviour of electrical activity and neuritic radii. Oscillatory neuron arrangements generally had a higher two-dimensional inhibitory clustering measure (2.9) than arrangements which reached equilibrium. However, after considering a simplification of the originally proposed measure for inhibitory clustering in two-dimensional lattice networks, we found a clearer relationship between outcome and extent of inhibitory clustering, reinforcing the conclusion that inhibitory clustering can induce oscillatory behaviours.

Other than finding that increased inhibitory clustering induces oscillatory behaviour, we concluded that global behavioural dynamics rely on the balance between excitation and inhibition, as well as the arrangement of neurons and the initial conditions of the system. Increased inhibitory clustering was also found to induce emerging segregation between excitation and inhibition, in the form of excitatory neurons with high degrees, which were hypothesised to be responsible for long-range communication within the network. Further, we concluded that instability was most evident in one-dimensional networks, whilst two-dimensional network outcomes tended to be more stable. It was hypothesised that networks in higher dimensions might protect against the emergence of the most pathological behaviours. Finally, our findings reinforced the idea that networks with higher levels of inhibition are more likely to experience oscillatory dynamics.

We have identified a number of improvements that can be made to the work in Chapter 2, including considering the activity-dependent model in three-dimensions and deriving an associated measure for inhibitory clustering within three-dimensional lattice networks. Further, improvements can be made to both the one- and two-dimensional inhibitory clustering measures (2.8)-(2.9), in order to improve their sensitivity in relation to the extent of clustering and behavioural outcome. A number of tests and analyses can be repeated with a finer grain level of detail, allowing for stronger conclusions to be drawn regarding the relationship between the proportion of inhibition, the spatial arrangement of neurons, initial conditions and behavioural outcome. Network analysis was performed in one-dimensional examples only, and another extension of this work would involve performing the same

type of analysis on two- and three-dimensional network examples. Finally, we identified that the model itself can be altered to consider more realistic scenarios, such as for the arrangement of neurons onto specific locations as opposed to being restricted to lattice positions, and the consideration of various synapse formation rules.

The results of the research presented in Chapter 2 reinforce some existing ideas regarding the influence of neural inhibition, whilst highlighting the previously under-examined effect of the spatial arrangement of neurons, and specifically the clustering of inhibitory neurons. We suggest that future modelling studies such as this one should consider both the number and arrangement of neurons, and should be careful when attributing particular dynamic properties to the ratio between excitation and inhibition. Further, work is required to develop tractable mathematical models that afford consideration of distinct neuron types within structured networks. One such example, which was discovered by the authors following publication of the work in Chapter 2, considers the dynamics of recurrent cortical networks containing excitatory and multiple subtypes of inhibitory neurons, investigating how perturbations of distinct neuronal subtypes recruits changes in activity through recurrent synaptic projections, and concluding that “recurrent inhibitory dynamics must be taken into account to fully understand many properties of cortical dynamics observed in experiments” [64].

From an experimental perspective, future work should focus on the detection and classification of inhibitory and/or excitatory neuron clusters in vivo, as well as into the exploration of their role in network pathology. Experiments can be performed to determine how inhibition of inhibition affects network development and behaviour and to design treatments that focus on neural inhibition as a target for inducing favourable network remodelling in patients experiencing pathological network activity. Some of the key questions we should be asking in the future include: i) *how is dynamic network stability achieved and maintained in the brain?*, ii) *how do different neuron subtypes and distinct arrangements of these different neuron subtypes affect outcome?* and iii) *how can we utilise our knowledge of neuron subtypes and arrangements and their effect on global outcome to design effective treatments for pathological neural activity?*

5.2 Summarising the work presented in Chapter 3

In Chapter 3, we have extended the existing modelling framework by deriving a series of model equations that accurately describe the SIR epidemic process, following the edge-based compartmental modelling approach [124, 73, 74, 77]. The epidemic occurs on a

complex multiplex network of N individuals, comprised of two distinct network layers. The first network layer remains static in time and is generated using two edge distributions, in order to achieve varying levels of clustering. The second network layer is dynamic in time, with all pairs of edges rewiring at a constant rate, and is generated using a single edge distribution. Each network layer is intended to describe distinct *types* of connections an individual makes with other population members. This work combines two previous edge-based compartmental models on uniplex networks [125, 77], generating a model which considers the SIR epidemic occurring on a complex network containing both static and dynamic network architecture.

The multiplex model's equations were validated by i) testing their convergence towards the dynamics of each pre-existing uniplex model when either the static or dynamic network elements were tending towards zero and ii) comparing their predictions against the dynamics of simulated SIR epidemics occurring on real networks generated according to equivalent parameter values. The multiple model's parameter space was explored by testing various combinations of model parameters and recording the outcome of the epidemic process.

To determine an expression for the basic reproduction number, we utilised the next generation matrix approach [20], generating a square matrix containing values representing the average number of infections caused across each type of edge, when the original infection was received across each type of edge. Here, the next generation matrix (3.24) is comprised of 9 values, since the multiplex model is generated using three types of edges. The basic reproduction number is calculated as the leading eigenvalue of the next generation matrix. The expression derived for the basic reproduction number was validated by checking that the final epidemic size was perturbed as the associated value of the basic reproduction number exceeded the epidemic threshold. The effect on the basic reproduction number of varying parameters and rates describing rewiring, clustering and average degree was also explored.

Following the edge-based compartmental modelling approach enabled us to derive a fixed number of equations that are able to predict the outcome of an SIR epidemic on a complex network of N individuals. These equations afford a huge reduction in the cost of making such predictions, when compared to the cost of making predictions via fully simulated epidemic processes. The model captures more complexity in network structure than previous modelling attempts and the work itself provides a concise illustration of model design, derivation, implementation and testing. We have further demonstrated the

utility of the edge-based compartmental modelling approach in capturing and describing complexity when modelling epidemics on networks and we hope that this work encourages future researchers to improve on current models, modelling approaches and analysis techniques.

We identified a number of potential extensions and improvements to the work presented in Chapter 3. Potential improvements to the model include: embedding the N individuals in space, considering weighted network connections, allowing for flux in and out of the population, considering more realistic rules for edge rewiring events and generating the dynamic network layer using two edge distributions to allow for tunable clustering on both network layers. Regarding the implementation and analysis of the model, we identified many unexplored areas, such as a comprehensive exploration of the entire parameter space and tests and analyses of various edge distributions and their effect on global outcome. Furthermore, the model's predictions can be tested using historic data from real-world epidemics.

In the future, research continuing along the themes we have explored in Chapter 3 should consider quantifying the various heterogeneities observed within existing populations, investigating how observed heterogeneous features influence disease spreading dynamics, searching out clear relationships or dependencies between population features and global outcome and designing and testing mechanisms or approaches with the aim of controlling disease spread. Further, there is an endless need for research that improves on existing models, modelling approaches and analytical techniques, especially as computational capabilities continue to improve. Pertinent questions arising from this research include: *how much complexity do we need to consider in our models in order to gain useful insights?* and *how can we utilise current mathematical models to reduce the severity of future disease outbreaks?*

5.3 Summarising the work presented in Chapter 4

In Chapter 4, we extend the analytical framework by utilising a unique approach to considering the epidemic threshold for pairwise model equations describing an SIR epidemic spreading through a clustered, regular network of N individuals. We begin by outlining the network-based formalism, SIR disease dynamics and the unclosed pairwise model equations describing the dynamics in time of the SIR epidemic process. We outline the motivation behind and the derivation of relevant closures for the model, including the two closures for clustered networks considered within the chapter.

Firstly, we consider the clustered pairwise model with the simple closure. We utilise the simple closure to express the full, closed model equations. We summarise pre-existing results [54] that derive a growth-rate-based expression for the epidemic threshold by utilising the correlation factor C_{SI} , which describes the propensity for nodes of type S and I to be neighbouring nodes in the network. We then provide an alternative approach to deriving an expression for the epidemic threshold, by utilising two variables $\alpha = \frac{[SI]}{[I]}$ and $\delta = \frac{[II]}{[I]}$ which are shown to converge to quasi-equilibrium values much faster than the epidemic process converges itself. We calculate differential equations for both fast variables α and δ , and aim to determine steady state values for both variables that would uncover the epidemic threshold expression.

When clustering is negligible, we find that the differential equations for α and δ can be solved easily to find steady state values, and we use these to determine the associated epidemic threshold. When clustering is present in the network, the differential equations for α and δ are far more complex, and trying to determine steady state values leads to a single cubic equation in terms of the variable α . We demonstrate that the roots of the cubic equation can be determined by utilising an asymptotic expansion of the solution in powers of the clustering coefficient ϕ . This approach leads to an estimate of the root of the cubic equation which is used to determine the epidemic threshold.

The epidemic threshold based on the asymptotic expansion of the root of the cubic equation in α is tested and validated by comparing its value to the epidemic threshold generated via the numerical solution to the cubic equation in α and to the epidemic threshold generated by solving numerically the full system of pairwise ODEs.

Additionally, we consider the clustered pairwise model with the compact improved closure, an adjustment of the improved closure which assumes that the number of nodes in the recovered state is negligible. This adjustment enables us to utilise the same approach to determining an epidemic threshold expression as was used for the pairwise model with the simple closure. Namely, we use the compact improved closure to express the full system of pairwise model equations and compute another system of differential equations involving the fast variables $\alpha = \frac{[SI]}{[I]}$ and $\delta = \frac{[II]}{[I]}$. We identify the trivial $(0,0)$ steady state by observing the differential equations for α and δ . However, in order to identify a non-trivial steady state expression, we rearrange the differential equations set equal to zero, resulting in another cubic equation in terms of the δ variable. Once again, we approximate the root of the cubic equation in δ via an asymptotic expansion of the root in powers of the clustering coefficient ϕ . This approximated root leads to an equivalent

approximated epidemic threshold for the pairwise model with the compact improved closure. The epidemic threshold for the clustered pairwise model with the compact improved closure, generated via the asymptotic expansion, is tested and validated by comparing its predictions to the threshold generated by solving numerically the cubic equation in δ and to the final epidemic size generated by solving the full system of pairwise ODEs.

We conclude the work by summarising the results presented and by making comparisons with the findings of research using differing approaches to deriving epidemic threshold expressions for clustered networks. We highlight potential extensions of the work, including testing our epidemic threshold expressions against explicit stochastic network simulations, investigating analytically the ODE systems for the fast variables α and δ and analysing the pairwise model with the full improved closure, i.e. without using Proposition 2. Further, we suggest that future research should utilise and compare different models in order to identify systematically the impact of clustering on epidemic spread and should make comparisons between the true basic reproduction number R_0 , which can be computed in various ways including using the next generation matrix approach [20], and epidemic threshold expressions derived by other means in order to reconcile different methods and improve the analytical approaches used. In Appendices 4.A and 4.B we provide detailed calculations of the differential equations for the fast variables α and δ and Appendices 4.C and 4.D contain standard linear-stability analysis of the disease-free steady state for each of the pairwise models considered, an alternative method of deriving a threshold condition. This work is likely to inform and improve future modelling and analysis techniques in mathematical epidemiology. It also provokes interesting questions such as: *how can we optimise and improve on current analytical techniques used on network models?*, *which epidemic descriptors provide us with the most insight?* and *how can we test systematically the performance of various epidemic descriptors currently used?*

5.4 Implications of the work & future research

In the work presented within this thesis, we have considered three mathematical models describing neuronal and epidemiological processes occurring within structured networks. There are a number of implications which arise after considering each of these modelling studies. For neuroscience, the finding in Chapter 2 that increased inhibitory clustering increases the likelihood of oscillatory behaviour in a model describing the activity-dependent development of a network of neurons highlights the importance of the *spatial arrangement* of the various types of neurons observed in the brain on behavioural outcome. For epi-

demology, the work in Chapters 3 and 4 highlights the importance of considering the *heterogeneous nature of connections* within complex networks and how they can influence disease spreading dynamics. Further, all three pieces of research reinforce the importance of developing improved models and modelling and analysis techniques.

There are numerous implications which are relevant to both neuroscience, epidemiology, and many other fields. In Chapter 2 the locations of the neurons (or nodes) are embedded in space, whereas Chapters 3 and 4 consider heterogeneous structural connections between individuals but do not embed node locations in space. An obvious next step would be to make direct comparisons between these network models with and without spatial embedding, investigating what changes occur to the process(es) being modelled.

Further, there are numerous implications to consider when modelling the influence of network structure on dynamical processes. Models that capture more complexity are required, meaning that simpler models which rely on unifying assumptions, such as mean-field model equations, cannot always capture the important effects to be investigated. However, as models become more complex, it becomes more difficult to communicate and pass on knowledge regarding the model and results of the model. In many modelling situations there are so many interacting factors that it is challenging to determine causality. There may also be a limit to the complexity of structure that can be considered in order for the model to be analytically tractable. A central question for modellers to ask themselves is when to stop incorporating additional complexity into models and assume that enough features have been considered to capture the important dynamics.

Another issue to consider is that there may already exist novel techniques and methods that can consider such complexity but are yet to have been discovered or utilised in the correct way. This highlights the difficulty in seeing and predicting that which we do not already know. On the other hand, we may be at the limit of what current mathematical techniques offer us to deal with complexity. These implications provoke other questions such as: *is there a unifying structural descriptor that captures sufficient complexity but allows for simple modelling?* For example, *does the clustering coefficient describe enough complexity or do we need to utilise additional structural descriptors?* Further, *will increasing computational power eventually mean that we can model all of the structural features we observe in complex networks?* Overall, research must continue to tread a careful balance between homogeneity and heterogeneity in complex network models. Some unifying assumptions will be acceptable, and in some cases will be necessary, whereas others assumptions must be neglected in order to investigate the effects of certain heterogeneities.

5.5 Final remarks

I believe that complex networks research offers and will continue to offer unrivalled insight into the complex systems and processes that occur around us in the real world. It is clear that the graph or network theory formalism can be used to describe complex systems in every corner of our existence and beyond, from the atomistic level all the way to describing the structure of the universe itself. Further, the underlying formalism of complex networks, namely graph theory in mathematics, provides a modelling and analysis framework that is beautiful, visual, universal and easily understood. For example, regardless of language spoken, two individuals from different cultures can communicate and understand the same idea via a simple drawing of a network or graph. Further, even within the same spoken language, the network theory formalism can be easily understood by researchers coming from completely different backgrounds. Effectively, network theory can be used as a form of communication. The ease of communication surrounding network theory will provoke cross-fertilisation and academic competition that will inevitably move the state of the art (or science!) forwards.

One drawback of the network theory formalism is that there exists some confusing and/or overlapping terminology. For example, multilayer versus multiplex networks and coevolutionary versus adaptive networks. One would argue that the global research community should agree upon a single list of terminology and definitions in order to facilitate communication and collaboration between researchers and to maximise the output from network-based research.

Regardless of the terminology and metrics that are used to describe complex networks and their features, the field itself will enable and improve our problem solving capabilities. With ever-increasing computational power, we will have the ability to study larger, more complex and more heterogeneous systems, as well as considering more complex dynamic processes. Greater computational abilities will also lead to more comprehensive tests and analyses being performed. Considering today's computational capabilities, one might rule out certain exhaustive searches due to the time and computational cost, whereas in ten years the same exhaustive search might be considered a necessity. Notwithstanding increases in computational ability, it is the progress of individual women and men across the globe doing research that will inevitably lead to better insight and greater analytical prowess, and it is my hope that this work inspires them.

Bibliography

- [1] Lada A Adamic and Natalie Glance. The political blogosphere and the 2004 us election: divided they blog. In *Proceedings of the 3rd international workshop on Link discovery*, pages 36–43. ACM, 2005. [1](#)
- [2] Eugenius SBC Ang, Tarik F Haydar, Vicko Gluncic, and Pasko Rakic. Four-dimensional migratory coordinates of GABAergic interneurons in the developing mouse cortex. *Journal of Neuroscience*, 23(13):5805–5815, 2003. [12](#)
- [3] Ronan F Arthur, Emily S Gurley, Henrik Salje, Laura SP Bloomfield, and James H Jones. Contact structure, mobility, environmental impact and behaviour: the importance of social forces to infectious disease dynamics and disease ecology. *Phil. Trans. R. Soc. B*, 372(1719):20160454, 2017. [47](#)
- [4] Frank Ball, Denis Mollison, and Gianpaolo Scalia-Tomba. Epidemics with two levels of mixing. *The Annals of Applied Probability*, pages 46–89, 1997. [82](#)
- [5] Justin Balthrop, Stephanie Forrest, Mark EJ Newman, and Matthew M Williamson. Technological networks and the spread of computer viruses. *Science*, 304(5670):527–529, 2004. [2](#)
- [6] Marc Barthélemy. Spatial networks. *Physics Reports*, 499(1):1–101, 2011. [82](#)
- [7] Michael Boss, Helmut Elsinger, Martin Summer, and Stefan Thurner 4. Network topology of the interbank market. *Quantitative finance*, 4(6):677–684, 2004. [1](#)
- [8] Keith N Brown, She Chen, Zhi Han, Chun-Hui Lu, Xin Tan, Xin-Jun Zhang, Liya Ding, Alejandro Lopez-Cruz, Dieter Saur, Stewart A Anderson, et al. Clonal production and organization of inhibitory interneurons in the neocortex. *Science*, 334(6055):480–486, 2011. [13](#), [44](#)
- [9] Charles D Brummitt, Kyu-Min Lee, and K-I Goh. Multiplexity-facilitated cascades in networks. *Physical Review E*, 85(4):045102, 2012. [48](#)

- [10] Ed Bullmore and Olaf Sporns. Complex brain networks: graph theoretical analysis of structural and functional systems. *Nature Reviews Neuroscience*, 10(3):186, 2009. [13](#)
- [11] Anthony N Burkitt. A review of the integrate-and-fire neuron model: I. homogeneous synaptic input. *Biological cybernetics*, 95(1):1–19, 2006. [7](#)
- [12] Anthony N Burkitt. A review of the integrate-and-fire neuron model: Ii. inhomogeneous synaptic input and network properties. *Biological cybernetics*, 95(2):97–112, 2006. [7](#)
- [13] Markus Butz and Arjen van Ooyen. A simple rule for dendritic spine and axonal bouton formation can account for cortical reorganization after focal retinal lesions. *PLoS computational biology*, 9(10):e1003259, 2013. [44](#)
- [14] E Cator and P Van Mieghem. Nodal infection in markovian susceptible-infected-susceptible and susceptible-infected-removed epidemics on networks are non-negatively correlated. *Physical Review E*, 89(5):052802, 2014. [92](#)
- [15] Gabriele Ciceri, Nathalie Dehorter, Ignasi Sols, Z Josh Huang, Miguel Maravall, and Oscar Marín. Lineage-specific laminar organization of cortical GABAergic interneurons. *Nature neuroscience*, 16(9):1199, 2013. [13](#), [44](#)
- [16] Christopher S Cohan and Stanley B Kater. Suppression of neurite elongation and growth cone motility by electrical activity. *Science*, 232(4758):1638–1640, 1986. [11](#)
- [17] Emanuele Cozzo, Raquel A Banos, Sandro Meloni, and Yamir Moreno. Contact-based social contagion in multiplex networks. *Physical Review E*, 88(5):050801, 2013. [48](#)
- [18] Laurent Decreusefond, Jean-Stéphane Dherisin, Pascal Moyal, Viet Chi Tran, et al. Large graph limit for an SIR process in random network with heterogeneous connectivity. *The Annals of Applied Probability*, 22(2):541–575, 2012. [96](#)
- [19] Marina Diakonova, Vincenzo Nicosia, Vito Latora, and Maxi San Miguel. Irreducibility of multilayer network dynamics: the case of the voter model. *New Journal of Physics*, 18(2):023010, 2016. [48](#)
- [20] O Diekmann, JAP Heesterbeek, and MG Roberts. The construction of next-generation matrices for compartmental epidemic models. *Journal of the Royal Society Interface*, page rsif20090386, 2009. [50](#), [61](#), [80](#), [124](#), [127](#)

- [21] Wei Dong and Carlos D Aizenman. A competition-based mechanism mediates developmental refinement of tectal neuron receptive fields. *Journal of Neuroscience*, 32(47):16872–16879, 2012. 12, 45
- [22] Ken TD Eames. Modelling disease spread through random and regular contacts in clustered populations. *Theoretical population biology*, 73(1):104–111, 2008. 88, 97
- [23] Ken TD Eames and Matt J Keeling. Modeling dynamic and network heterogeneities in the spread of sexually transmitted diseases. *Proceedings of the National Academy of Sciences*, 99(20):13330–13335, 2002. 87
- [24] Daniel Ehrens, Duluxan Sritharan, and Sridevi V Sarma. Closed-loop control of a fragile network: application to seizure-like dynamics of an epilepsy model. *Frontiers in neuroscience*, 9:58, 2015. 39
- [25] I Ferrer, E Soriano, JA Del Rio, S Alcantara, and C Auladell. Cell death and removal in the cerebral cortex during development. *Progress in neurobiology*, 39(1):1–43, 1992. 11
- [26] R Douglas Fields, Elaine A Neale, and Phillip G Nelson. Effects of patterned electrical activity on neurite outgrowth from mouse sensory neurons. *Journal of Neuroscience*, 10(9):2950–2964, 1990. 11
- [27] Robert S Fisher, Walter Van Emde Boas, Warren Blume, Christian Elger, Pierre Genton, Phillip Lee, and Jerome Engel Jr. Epileptic seizures and epilepsy: definitions proposed by the international league against epilepsy (ilae) and the international bureau for epilepsy (ibe). *Epilepsia*, 46(4):470–472, 2005. 6
- [28] Naila Ben Fredj, Sarah Hammond, Hideo Otsuna, Chi-Bin Chien, Juan Burrone, and Martin P Meyer. Synaptic activity and activity-dependent competition regulates axon arbor maturation, growth arrest, and territory in the retinotectal projection. *Journal of Neuroscience*, 30(32):10939–10951, 2010. 45
- [29] Sebastian Funk, Erez Gilad, Chris Watkins, and Vincent AA Jansen. The spread of awareness and its impact on epidemic outbreaks. *Proceedings of the National Academy of Sciences*, 106(16):6872–6877, 2009. 4, 84
- [30] Sebastian Funk, Marcel Salathé, and Vincent AA Jansen. Modelling the influence of human behaviour on the spread of infectious diseases: a review. *Journal of the Royal Society Interface*, page rsif20100142, 2010. 4

- [31] Karunesh Ganguly and Mu-ming Poo. Activity-dependent neural plasticity from bench to bedside. *Neuron*, 80(3):729–741, 2013. [12](#), [45](#)
- [32] Daniel T Gillespie. A general method for numerically simulating the stochastic time evolution of coupled chemical reactions. *Journal of computational physics*, 22(4):403–434, 1976. [50](#), [66](#), [80](#)
- [33] Sergio Gomez, Albert Diaz-Guilera, Jesus Gomez-Gardenes, Conrad J Perez-Vicente, Yamir Moreno, and Alex Arenas. Diffusion dynamics on multiplex networks. *Physical review letters*, 110(2):028701, 2013. [48](#)
- [34] Andrzej Grabowski and RA Kosiński. Ising-based model of opinion formation in a complex network of interpersonal interactions. *Physica A: Statistical Mechanics and its Applications*, 361(2):651–664, 2006. [2](#)
- [35] Clara Granell, Sergio Gómez, and Alex Arenas. Dynamical interplay between awareness and epidemic spreading in multiplex networks. *Physical review letters*, 111(12):128701, 2013. [4](#)
- [36] Thilo Gross and Bernd Blasius. Adaptive coevolutionary networks: a review. *Journal of the Royal Society Interface*, 5(20):259–271, 2008. [xi](#), [3](#), [4](#)
- [37] Thilo Gross, Carlos J Dommar DLima, and Bernd Blasius. Epidemic dynamics on an adaptive network. *Physical review letters*, 96(20):208701, 2006. [87](#)
- [38] Stephen Grossberg. Nonlinear neural networks: Principles, mechanisms, and architectures. *Neural networks*, 1(1):17–61, 1988. [11](#), [14](#)
- [39] Roger Guimera, Stefano Mossa, Adrian Turttschi, and LA Nunes Amaral. The worldwide air transportation network: Anomalous centrality, community structure, and cities’ global roles. *Proceedings of the National Academy of Sciences*, 102(22):7794–7799, 2005. [1](#)
- [40] Bilal Haider, Alvaro Duque, Andrea R Hasenstaub, and David A McCormick. Neocortical network activity in vivo is generated through a dynamic balance of excitation and inhibition. *Journal of Neuroscience*, 26(17):4535–4545, 2006. [12](#)
- [41] Keith B Hengen, Mary E Lambo, Stephen D Van Hooser, Donald B Katz, and Gina G Turrigiano. Firing rate homeostasis in visual cortex of freely behaving rodents. *Neuron*, 80(2):335–342, 2013. [12](#)

- [42] John Henley and Mu-ming Poo. Guiding neuronal growth cones using Ca^{2+} signals. *Trends in cell biology*, 14(6):320–330, 2004. 12
- [43] Cesar A Hidalgo and Carlos Rodriguez-Sickert. The dynamics of a mobile phone network. *Physica A: Statistical Mechanics and its Applications*, 387(12):3017–3024, 2008. 49
- [44] Petter Holme. Three faces of node importance in network epidemiology: Exact results for small graphs. *Physical Review E*, 96(6):062305, 2017. 86
- [45] Thomas House, Geoffrey Davies, Leon Danon, and Matt J Keeling. A motif-based approach to network epidemics. *Bulletin of Mathematical Biology*, 71(7):1693–1706, 2009. 87
- [46] Thomas House and Matt J Keeling. The impact of contact tracing in clustered populations. *PLoS computational biology*, 6(3):e1000721, 2010. 88
- [47] Karly A Jacobsen, Mark G Burch, Joseph H Tien, and Grzegorz A Rempała. The large graph limit of a stochastic epidemic model on a dynamic multilayer network. *arXiv preprint arXiv:1605.02809*, 2016. 48, 82, 83
- [48] Svante Janson, Malwina Luczak, and Peter Windridge. Law of large numbers for the SIR epidemic on a random graph with given degrees. *Random Structures & Algorithms*, 45(4):726–763, 2014. 96
- [49] Hawoong Jeong, Bálint Tombor, Réka Albert, Zoltan N Oltvai, and A-L Barabási. The large-scale organization of metabolic networks. *Nature*, 407(6804):651, 2000. 1
- [50] Xiaolong Jiang, Guangfu Wang, Alice J Lee, Ruth L Stornetta, and J Julius Zhu. The organization of two new cortical interneuronal circuits. *Nature neuroscience*, 16(2):210, 2013. 44
- [51] Brian Karrer and Mark EJ Newman. Message passing approach for general epidemic models. *Physical Review E*, 82(1):016101, 2010. 86
- [52] Brian Karrer and Mark EJ Newman. Random graphs containing arbitrary distributions of subgraphs. *Physical Review E*, 82(6):066118, 2010. 87
- [53] Matt J Keeling and Ken TD Eames. Networks and epidemic models. *Journal of the Royal Society Interface*, 2(4):295–307, 2005. 49

- [54] Matthew J Keeling. The effects of local spatial structure on epidemiological invasions. *Proceedings of the Royal Society of London B: Biological Sciences*, 266(1421):859–867, 1999. [9](#), [86](#), [87](#), [88](#), [93](#), [97](#), [98](#), [99](#), [107](#), [126](#)
- [55] William O Kermack and Anderson G McKendrick. A contribution to the mathematical theory of epidemics. *Proceedings of the Royal Society of London A: Mathematical, Physical and Engineering Sciences*, 115(772):700–721, 1927. [4](#)
- [56] Istvan Z Kiss, Luc Berthouze, Timothy J Taylor, and Péter L Simon. Modelling approaches for simple dynamic networks and applications to disease transmission models. *Proc. R. Soc. A*, 468(2141):1332–1355, 2012. [49](#), [87](#), [97](#)
- [57] István Z Kiss, Joel C Miller, and Péter L Simon. *Mathematics of Epidemics on Networks*. Springer, 2017. [86](#), [92](#), [93](#), [96](#)
- [58] Kakajan Komurov and Michael White. Revealing static and dynamic modular architecture of the eukaryotic protein interaction network. *Molecular systems biology*, 3(1):110, 2007. [81](#)
- [59] Ravi Kumar, Jasmine Novak, and Andrew Tomkins. Structure and evolution of online social networks. In *Link mining: models, algorithms, and applications*, pages 337–357. Springer, 2010. [1](#)
- [60] Jinxian Li, Weiqiang Li, and Zhen Jin. The epidemic model based on the approximation for third-order motifs on networks. *Mathematical biosciences*, 2018. [88](#), [109](#)
- [61] Weihua Li, Shaoting Tang, Wenyi Fang, Quantong Guo, Xiao Zhang, and Zhiming Zheng. How multiple social networks affect user awareness: The information diffusion process in multiplex networks. *Physical Review E*, 92(4):042810, 2015. [84](#)
- [62] Jennifer Lindquist, Junling Ma, P Van den Driessche, and Frederick H Willeboordse. Effective degree network disease models. *Journal of mathematical biology*, 62(2):143–164, 2011. [86](#)
- [63] Ashok Litwin-Kumar and Brent Doiron. Slow dynamics and high variability in balanced cortical networks with clustered connections. *Nature neuroscience*, 15(11):1498, 2012. [40](#), [41](#)

- [64] Ashok Litwin-Kumar, Robert Rosenbaum, and Brent Doiron. Inhibitory stabilization and visual coding in cortical circuits with multiple interneuron subtypes. *Journal of neurophysiology*, 115(3):1399–1409, 2016. 123
- [65] Heiko J Luhmann, A Fukuda, and W Kilb. Control of cortical neuronal migration by glutamate and GABA. *Frontiers in cellular neuroscience*, 9:4, 2015. 12
- [66] Heiko J Luhmann, Anne Sinning, Jenq-Wei Yang, Vicente Reyes-Puerta, Maik C Stüttgen, Sergei Kirischuk, and Werner Kilb. Spontaneous neuronal activity in developing neocortical networks: from single cells to large-scale interactions. *Frontiers in neural circuits*, 10:40, 2016. 45
- [67] LyonLabs, LLC, and Barrett Lyon. The opte project. <http://www.opte.org/>. Accessed: 20th September 2018. xi, 2
- [68] Yunyong Ma, Hang Hu, and Ariel Agmon. Short-term plasticity of unitary inhibitory-to-inhibitory synapses depends on the presynaptic interneuron subtype. *Journal of Neuroscience*, 32(3):983–988, 2012. 44
- [69] Daniel Malagarriga, Alessandro EP Villa, Jordi Garcia-Ojalvo, and Antonio J Pons. Mesoscopic segregation of excitation and inhibition in a brain network model. *PLoS computational biology*, 11(2):e1004007, 2015. 42
- [70] Lauren Ancel Meyers, MEJ Newman, and Babak Pourbohloul. Predicting epidemics on directed contact networks. *Journal of theoretical biology*, 240(3):400–418, 2006. 54
- [71] Joel C Miller. Percolation and epidemics in random clustered networks. *Physical Review E*, 80(2):020901, 2009. 49, 87
- [72] Joel C Miller. Spread of infectious disease through clustered populations. *Journal of the Royal Society Interface*, pages rsif–2008, 2009. 87, 109
- [73] Joel C Miller. A note on a paper by Erik Volz: SIR dynamics in random networks. *Journal of mathematical biology*, 62(3):349–358, 2011. 8, 50, 123
- [74] Joel C Miller. Epidemics on networks with large initial conditions or changing structure. *PloS one*, 9(7):e101421, 2014. 8, 50, 80, 123
- [75] Joel C Miller. Mathematical models of SIR disease spread with combined non-sexual and sexual transmission routes. *Infectious Disease Modelling*, 2017. 82

- [76] Joel C Miller and Istvan Z Kiss. Epidemic spread in networks: Existing methods and current challenges. *Mathematical modelling of natural phenomena*, 9(2):4–42, 2014. [85](#), [96](#)
- [77] Joel C Miller, Anja C Slim, and Erik M Volz. Edge-based compartmental modelling for infectious disease spread. *Journal of the Royal Society Interface*, 9(70):890–906, 2012. [8](#), [49](#), [50](#), [53](#), [68](#), [70](#), [81](#), [83](#), [85](#), [86](#), [123](#), [124](#)
- [78] Joel C Miller and Erik M Volz. Model hierarchies in edge-based compartmental modeling for infectious disease spread. *Journal of mathematical biology*, 67(4):869–899, 2013. [49](#), [87](#)
- [79] Jose M Montoya and Ricard V Solé. Small world patterns in food webs. *Journal of theoretical biology*, 214(3):405–412, 2002. [1](#)
- [80] Peter J Mucha, Thomas Richardson, Kevin Macon, Mason A Porter, and Jukka-Pekka Onnela. Community structure in time-dependent, multiscale, and multiplex networks. *science*, 328(5980):876–878, 2010. [48](#)
- [81] Maziar Nekovee, Yamir Moreno, Ginestra Bianconi, and Matteo Marsili. Theory of rumour spreading in complex social networks. *Physica A: Statistical Mechanics and its Applications*, 374(1):457–470, 2007. [2](#)
- [82] Mark Newman. *Networks*. Oxford university press, 2018. [1](#)
- [83] Mark EJ Newman. The structure of scientific collaboration networks. *Proceedings of the national academy of sciences*, 98(2):404–409, 2001. [1](#)
- [84] Mark EJ Newman. The structure and function of complex networks. *SIAM review*, 45(2):167–256, 2003. [48](#)
- [85] Mark EJ Newman. Random graphs with clustering. *Physical review letters*, 103(5):058701, 2009. [87](#)
- [86] J-P Onnela, Jari Saramäki, Jorkki Hyvönen, György Szabó, David Lazer, Kimmo Kaski, János Kertész, and A-L Barabási. Structure and tie strengths in mobile communication networks. *Proceedings of the national academy of sciences*, 104(18):7332–7336, 2007. [1](#)
- [87] Ronald W Oppenheim. Cell death during development of the nervous system. *Annual review of neuroscience*, 14(1):453–501, 1991. [11](#)

- [88] Romualdo Pastor-Satorras, Claudio Castellano, Piet Van Mieghem, and Alessandro Vespignani. Epidemic processes in complex networks. *Reviews of modern physics*, 87(3):925, 2015. [2](#), [86](#)
- [89] Romualdo Pastor-Satorras and Alessandro Vespignani. Epidemic dynamics and endemic states in complex networks. *Physical Review E*, 63(6):066117, 2001. [86](#)
- [90] Gian Luca Pellegrini, Lucilla de Arcangelis, Hans J Herrmann, and Carla Perrone-Capano. Activity-dependent neural network model on scale-free networks. *Physical Review E*, 76(1):016107, 2007. [11](#)
- [91] Jill E Perry-Smith and Christina E Shalley. The social side of creativity: A static and dynamic social network perspective. *Academy of management review*, 28(1):89–106, 2003. [81](#)
- [92] Carsten K Pfeffer, Mingshan Xue, Miao He, Z Josh Huang, and Massimo Scanziani. Inhibition of inhibition in visual cortex: the logic of connections between molecularly distinct interneurons. *Nature neuroscience*, 16(8):1068, 2013. [44](#)
- [93] Hyun-Jae Pi, Balázs Hangya, Duda Kvitsiani, Joshua I Sanders, Z Josh Huang, and Adam Kepecs. Cortical interneurons that specialize in disinhibitory control. *Nature*, 503(7477):521, 2013. [44](#)
- [94] DA Rand. Correlation equations and pair approximations for spatial ecologies. *Advanced ecological theory: principles and applications*, 100, 1999. [9](#), [86](#), [87](#)
- [95] P Rattana, L Berthouze, and IZ Kiss. Impact of constrained rewiring on network structure and node dynamics. *Physical Review E*, 90(5):052806, 2014. [49](#), [82](#), [83](#)
- [96] Prapanporn Rattana, Konstantin B Blyuss, Ken TD Eames, and Istvan Z Kiss. A class of pairwise models for epidemic dynamics on weighted networks. *Bulletin of mathematical biology*, 75(3):466–490, 2013. [87](#)
- [97] Martin Ritchie, Luc Berthouze, Thomas House, and Istvan Z Kiss. Higher-order structure and epidemic dynamics in clustered networks. *Journal of Theoretical Biology*, 348:21–32, 2014. [27](#), [42](#)
- [98] Martin Ritchie, Luc Berthouze, and Istvan Z Kiss. Beyond clustering: Mean-field dynamics on networks with arbitrary subgraph composition. *Journal of mathematical biology*, 72(1-2):255–281, 2016. [87](#)

- [99] Marcel Salathé and James H Jones. Dynamics and control of diseases in networks with community structure. *PLoS Comput Biol*, 6(4):e1000736, 2010. 48
- [100] Karl Schilling, Michael H Dickinson, John A Connor, and James I Morgan. Electrical activity in cerebellar cultures determines purkinje cell dendritic growth patterns. *Neuron*, 7(6):891–902, 1991. 11
- [101] Alfons Schnitzler and Joachim Gross. Normal and pathological oscillatory communication in the brain. *Nature reviews neuroscience*, 6(4):285, 2005. 6
- [102] Fanni Sélley, Ádám Besenyei, Istvan Z Kiss, and Péter L Simon. Dynamic control of modern, network-based epidemic models. *SIAM Journal on Applied Dynamical Systems*, 14(1):168–187, 2015. 49, 83
- [103] Kieran J Sharkey, Carmen Fernandez, Kenton L Morgan, Edmund Peeler, Mark Thrush, James F Turnbull, and Roger G Bowers. Pair-level approximations to the spatio-temporal dynamics of epidemics on asymmetric contact networks. *Journal of mathematical biology*, 53(1):61–85, 2006. 87
- [104] Neil Sherborne, Joel C Miller, Konstantin B Blyuss, and Istvan Z Kiss. Mean-field models for non-markovian epidemics on networks. *Journal of mathematical biology*, 76(3):755–778, 2018. 87
- [105] Maxim S Shkarayev, Ilker Tunc, and Leah B Shaw. Epidemics with temporary link deactivation in scale-free networks. *Journal of Physics A: Mathematical and Theoretical*, 47(45):455006, 2014. 49, 83
- [106] Péter L Simon and Istvan Z Kiss. Super compact pairwise model for SIS epidemic on heterogeneous networks. *Journal of Complex Networks*, 4(2):187–200, 2015. 111
- [107] Olaf Sporns. The non-random brain: efficiency, economy, and complex dynamics. *Frontiers in computational neuroscience*, 5:5, 2011. 5, 13
- [108] Mark Steyvers and Joshua B Tenenbaum. The large-scale structure of semantic networks: Statistical analyses and a model of semantic growth. *Cognitive science*, 29(1):41–78, 2005. 1
- [109] András Szabó-Solticzky, Luc Berthouze, Istvan Z Kiss, and Péter L Simon. Oscillating epidemics in a dynamic network model: stochastic and mean-field analysis. *Journal of mathematical biology*, 72(5):1153–1176, 2016. 87

- [110] Daisuke H Tanaka, Mitsutoshi Yanagida, Yan Zhu, Sakae Mikami, Takashi Nagasawa, Jun-ichi Miyazaki, Yuchio Yanagawa, Kunihiro Obata, and Fujio Murakami. Random walk behavior of migrating cortical interneurons in the marginal zone: time-lapse analysis in flat-mount cortex. *Journal of Neuroscience*, 29(5):1300–1311, 2009. [12](#)
- [111] Michael Taylor, Timothy J Taylor, and Istvan Z Kiss. Epidemic threshold and control in a dynamic network. *Physical Review E*, 85(1):016103, 2012. [49](#), [83](#)
- [112] Pieter Trapman. On analytical approaches to epidemics on networks. *Theoretical population biology*, 71(2):160–173, 2007. [87](#), [109](#)
- [113] Ilker Tunc, Maxim S Shkarayev, and Leah B Shaw. Epidemics in adaptive social networks with temporary link deactivation. *Journal of statistical physics*, 151(1-2):355–366, 2013. [49](#), [83](#)
- [114] Gina G Turrigiano and Sacha B Nelson. Homeostatic plasticity in the developing nervous system. *Nature Reviews Neuroscience*, 5(2):97, 2004. [12](#)
- [115] LD Valdez, Pablo A Macri, and Lidia A Braunstein. Temporal percolation of a susceptible adaptive network. *Physica A: Statistical Mechanics and its Applications*, 392(18):4172–4180, 2013. [82](#), [83](#)
- [116] Pauline Van den Driessche and James Watmough. Reproduction numbers and sub-threshold endemic equilibria for compartmental models of disease transmission. *Mathematical biosciences*, 180(1-2):29–48, 2002. [110](#)
- [117] Martijn P van den Heuvel and Olaf Sporns. Network hubs in the human brain. *Trends in cognitive sciences*, 17(12):683–696, 2013. [13](#)
- [118] A Van Ooyen and J Van Pelt. Complex periodic behaviour in a neural network model with activity-dependent neurite outgrowth. *Journal of theoretical biology*, 179(3):229–242, 1996. [12](#), [20](#), [39](#), [44](#)
- [119] A Van Ooyen, J Van Pelt, and MA Corner. Implications of activity dependent neurite outgrowth for neuronal morphology and network development. *Journal of theoretical biology*, 172(1):63–82, 1995. [8](#), [12](#), [14](#), [16](#), [17](#), [39](#), [40](#), [41](#), [121](#)
- [120] Catelijne Van Oss and Arjen Van Ooyen. Effects of inhibition on neural network development through activity-dependent neurite outgrowth. *J. Theor. Biol*, 185:263–280, 1997. [12](#), [39](#), [40](#)

- [121] Matthew C Vernon and Matt J Keeling. Representing the UK’s cattle herd as static and dynamic networks. *Proceedings of the Royal Society of London B: Biological Sciences*, 276(1656):469–476, 2009. [81](#)
- [122] Alessandro Vespignani. Modelling dynamical processes in complex socio-technical systems. *Nature physics*, 8(1):32, 2012. [1](#)
- [123] Katherine L Villa, Kalen P Berry, Jaichandar Subramanian, Jae Won Cha, Won Chan Oh, Hyung-Bae Kwon, Yoshiyuki Kubota, Peter TC So, and Elly Nedivi. Inhibitory synapses are repeatedly assembled and removed at persistent sites in vivo. *Neuron*, 89(4):756–769, 2016. [44](#), [45](#)
- [124] Erik Volz. SIR dynamics in random networks with heterogeneous connectivity. *Journal of mathematical biology*, 56(3):293–310, 2008. [8](#), [50](#), [123](#)
- [125] Erik M Volz, Joel C Miller, Alison Galvani, and Lauren Ancel Meyers. Effects of heterogeneous and clustered contact patterns on infectious disease dynamics. *PLoS computational biology*, 7(6):e1002042, 2011. [2](#), [3](#), [49](#), [68](#), [81](#), [87](#), [124](#)
- [126] Wikipedia. Internet map 1024 - transparent, inverted. https://commons.wikimedia.org/wiki/File:Internet_map_1024_-_transparent,_inverted.png. Accessed: 20th September 2018. [xi](#), [2](#)
- [127] Fred Wolf, Rainer Engelken, Maximilian Puelma-Touzel, Juan Daniel Flórez Weidinger, and Andreas Neef. Dynamical models of cortical circuits. *Current opinion in neurobiology*, 25:228–236, 2014. [44](#)
- [128] Nobuhiko Yamamoto and Guillermina López-Bendito. Shaping brain connections through spontaneous neural activity. *European Journal of Neuroscience*, 35(10):1595–1604, 2012. [12](#)
- [129] Changwang Zhang, Shi Zhou, Joel C Miller, Ingemar J Cox, and Benjamin M Chain. Optimizing hybrid spreading in metapopulations. *Scientific reports*, 5, 2015. [82](#)
- [130] Dawei Zhao, Lixiang Li, Haipeng Peng, Qun Luo, and Yixian Yang. Multiple routes transmitted epidemics on multiplex networks. *Physics Letters A*, 378(10):770–776, 2014. [48](#), [82](#)
- [131] Yong Zhuang, Alex Arenas, and Osman Yağan. Clustering determines the dynamics of complex contagions in multiplex networks. *Physical Review E*, 95(1):012312, 2017. [48](#), [49](#)

- [132] Yong Zhuang and Osman Yağın. Information propagation in clustered multilayer networks. *IEEE Transactions on Network Science and Engineering*, 3(4):211–224, 2016. [49](#)